NOVEL TOOLS FOR SIMULTANEOUS OPTOGENETIC MANIPULATION AND CALCIUM IMAGING IN THE ZEBRAFISH NERVOUS SYSTEM

Zur Erlangung des akademischen Grades eines

DOKTORS DER NATURWISSENSCHAFTEN

(Dr. rer. nat.)

der KIT-Fakultät für Chemie und Biowissenschaften

des Karlsruher Instituts für Technologie (KIT)

genehmigte

DISSERTATION
von
Ali Gheisari
aus
Esfahan (Iran)

KIT-Dekan: Prof. Dr. Willem Klopper

Referent: Prof. Dr. Martin Bastmeyer

Korreferent: Prof. Dr. Francesco Saverio Pavone

Tag der mündlichen Prüfung: 27.04.2017

UNIVERSITÀ
DEGLI STUDI
FIRENZE

DOTTORATO DI RICERCA IN
ATOMICS AND MOLECULAR PHOTONICS

Dottorato Internazionale
CICLO XXIX

COORDINATORE Prof. Roberto Righini

NOVEL TOOLS FOR SIMULTANEOUS OPTOGENETIC MANIPULATION AND CALCIUM IMAGING IN THE ZEBRAFISH NERVOUS SYSTEM

Settore Scientifico Disciplinare FIS/03

Dottorando
Ali Gheisari

Tutore
Prof. Francesco Saverio Pavone

Tutore
Prof. Martin Bastmeyer

Coordinatore
Prof. Roberto Righini

December 2013- November 2016

Erklärung

Ich versichere hiermit, dass ich diese Arbeit selbstständig verfasst habe und keine anderen, als die angegebenen Quellen und Hinweise benutzt habe. Wörtlich oder inhaltlich übernommene Stellen sind als solche gekennzeichnet und die Satzung des Karlsruher Instituts für Technologie (KIT) zur Sicherung guter wissenschaftlicher Praxis habe ich in der gültigen Fassung beachtet. Ich versichere außerdem, dass die beigelegte, elektronische Version der Arbeit mit der schriftlichen übereinstimmt und dass die Abgabe und Archivierung der Primärdaten gemäß Abs. A (6) der Regeln zur Sicherung guter wissenschaftlicher Praxis des KIT beim Institut gesichert ist.

Ali Gheisari Karlsruhe, den 14.03.2016

To my parents

پیشکش به پدر و مادرم

Abstract

The large number of neurons and neural interconnection makes the nervous system a dense and complex network. Understanding the functionality of such a network requires not only high-throughput recording of neural activities with cellular resolution but also a non-invasive and well-defined interaction with the neurons. This work demonstrates two pivotal steps towards these aims:

(i) Developing a fluorescence microscope based on Bessel light-sheet illumination to record neural activities by means of calcium imaging. Part II describes the successful development and construction of an *in vivo* light-sheet fluorescence microscope (*in vivo* LSFM) based on conventional digitally laser scanning light-sheet microscopy (DSLM) with interchangeable Gaussian and Bessel illumination modalities to compare the performance of both methods. The Bessel illumination modality in comparison to the Gaussian one reveals not only a two-fold improvement in axial resolution but also a reduction by the factor of 4 in the shadowing artifact and consequently, 35 times improvement in detecting the correct neural activities from the calcium signals.

(ii) Providing a suitable transgenic zebrafish model for optogenetic manipulation; Optogenetics apply light to facilitate the interaction with a genetically-engineered cell and/or populations of cells. Part III describes the establishment of a transgenic zebrafish expressing a red-shifted channelrhodopsin, Chlamydomonas channelrhodopsin1 fused to Volvox channelrhodopsin1 (C1V1), under the elavl3 promoter making almost the entire nervous system of larval zebrafish accessible for optical manipulation. To the best of our knowledge, this is the first demonstration of a transgenic zebrafish with C1V1 pan-neuronal expression. The establishment of the stable transgenic line is in progress.

In future, crossing this line with an already established line expressing a calcium indicator protein will provide the essential animal model for simultaneous optogenetic manipulation and high-fidelity neural activity.

Contents

List of Figures

Part I

Background

Chapter 1

Fluorescence

Although the term "fluorescence" has been introduced by G.G. Stokes (1819-1903) [1] after a mineral called fluor-spar, this phenomenon had been reported since 16th century. He explained that so many materials and/or mixture of several chemical ingredients induce a spectral shift in the incident light. Nowadays, this shift is called Stokes shift. As is shown in Figure 1.1, the fluorescent materials emit a continuous spectrum shifted to larger wavelengths with respect to their absorbance spectrum [2].

Fluorescence is an emission phenomenon by a molecule that is in an excited state. The incident light (photon) excites the electron from its ground orbital to an outer (excited) orbital. Since the excited states are not stable, the electron releases a part of its energy as heat and falls into a lower excited orbital. Finally, the electron tends to rest again on the ground state by emitting the rest of the energy as a photon with lower energy, therefore, larger wavelength that are illustrated in Jablonski diagram (Figure 1.2). The first is the absorption (A) of the electromagnetic wave which has the wavelength correlated to the energy differences of the molecular states. The

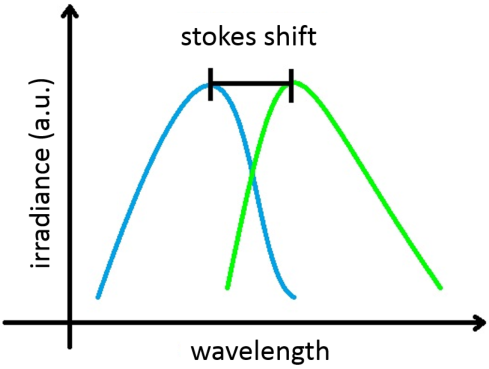

Figure 1.1: Stokes shift; The blue curve shows the absorbance spectrum and the green shows the fluorescence spectrum.

molecular energy levels are represented in Figure 1.2 using S for singlet state and T for triplet state according to their spin state. In the singlet states two electrons with opposite spins occupy the molecular orbital. According to Pauli Exclusion Principle, electrons in S states are paired with multiplicity of 1 [3]. It is notable that the excited electron preserves its spin while absorbing the energy.

Moreover, the energy level of a molecular orbital is quantized; hence, the excitation energies (equivalently wavelengths) of a molecule is unique [5]. The other straight arrows in Figure 1.2 show the emission ways of an excited molecule to its ground state. When a molecule emits a photon from a higher energy level to a lower one with the same spin state (e.g. $S1 \rightarrow S0$), this process is named fluorescence (F) and if their spin states are different (e.g. $T1 \rightarrow S0$), it is termed phosphorescence. Moreover, there are non-radiating relaxations which are shown in Figure 1.2 by arrows with zig zags. Internal conversion (IC) is the non-radiating relaxation between two energy levels

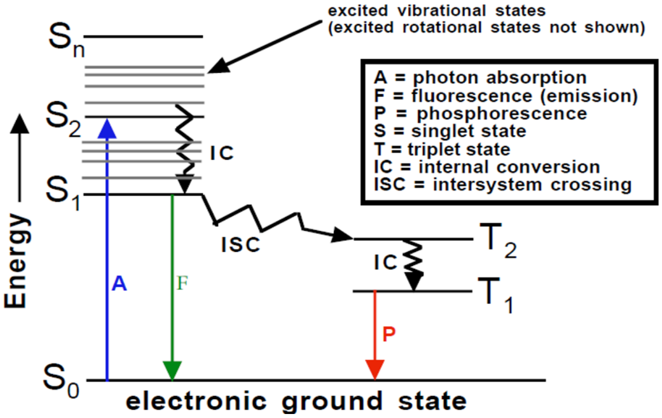

Figure 1.2: Jablonski diagram; A schematic representation of the molecular excitation and laxation. Straight arrows represent the irradiativ processes: the blue indicates the absorbance, the green, the fluorescence emission and the red one, the phosphorescence emission. While the arrows with zig zags shows the non-irradiative transitions as described in the box at the top right. Adopted from [4]

with the same spin state, while intersystem crossing (ISC) occurs between energy levels with different spin state. An oxygen-rich environment, a fluorescent structure with heavy metals [6] or paramagnetic moieties [7] can influence the intersystem crossing (k_{ISC}). When a fluorescent molecule goes to the triplet state, this can lead to photobleaching. The triplet states have unpaired electrons which give radical properties to the molecule. Moreover, the triplet states have a long lifetime that provides enough time for the fluorescent molecule to interact with the impurities, oxygen and/or other fluorescent molecules in the environment to yield non-fluorescent molecular structures [8]. There are several parameters that affect fluorescence, such as fluorescence quantum yield (Φ). Fluorescence quantum yield simply is the ratio of the number of those molecules emitting fluorescent photons to the number of photons absorbed by the system [9]. In other words, it is the relative rate of the fluorescence to all other relaxing phenomena such as internal conversion, intersystem crossing, phosphorescence, etc. including fluorescence:

$$\phi = \frac{k_f}{k_f + k_{nf}}, \tag{1.1}$$

where the fluorescence rate is shown by k_F and non-fluorescence rate overall, by k_{nF}. As explained by Lakowicz [10], in practice to obtain the fluorescence quantum yield, it is common to measure the fluorescence life time of a molecule from experiments. Whilst the fluorescence life time is defined as:

$$\tau = \frac{I}{k_f + k_{nf}}, \tag{1.2}$$

and F_k can be calculated by:

$$k_f = 2.88 \times 10^9 n^2 \frac{\int F\bar{v}d\bar{v}}{\int \bar{v}^3 F\bar{v}d\bar{v}} \tag{1.3}$$

where $F(\bar{v})$ represents the emission spectrum as a function of wavenumber (cm^{-1}), $\varepsilon(\bar{v})$, the absorption spectrum as the function of wavenumber while n is the refractive index of the medium. The integration is over the ground state (S_0) and first excited single state (S_1). Therefore, we can obtain the fluorescence quantum yield by dividing the life time to intrinsic lift time ratio:

$$\phi = \frac{\tau}{\tau_n} \tag{1.4}$$

where τ_n is intrinsic fluorescent life time of the fluorescent molecule. The intrinsic fluorescence life time is described as the life time of the fluorescence molecule in absence of the non-fluorescent relaxations, given by:

$$\tau_n = \frac{I}{k_n} \tag{1.5}$$

1.1 Fluorescent probes

Although, the luminance of jellyfish has been considered centuries ago, only in 1962, this phenomenon has been associated to the green fluorescent protein (GFP) by Shimomura. [11]

In 1974, Morise, Shimomura and their colleagues were able to isolate and crystallize GFP [12]. The revolutionary step in fluorescence study has been the sequencing of the GFP gene by Pracher [13]. It took two years for Chalfie to put GFP sequence into a DNA vector which causes the cells to fluoresce in green, under UV or blue light [14]. Later on, yellow, blue, cyan and red fluorescent proteins families have been developed providing a variety of tools to mark or indicate specific actions and/or structural components in cells and organs. [15]

Each fluorescent protein contains a chemical component which has fluorescent properties. This component is called fluorophore, which is, in general, a large polycyclic aromatic hydrocarbons (PAH). The structure of four common FP derived from GFP is shown in Figure 1.3. GFP is a barrel-shape

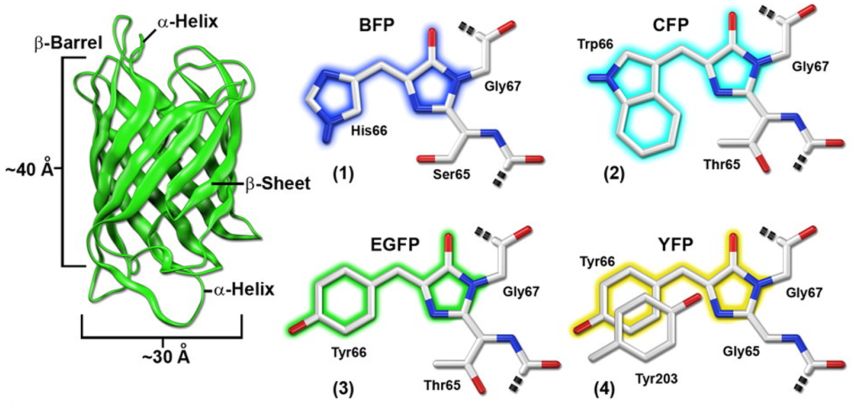

Figure 1.3: Fluorescent protein (FP) architecture with dimensions and four common chromophores derived from Aequorin; 1) Blue FP 2) Cyan FP 3) Green FP 4) Yellow FP. Adopted from [16]

protein with a planar ring structure containing conjugated double bonds at the center. The differences in the number of aromatic rings, the ligands properties and their positions as well as the structural characteristics of the fluorophores are shown in Figure 1.3.

Polycyclic aromatic hydrocarbons or PAHs are compounds containing fused aromatic ring. One way to shift the emission of the molecule toward red is to increase the number of hydrocarbon conjugation [17]. More fused aromatic rings decrease the overall molecular energy; therefore, they shift the emission spectrum towards the visible range. Another important parameter to consider is the structure of the molecule. As shown in Figure 1.4, anthracene and phenanthrene both have three aromatic rings but different structures. Anthracene is a linear molecule which emits highest fluorescent intensity at about 400 nm while phenanthrene emits at about 365 nm. Tetracene and benza(a)anthracene follow the same trend. They exhibit

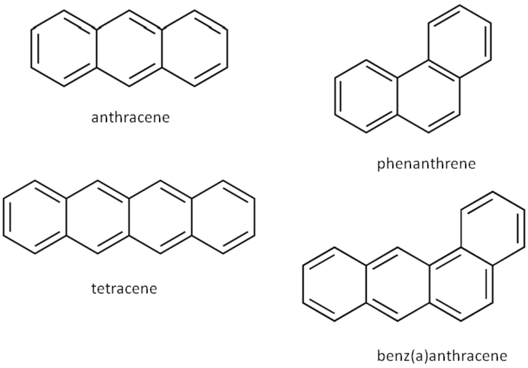

Figure 1.4: Compounds containing fused aromatic rings or polycyclic aromatic hydrocarbons (PAH); Their properties vary depending on the number of the fused aromatic rings and their arrangement. Four small PAHs are shown as examples. Adopted from [17]

their most intense fluorescence at about 510 nm and 386 nm respectively [18]. Genetically engineered [19] fluorescent proteins with better extinction coefficients and higher quantum yields have been a critical and trending field in fluorescence studies, such as fluorescence microscopy. [20]

Chapter 2

Fluorescence microscopy

Since the first microscope was introduced in the 17^{th} century, distinguishing between the regions of interest in the object and the background has been highly important. Fluorescence occurs only in the objects matching the features explained in chapter 1 This selectivity provides bright images of the object of interest while the background is dark. Fluorescence microscopy has undergone several improvements in resolving the details, speed of acquisition to high throughput, long-term imaging both *ex vivo* and in *vivo* and in the automatic manner via software developments. [21]

The most common fluorescence microscope is called wide-field fluorescence microscope (Figure 2.1). It, briefly, is a light source uniformly illuminating the sample through an objective (acting as the condenser) and collecting the fluorescent photon with the same objective (acting as the collector) toward the detector. The key point of a fluorescence microscope is filtering all wavelengths out the collected light but the fluorescent ones. [22]

The light source is typically of high pressure lamps such as mercury arc lamp, lasers or LEDs providing a wide range of excitation wavelengths. The

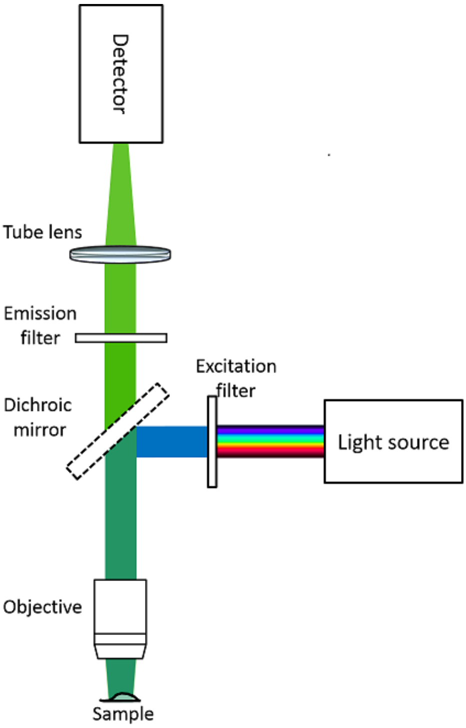

Figure 2.1: Wide-field fluorescence microscope; The light from the source is filtered to the excitation wavelength. The excitation light is deflected by a dichroic mirror and then uniformly illuminating the sample through an objective. The collected fluorescent photons with the same objective pass through the dichroic mirror and the emission filter. Latter, they are imaged on the detector by a tube lens.

beam is then deflected by a dichroic mirror toward the objective. Dichroic mirrors deflect a part of the electromagnetic spectrum while are transmittable to another part based on their characteristics. The sample is excited through the objective. The emitted fluorescent photons are then collected by the objective and filtered by the emission filter. Finally, the fluorescent image is formed on a detector such as a camera or a photomultiplier (PMT) by a tube lens.

2.1 Image formation

Diffraction and interference are the principal phenomena defining how a microscope is forming the image. Moreover, these physical phenomena are in accordance to the wave nature of the light formulated in the field of wave optics. Considering wave optics, the image of a point-like object is a diffraction pattern created via interference of the collected rays through an optical system. The image of the point-like object takes the shape of a smeared point which defines the impulse response of the system. Since the fluorescence microscope provides the image of the specimen through the combination of the optical element, its impulse response defines the correlation between the object and its image as explained by Goodman [23]

$$U(\vec{r}) = \int\int\int h(\vec{r},\vec{r'})O(\vec{r'})d\vec{r'} \tag{2.1}$$

where h denotes the impulse response of the system, O and U stand for the spatial distribution of the object at $\overrightarrow{r'}$ in its space and the field distribution of the propagated electromagnetic wave positioned at $\overrightarrow{r'}$ in image space respectively. In case of fluorescence microscopy, it is convenient to utilize

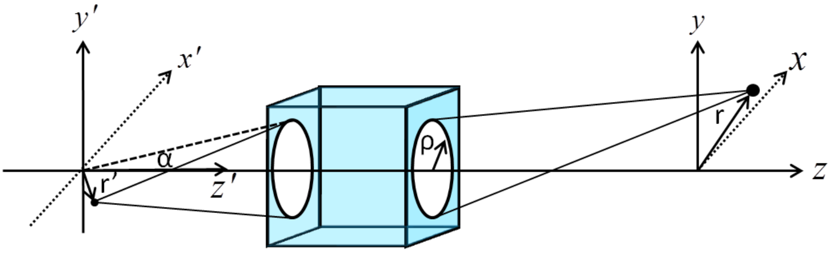

Figure 2.2: Diagram of image formation through an optical system with notation; The emitted field from the object at $\vec{r'}$ propagates through an unknown optical system such as a fluorescence microscope shown with blue box. The microscope images the propagated field at $\vec{r}$ in image space. α is the half-aperture angle of the entrance pupil.

the term intensity distribution, I, instead of the field one. Because, in eq. 2.1, the field distribution in object space is assumed to be coherent whereas the fluorescent molecules emit randomly, hence, the propagated fields originated from individual molecules are not correlated. Therefore, eq. 2.1 can be revised for the intensity:

$$I(\vec{r}) = \int\int\int |h(\vec{r}, \vec{r'})|^2 O(\vec{r'}) d\vec{r'} \tag{2.2}$$

where the impulse response of the system for intensity is the modulus square of the impulse response of the system for the field.

We assume that the object is point-like; therefore, O is mathematically represented by a delta function. Following eq. 2.2, the impulse response of the system for a point-like object is called point spread function or PSF. Furthermore, we assume that the microscope is a linear optical system fulfilling the Abbe sine condition. Besides, we can reduce the imaging

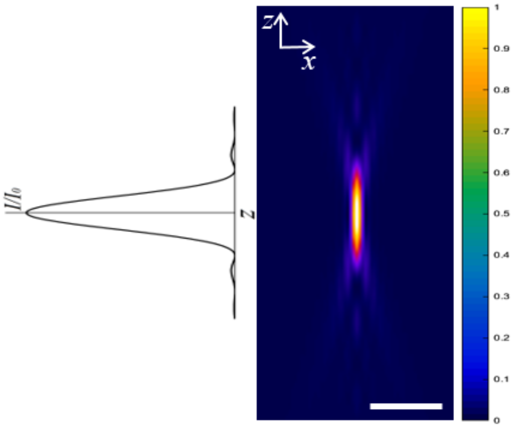

Figure 2.3: xz section of the diffraction limited PSF for an optical system with circular aperture; $NA = 1$ and $\lambda = 510\ nm$ matching the characteristics of our custom fluorescence microscope. The intensity is normalized to 1 according to the colormap on the right. Scale bar is $5\mu m$

problem to a system with circular aperture since the cross section of the optical elements in common microscopes is circular. In this case, the PSF of the microscope can be given by [24]

$$PSF(r,z) = c|\int_0^1 J_0(NAK_0\rho r)e^{\frac{ik_0}{2n}(NA)^2\rho^2 z}\rho d\rho|^2 \tag{2.3}$$

where c denotes a constant, J_0 the 0^th order Bessel function of the first kind, $\vec{\rho}$ the radial unit vector of the microscope exit aperture, $r = \sqrt{x^2 + y^2}$ and z represent the radial and axial position of the image element respectively and k_0 the wavenumber. Here, $NA = n\ sin\alpha$ stands for numerical aperture which defines the light collecting strength of the optical system where n is the refractive index of the medium and α the half-aperture angle of the entrance pupil (Figure 2.2). The xz section of the PSF of the above-mentioned system is shown in Figure 2.3.

Each geometrical object can be represented as a continuous modulation of points that each point produces a paraboloidal wave. From point (x', y'), a wave originates with the complex amplitude of $f(x', y')$ centered about (x', y') and propagates in free space. So that the point (x', y') generate a wave with the amplitude of $f(x', y')\ h(x - x', y - y')$ at the corresponding point (x, y). The sum of the contribution of each point of the object is

$$g(x, y) = \iint_{-\infty}^{\infty} f(x', y')h(xx, yy)dx'dy' \tag{2.4}$$

which is a two-dimensional convolution, $g(x, y)$ being the complex amplitude of the wave at the output. Analogously, the image formed by an imaging system is a superposition of the PSFs of each points in the object. So that the image can be calculated by the convolution of the object with the system PSF. The aforementioned method in Fresnel approximation is founded in space domain. Alternative to the space-domain approach is the frequency-domain approach in which the output wave is considered as the superposition of the plane waves with different spatial frequencies.

As an arbitrary function, $f(x, y)$ can be written as a superposition of harmonic functions through Fourier transform,

$$f(x, y) = \iint_{-\infty}^{\infty} F(v_x, v_y)e^{(-2\pi i(v_x x + v_y y))}dv_x dv_y \tag{2.5}$$

where $F(v_x, v_y)$ is the complex amplitude of a plane wave with the frequencies (v_x, v_y). The output wave, $g(x, y)$ of the system is a sum of plane wave

$$\begin{tikzcd}
f(x,y) \arrow[r, "PSF"] \arrow[d, "FT"'] & g(x,y) \\
F(v_x,v_y) \arrow[r, "OTF"'] & G(v_x,v_y) \arrow[u, "FT^{-1}"']
\end{tikzcd}$$

Figure 2.4: Correlation diagram of image formation approaches; $f(x,y)$ denotes the input, $g(x,y)$, the output and their Fourier transform function are $F(vx,vy)$ and $G(vx,vy)$, respectively. FT is the abbreviation Fourier transform and FT^{-1} stands for the reverse Fourier transform.

with the complex envelope of $G(v_x,v_y) = H(v_x,v_y)F(v_x,v_y)$ is the Fourier transform of $g(x,y)$ in eq. 2.4,

$$g(x,y) = \iint_{-\infty}^{\infty} H(v_x,v_y)F(v_x,v_y)e^{(-2\pi i(v_x x+v_y y))}dv_x dv_y \tag{2.6}$$

$H(v_x,v_y)$ being the response of the optical system to the spatial harmonic functions (plane waves complex amplitude), known as optical transfer function (OTF). This two approach are coupled via Fourier transform in the way that the imaging power of an optical system is either defined by the PSF or OTF of the system as illustrated in Figure 2.4.

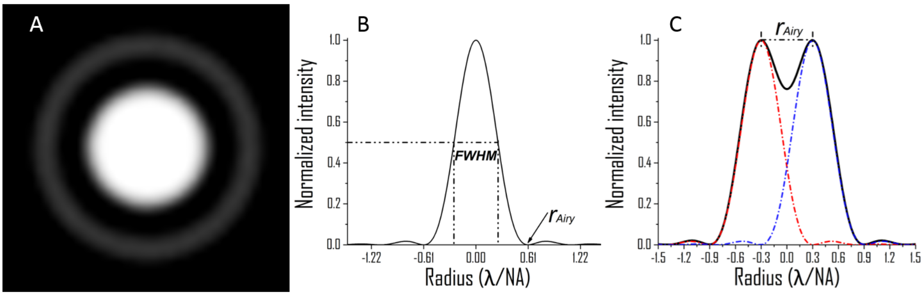

Figure 2.5: A) Airy diffraction pattern; the PSF of a point-like object through a microscope objective. B) Cross section of the Airy diffraction pattern (intensity distribution); r_{Airy} and FWHM are indicated. C) The overlap of the PSF of two point-like objects at r_{Airy} distant from each other on the image plane. In accordance to the Rayleigh criterion, the objects are just resolved.

2.2 Spatial resolution

Spatial resolution is a fundamental property of each optical system. It is defined as the shortest distances that two point-like objects can be just distinguished as distinct entities by the detector. [25]

For a point-like object the PSF in the focal plane of the microscope objective ($z = 0$) is derived from eq. 2.3;

$$PSF(r, 0) = c \mid \int_0^1 J_0(NAk_0\rho r)\rho d\rho \mid^2 \tag{2.7}$$

since,

$$\int_0^b xJ_0(ax) = \frac{b}{a}J_1(ab) \tag{2.8}$$

where J_1 denotes first order Bessel function of the first kind [26]. Replacing x with ρ and ρ with $NAkr$ whilst taking $b = 1$ in eq. 2.8, we have

$$PSF_{z=0} \propto \left(\frac{J_1(NAk_0r)}{NAk_0r}\right)^2, r = \sqrt{X^2 + y^2}. \tag{2.9}$$

This diffraction pattern is known as Airy diffraction pattern (Figure 2.5A) where the propagation of light in the free space after the objective is determined by the Fresnel approximation [27]. The first zero of eq. 2.9 is placed at (Figure 2.5B):

$$r_{Airy} = 0.61\frac{\lambda}{NA} \tag{2.10}$$

In case of the fluorescence microscope, each fluorophore is imaged proportionally to PSF of the microscope. This leads to the fact that if two fluorophores are such close to each other that their intensity peaks are at a distance of r_{Airy}, in accordance to the Rayleigh criterion, they are just resolvable (Figure 2.5C). In other words, the resolution of the microscope on the image plane or its radial resolution is given by the Airy radius eq. 2.10. In the axial direction, at the focal point ($r = 0$), the PSF is

$$PSF(r = 0, z) \propto \left(\frac{sin\left(\frac{u}{4}\right)}{\frac{u}{4}}\right)^2, u = \frac{k_0NA^2z}{n} \tag{2.11}$$

Analogous to the radial resolution by applying the Rayleigh criterion, we obtain the axial resolution by:

$$z_{min} = \frac{2n\lambda}{NA^2} \tag{2.12}$$

However, it is common to measure the 3D PSF of the microscope formed near the focal plane utilizing sub-diffraction fluorescent beads and fitting the radial and axial intensity distribution along the PSF with a one-dimensional Gaussian function. Hence, it is practical to use the full-width of the profile at half of the maximum intensity (FWHM) as an alternative measure for resolution.

$$FWHM_{radial} \approx 0.84 r_{Airy} \qquad FWHM_{axial} \approx 0.89 z_{min} \tag{2.13}$$

It is notable that the integral of the radial PSF at different z is constant (Figure 2.6). In other words, the out-of-focus fluorophores emit unwanted light collected by the objective and contribute to the image formation at the detector. This leads to the reduction of image quality such as sharpness and contrast and consequently, the resolution of the microscope. Therefore, one should consider to image thin objects or limiting the illumination field and blocking out-of-focus light. These considerations have led to physically sectioning the sample to thin slices or novel microscopy techniques that either restrict the illumination to the focal plane or are able to distinguish between in-focus and out-of-focus light. Such systems are said to perform optical sectioning [28]. (see chapter 2.5).

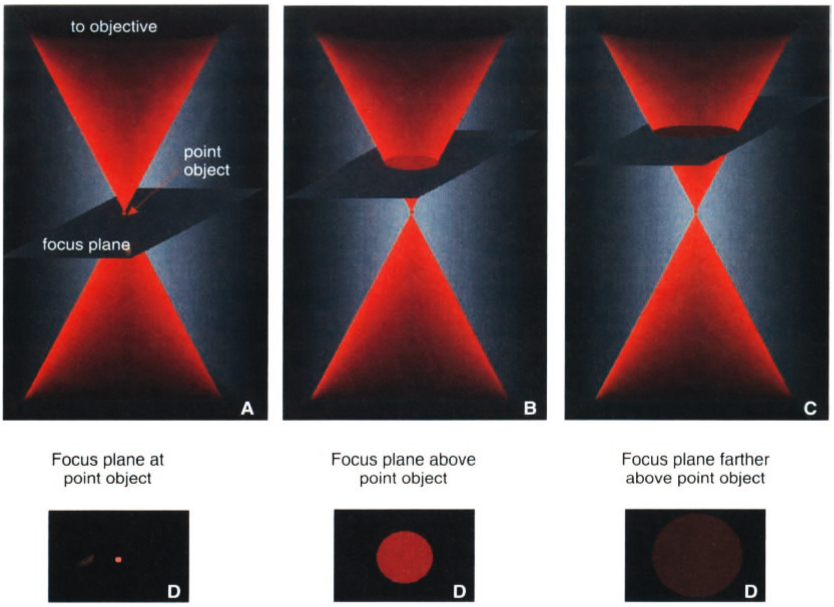

Figure 2.6: Appearance of a point-like object with respect to the focus plane; Further from the focus, the intensity is spread more while its integral is constant assuming no absorbance occurred via propagation. Adopted from [29]

2.3 Sampling

The term sampling refers to the representation of a continuous function (analog) with its discrete values at equidistant points. The interval between each two equidistant points is called the sampling distance. As shown in Figure 2.7, $I(x)$ is a continuous function in space coordinate (X) that has been sampled at equidistant positions. In other words, sampling is digitizing values at discrete coordinates.

The image is a two-dimensional continuous function of intensity over space

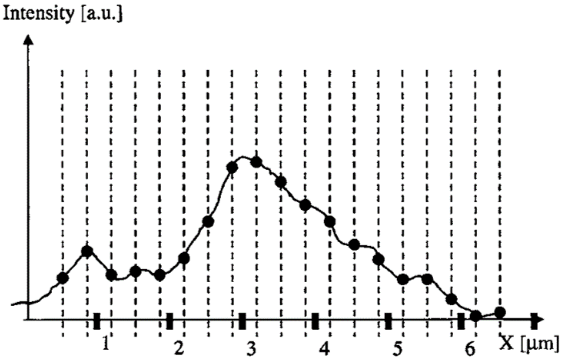

Figure 2.7: Sampling; The intensity of a signal (I) is plotted as a function of space coordinate (X). Dashed lines indicate the samples. Adopted from [30]

coordinates projected on a light detector. Nowadays, microscopes are equipped with a light detector which converts the collected photons to an electrical signal yielding to the digital image, namely the digital cameras. A digital camera is equipped with either a charged-couple device (CCD) or a complementary metal-oxide semiconductor (CMOS) photo sensor that are two-dimensional arrays of light detector.

The smallest element of a CCD (similar for CMOS) is called pixel acting as an individual photo sensor which are normally of square shape. The amplitude of the electrical signal produced by each pixel is assigned to a digital element independently from its neighbor pixels and is proportional to the number of collected photons. Therefore, the analogue image acquired from the object is sampled according to the pixels on the CCD. whilst the sampling distance (D) is given by the size of the pixels (pixel pitch) in object space:

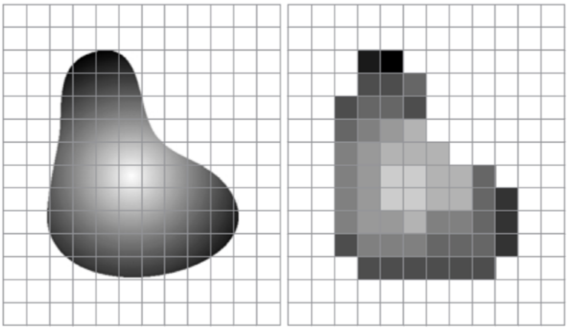

Figure 2.8: Sampling of an analog image (right) to a digital one (left) through a sensor array (CCD or CMOS). Adopted from [31]

$$D = \frac{P}{M} \tag{2.14}$$

where P and M are the actual pixel pitch of the camera and total magnification of the imaging system.

Figure 2.8 presents the digital image reconstructed from a continuous image projected on a CCD camera. In order to reconstruct the original signal reliably through digitization, the Nyquist theorem provides an optimal strategy in sampling. The Nyquist theorem has been proved by Shannon, rephrasing that the sampling frequency should be more than double the highest frequency in the signal [29]. In a microscope, the cut-off frequency is a measure for the highest frequency contributing in producing an image, therefore the sampling frequency (ν_s) should be larger than $2\nu_c$ or the Nyquist frequency (ν_{Nq}).

$$\nu_{Nq} = 2\nu_c \tag{2.15}$$

where, in case of wide-field fluorescence microscope [30]

$$\nu_{Nq} = \frac{4NA}{\lambda} \tag{2.16}$$

where λ presents the shortest emission wavelength and NA the numerical aperture of the microscope. Furthermore, it is common to use CCD cameras as the detector in wide-field microscopes. Thus the sampling frequency can be obtained from eq. 2.14:

$$\nu_s = \frac{1}{D} \tag{2.17}$$

therefore,

$$D \prec \frac{\lambda}{4NA_{obj}} = 0.41(r_{Airy}) \tag{2.18}$$

which means that for imaging a distance of the radius of Airy disk in the object, at least two pixels on the camera are required.

2.4 Signal-to-noise ratio

Since the development of the microscope, distinguishing the object of interest from the background has been an issue. Although fluorescence microscopy provides a sensitive imaging system, there are other sources to degrade fluorescence images. A common measure to define the sensitivity of a microscope is signal-to-noise (SNR). In signal processing, SNR is described as the relative level of the desired signal to the undesired one (noise). Mathematically this is calculated by dividing the power of the signal (P_{signal}) to the power of the background noise (P_{noise}).

$$SNR = \frac{P_{signal}}{P_{noise}} \tag{2.19}$$

In some situations, such as digital images from a light detector (e.g. CCD camera), the mean of the gray values of an image (practically of a region of interest or ROI) describes the signal while the standard deviation of the background shows the noise (all undesired signals). Therefore, the SNR of an image is given by: [32]

$$SNR = \frac{\mu}{\sigma} \tag{2.20}$$

where μ represents the mean value over a region of interest and σ the standard deviation of the background. The higher the SNR, the better the images and the more sensitive is the microscope.

Considering the Rose criterion, the features of an image are completely distinguishable if its SNR is at least 5 [33]. It is notable that there are sources of noise in the imaging systems which limit the imaging performance. Noise occurs, mainly, through the digitization of the collected photon to amplified electric signal by the light detectors. An incessant source of noise in digital imaging is the so called shot noise. The dominant shot noise arises due to a quantum limitation caused by the variable number of the photons detected by the detector at a defined time interval (e.g. exposure time of a camera). Since the propagation of the photons is temporally independent, according to the Poisson distribution, the noise of an image is equal to the square root of the number of the detected photons. This noise is known as photon shot noise or quantum noise. Thus, it is critical in case of imaging when the signal is low.

$$noise_{quantum} = \sqrt{\#photon} \tag{2.21}$$

Due to array detectors, it is notable that the photon shot noise of each pixel is independent from the other one.

There is an additional shot noise which is known as dark shot noise. It is caused by the leakage of current in the circuits of the image sensor. This noise can be avoided by subtracting a dark image by the detector from the desired image. [34]

In addition to shot noise, the undesired ballistic photons from the object cause reduction in the image quality. For instance, when out-of-focus fluorescent photons reach the detector, they induce blurriness in the formed images. Contrast is a measure of the brightness of the image of an object with respect to the other object in the same region of interest (ROI) that can be quantified by:

$$contrast = \frac{n_b - n_d}{2n_{avg}} \tag{2.22}$$

where $2n_{avg}$ represents the intensity average over the ROI and n_b and n_d, the intensity of the bright and the dark section of the ROI. Contrast can be enhanced via illuminating the object with higher power (which increases the probability of photo damages in general and photobleaching in fluorescence microscopy) and blocking the undesired light, such as utilizing filters in fluorescent microscopes or spatially blocking out-of-focus light by placing a spatial filter (pinhole) at the conjugated plane to the sample and the detector in a confocal microscope.

2.5 Optical sectioning

Although the wide-field fluorescence (Figure 2.9A) equipped with a fast digital camera provides fast acquisition in large field of view, it does not provide optical sectioning. Thus, the ballistic photons emitted from out-of-focus fluorophores contribute in the formation of the image on the detector (camera, photomultiplier, etc.) as blurriness, therefore, they lower the contrast. To overcome this contribution, either the excitation should be restricted to the plane in object space conjugated to the detector or the system should be capable of rejecting the out-of-focus light. This is called optical sectioning.

Here confocal microscopy, two-photon microscopy and light-sheet fluorescent microscopy (LSFM) will be discussed. In confocal microscopy (Figure 2.9B) the illumination light comes from a pinhole (illumination pinhole) in a conjugated plane to the focal plane of the objective. Later, the emitted fluorescence collected by the objective passes through a second pinhole (detection pinhole). The detection pinhole is placed in front of a fast detector (most commonly, a PMT) and in another plane conjugated to the focal plane of the objective. The pinholes, with respect to each other, are said to be confocal. The optical sectioning is obtained through:

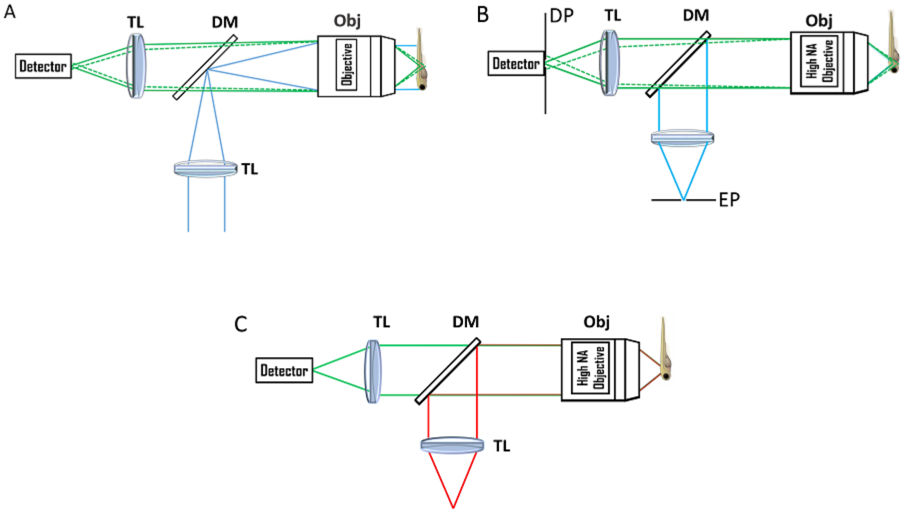

Figure 2.9: Simplified scheme; A) wide-field fluorescent microscope. B) confocal fluorescence microscope. C) two-photon fluorescence microscope. The blue rigid lines depict the illumination light for single-photon excitation (typically in range of visible wavelengths) and the red rigid lines, the infrared excitation where the green rigid lines are in-focus fluorescence and the dashed lines are out-of-focus fluorescence propagating toward the detector. Obj is the abbreviation for the Objective; DM for dichroic mirror; TL for the tube lens; EP for the excitation pinhole; DP for the detection pinhole.

- Focusing the illumination, thus fewer out-of-focus fluorophores with lower power are excited.
- The detection pinhole spatially filters the out-of-focus light out.

Although the confocal microscope provides high contrast images with high resolution, its drawbacks limit its application in brain activity imaging. Confocal microscopy requires high intensity excitation which can lead to photobleaching and in cases, phototoxicity. Furthermore, to collect more photons emitted from the fluorophore on the focal plane, it needs high NA objectives. Utilizing the high NA objectives limits the working distance and therefore the depth achievable. Another popular technique performing optical sectioning is known as two-photon fluorescence microscopy [35]. The fluorescence occurs by the absorbance of two photons with roughly half energy required for one-photon fluorescence (Figure 2.10A). To achieve efficient two-photon excitation, the light intensity should be localized spatially and temporally. The light intensity of a laser beam working in TEM_{00} mode (I), in case of Gaussian-Lorentzian distribution approximation [36] is given by:

$$I(\rho, z, t) = \frac{2P(t)}{\pi\omega^2(z)} e^{-\frac{2\rho^2}{\omega^2(z)}}, \omega(z) = \omega_0 \sqrt{1 + \left(\frac{z}{z_r}\right)^2} \tag{2.23}$$

where ρ and z are the radial and axial coordinates when their origin is at the focus spot. $P(t)$ is the laser power as a function of time and ω_0 and z_R are the beam waist at focal plane and Rayleigh length, respectively. Furthermore, the two-photon absorption from state i to the state f, $(\bar{\omega}^{(2)}_{i \to f})$ is proportional to the square of the light intensity in eq. 2.23. The fluorescence emission (F), also, is proportional to the two photon absorption.

These lead to the drop of the fluorescence emission with the power of four of the axial distant (z) away from focal spot [37]:

$$F \propto z^{-4} \tag{2.24}$$

which means fluorescence occurs nonlinearly in a small volume around the focus. In this way, the fluorophores out of the focus volume are not excited and optical sectioning is obtained. The confinement of two-photon absorption to a diffraction-limited focus (Figure 2.10B) reduces the problem of phototoxicity and photobleaching and it allows us to acquire images of living samples with a resolution comparable to the one of confocal microscopy whereas no spatial filter (pinhole) is required (Figure 2.9C). Moreover, two-photon excitation wavelengths are in the infrared range; taking into account the transparency of biological samples in this wavelength region, this leads to in-depth imaging in highly-scattering biological samples, such as in brain. The common drawback of confocal microscopy and two-photon microscopy is not only the requirement of high NA objectives but also the way 2D images are acquired. The 2D images are, commonly, obtained via scanning focused light over the focal plane with galvanometer mirrors. This leads to a reduction in the temporal resolution of the system and therefore, two-photon microscopes cannot be capable to track the dynamics of the neuronal system, namely, the calcium ion (Ca^{2+}) propagation over a large sample such as zebrafish brain. To overcome this limitation in two-photon microscopy, several technological improvements have been introduced; namely, utilizing acousto-optic devices to sweep the focused laser beam over large number of positions (random access two-photon microscopy [38]) or resonant galvanometer mirrors which work only at one specific frequency [39]. Although faster scanning enables the scientists to utilize the laser scanning microscopes to record fast dynamics, recording at such high frame rates lower the pixel dwell time meaning less signal collected. To leverage the signal level, the illumination power must be increased which consequently increments the risk of photobleaching and phototoxicity. To overcome these drawbacks, light-sheet fluorescence microscopy (LSFM) which performs optical sectioning and acquires 2D images with such temporal resolution comparable to wide-field microscopy can be applied.

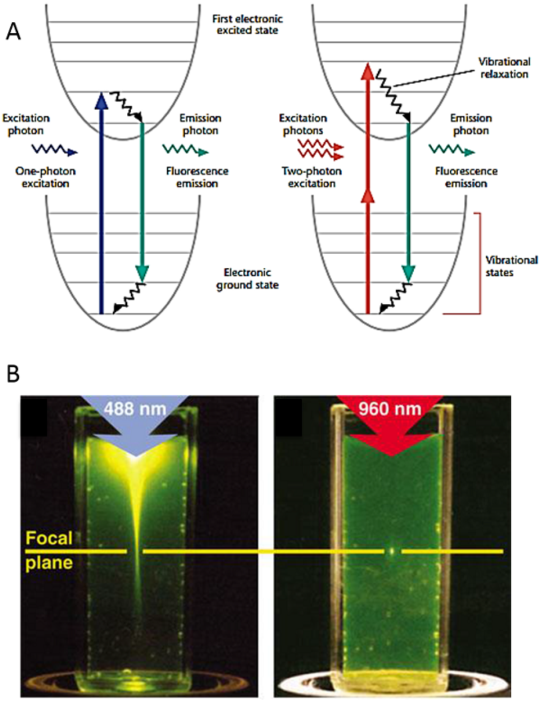

Figure 2.10: Two-photon excitation; A) The Jablonski diagrams for single-photon excitation (left) and two-photon excitation (right). Adopted from [40] B) The localization of the excitation in case of single-photon absorption (left) and two-photon absorption (right). Adopted from [41]

Chapter 3

Zebrafish for *in vivo* imaging

Zebrafish has become an interesting and important study model in biology decades ago, ranging from developmental biology [42] to activity and functional studies [43]. The partial transparency of the embryos and larvae allows direct observation of organ development through the chorion[1]. The availability of pertaining genetic toolset and its small size make it an important model which mimics the development and functionality of the higher vertebrates in a minimalist manner. Zebrafish is suitable for carrying out the mutagenesis to render stable mutations even by disruption of a single gene [44]. These advantages allow several experimental approaches to be undertaken, such as whole-brain Ca^{2+} imaging [45] or optical manipulation [46]. The zebrafish brain consists of 10^5 neurons [47]. As in other teleosts [2], the optic tecta in the midbrain dominate the brain [48]. The telencephalon lobes attached to the olfactory bulb lobes (Figure 3.1) are smaller than the optic tectum. Although the mesencephalon is covered by the optic tectum

---

[1] The outer embryonic membrane

[2] The largest infraclass of ray-finned fishes

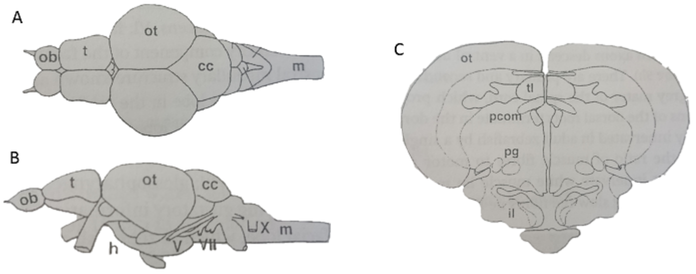

Figure 3.1: Drawing of the adult zebrafish brain; A, B denote the whole brain lateral, dorsal views, respectively and C, the paraffin-stained mesencephalon section. The subdivisions and preglomerular nucleus are represented with abbreviation: cc, corpus cerebelli; h, hypothalamus; il, inferior lobe; m, metencephalon; ob, olfactory bulb; ot, optic tectum; pcom, preoptic area; pg, preglomerular nucleus; t, telencephalon; tl, torus longitudinalis, V, trigeminal, VII, facial nerve; X, vagal nerve. Adopted from [49]

(Figure 3.1C) and is not apparent from the dorsal view (Figure 3.1A), the hypothalamus and pituitary are visible in the lateral view (Figure 3.1B). [49]

Recent studies investigated organ development and functionality such as the heart [50, 51], behavioral observations [52] or the mechanism of olfactory responses in zebrafish larvae [53]. The larval zebrafish is more interesting in the case of fluorescent imaging rather than the adults. Figure 3.2 shows a larval brain of the zebrafish 5 days post fertilization (dpf) addressing the gap, to be considered, between larval and adult zebrafish brain morphology and therefore, functionality. [49]

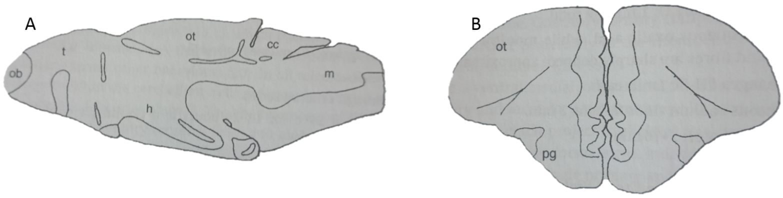

Figure 3.2: Drawing of the 5 dpf (day(s) post fertilization) zebrafish larvae;
A) The lateral view of whole brain
B) the paraffin-stained mesencephalon section. Adopted from [49]

Chapter 4

Mapping nervous system activity

The nervous system consists of interconnected circuits of neurons that selectively perform a variety of tasks. These include receiving information from the sensory system, propagating and interpolating the information, eliciting actions via motor-neurons exhibiting behavior as well as regulating the internal functionality of the organs. They perform before-mentioned functions via communication with one another through well-defined electrical and chemical signals. In accordance to the broad variety of the tasks, the nervous system requires a highly dynamic system consisting of several specialized compartments. In neuroscience, a central goal is to understand the nervous system functionality.

The large number of neurons and neuron-neuron interconnectivity makes the nervous system a highly-dense and complicated network. Understanding the functionality of such network requires not only a sophisticated processing of the information as it propagates through the whole meshwork

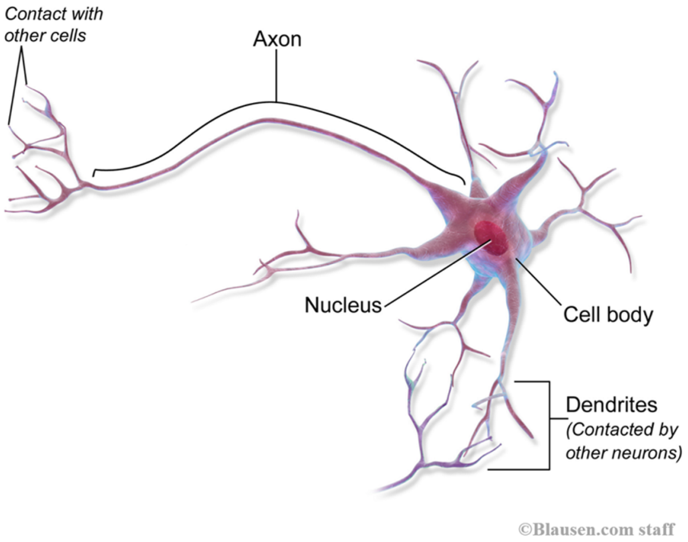

Figure 4.1: Scheme of a neuron showing the general structure; The information is received by dendrite from the other neuron and is transmitted to the cell body (soma). The cell body contains the nucleus where all received signals are integrated and analyzed. Then, the axon transfers the generated signal from the cell body to the other cells.

but also a prior knowledge of structure of the meshwork. Neurons (Figure 4.1) are electrically excitable cells which transfer the information as spikes of voltage named action potentials. There is an unequal distribution of ions on two sides of the nerve cell membrane known as membrane resting potential. The membrane separates the extracellular and intracellular media, acting as barrier that prevents diffusing of many proteins, molecules and ions from extracellular fluids to the intracellular and vice versa. On the other hand, the neuron membrane is selectively permeable to only few ions, to be named sodium (Na^+), potassium (K^+), chlorine (Cl^-) and calcium (Ca^{2+}). The membrane consists of protein channels and pumps that maintain the number of the intracellular ions with respect to the extracellular ones in order to keep the intracellular space potential negative to the extracellular space one. Figure 4.2 shows $Na^+$and K^+ channels and pumps. The sodium-potassium pumps use energy-storing molecules (ATPs) to pump $3Na^+$ to the extracellular fluid whilst pumping one K^+ to the intercellular medium. This yields to a high concentration of Na^+ in the extracellular medium and K^+ in the intracellular medium. Since the membrane is highly permeable for K^+ comparing to Na^+, mainly a concentration gradient diffuses K^+ to the extracellular medium via potassium channels. Through this diffusion outside of the cell gets more positive than its inside inducing an electrical force on K^+ inward. The influx and outflux of ions reach a balance at a voltage such that the concentration gradient and the electrical forces reach to an electrochemical equilibrium. Accordingly, the cell membrane becomes polarized and therefore aiding to the membrane resting potential. For instance, the resting potential in a neuron is about $-70mV$.

Along with aforementioned pumps and channels, there are voltage-gated ion channels across the neurons membrane which are in closed state while resting potential. Once, an excitatory input increases the membrane potential of a neuron to a threshold potential (which varies depending on the conductance of the potassium and sodium, the axon diameter and density of voltage-gated sodium channels), the voltage-gated sodium channels (shown in green in Figure 4.3) open and therefore cause an influx of Na^+ to the intracellular medium. Thus, the membrane potential increases suddenly (depolarization) and an action potential occurs that locally opens more voltage-gated channels. The voltage-gated sodium channels tend to be opened for a short time before they undergo the auto-inactivation. They

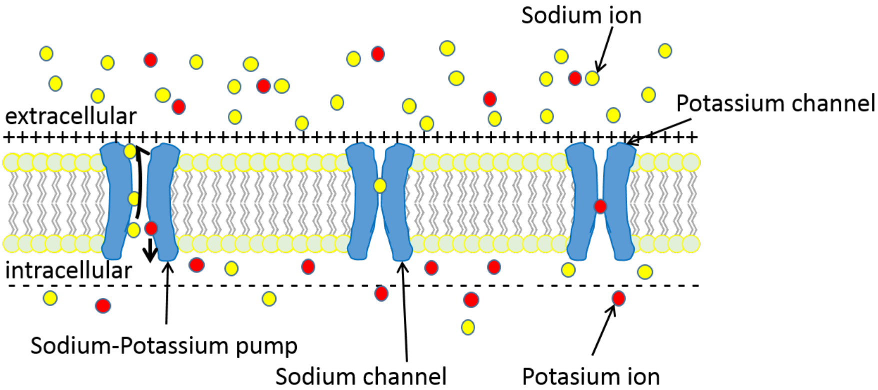

Figure 4.2: Schematic of the sodium and potassium channels and pump on the neuron membrane; The sodium-potassium pumps outflow 3 Na^+ and influx one K^+ causing an ionic gradient concentration across the membrane. Moreover, the membrane permeability for K^+ is quite high, that leads to the diffusing of potassium ions outward the cell through potassium channels. This chemical diffusion lead to an electrical force inward the cell preventing more K^+ reduction. The membrane therefore reaches an electrochemical equilibrium at a voltage known as resting potential.

remain closed after a short refractory period to be ready for the next opened conformation. On the other hand, the voltage-gated potassium channels (shown orange in Figure 4.3) adopt an open conformation in higher potentials. Hence, they lead to an outflux of K^+ and consequently a decrease of the membrane potential (repolarization). These potassium channels tend to stay opened for longer time than the sodium ones to gradually bring the membrane to its resting potential. While the voltage-gated sodium channels are in refractory state, the voltage-gated potassium channels reduce the membrane potential below the threshold potential, which guarantees the unidirectional propagation of the action potential down to the axons.

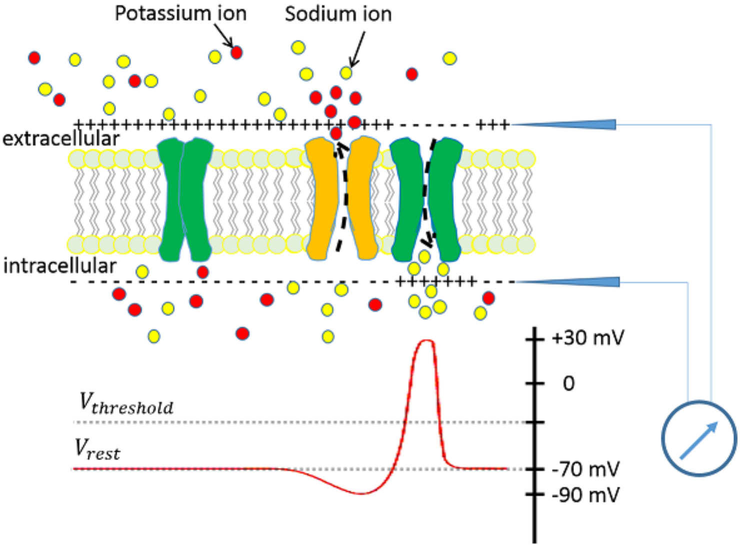

Figure 4.3: Schematic of an action potential; Once, an excitatory input increases the membrane potential of a neurons to a threshold, the voltage-gated sodium channels (green) open and locally depolarize the membrane. In higher potentials the voltage-gated potassium channels (orange) open and decrease the membrane potential. The diagram of the action potential recorded by a voltmeter is schematically shown below.

[54]

Upon receiving the action potential, the information is transferred through synapses from one neuron (presynaptic neuron) to either the other one (postsynaptic neuron) or the environment via the process called synaptic transmission. The information can be transferred by chemicals as messenger or neurotransmitter. Although direct recording of the action potentials is preferable, the tools to measure the neuron's electrical activity such as electrophysiology suffer from low spatial resolution [55]. Moreover, the main direct measurement of neuron activity requires likely invasive, physical contact to the neuronal tissue. This is the main weakness of electrophysiological methods [56]. Alternatively, other neuronal messengers may be used as an indirect measure of neuronal activity. Neurotransmitters and ions can be named as neuronal messengers. Among all neuronal messengers, Ca^{2+} provides a multi-purpose signal related to a variety of functions in different cell types. Ca^{2+} provokes the synaptic transmission in both presynaptic [57] and postsynaptic [58] neurons as well as it regulates gene transcription in the nucleus [59]. Upon membrane resting potential, the cells have a Ca^{2+} concentration of $100nM$ which can rise by ten times once the cells are activated via the Ca^{2+} influx through voltage-gated calcium channels (VGCCs) [60]. Considering before-mentioned characteristics of intracellular Ca^{2+} signaling, it is not surprising that recording Ca^{2+} changes is the most common approach to investigate the activity of a population of neurons *in vitro* [61, 62] and *in vivo* [63, 64]. Similar to instrumentational improvement, the calcium indicators have been undergone several improvements from bioluminescent proteins to synthetic and genetically-encoded calcium indicators or GECIs. The aim has been to provide clear Ca^{2+} dynamic indication with higher temporal resolution and a larger range of fluorescence. [65, 66, 67, 68, 69]

Although the improved syntactic calcium indicators, such as Oregon Green BAPTA and fluo-4, provide high Ca^{2+} affinity, relatively easy but invasive implementation and a large signal-to-noise ratio, the injected dyes diffuse away from the injection sites, leading to the reduction of spatial specificity and a high background signal. Hence, these drawbacks make the synthetic dye inappropriate for long-term imaging [70, 71]. To overcome these limitations, GECIs have been introduced by the Tsien group [72]. GECIs are protein-based calcium indicators which track the Ca^{2+} dynamics with

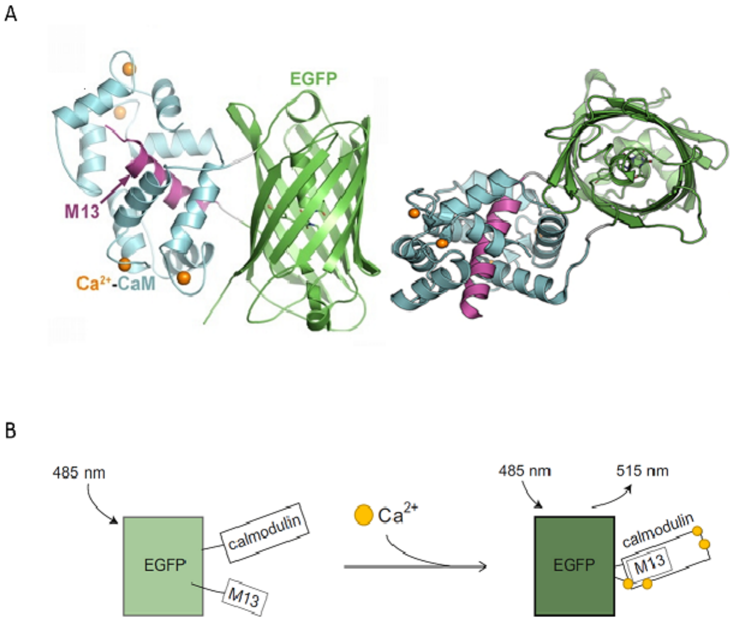

Figure 4.4: GCAMP, a genetically encoded calcium indicator; A) The structure of GCAMP illustrating the EGFP in green, M13 in purple whereas Ca^{2+} are shown with reddish orange spheres and calmodulin (CaM) in cyan. Adopted from [73]. B) The conformational change in presence of Ca^{2+}. Adopted from [57]

fluorescence fluctuations. These indicators can be addressed to a specific compartment or protein in an organ of living organisms via engineering their genome. [55]

Based on their method to indicate the Ca^{2+} propagation, GECIs are categorized into Förster resonance energy transfer (FRET) and single-fluorophore families. The main applied GECIs are the green calcium indicator proteins (GCAMPs) from single-fluorophore family. GCAMPs consist of one enhanced green fluorescent protein (EGFP) which is bound to a hinge-like protein calmodulin with high affinity to Ca^{2+} and to M13, a synthetic calmodulin-binding peptide (Figure 4.4A) [74]. In the absence of Ca^{2+}, the fluorescent proteins exist in a poorly fluorescent state. Once the calmodulin binds to Ca^{2+}, the M13 binds to calmoludin. Thus EGFP can be rapidly de-protonated, causing a high absorbance at the excitation wavelength followed by a bright fluorescence emission (Figure 4.4B). [75, 73]

Due to their characteristics, zebrafishes have been utilized as a suitable model for *in vivo* imaging of neuronal populations [76]. In accordance to whole-brain Ca^{2+} imaging with GECIs, genetic tools have been developed for zebrafish, notably, using the Tol2 system, a highly efficient transgenesis method. [77, 78]

These improvements provide the material for imaging brain activity in zebrafish behaviour, for example, correlating the brain activity with simulation-induced movements in paralyzed larval zebrafish. The fictive movement is caused via electrophysiological methods [79]. Alternatively, genetically encoded manipulators can be used to optically activate a neuron or a population of neurons. In this case the Ca^{2+} propagation is recorded additionally with imaging the fluorescence from the GECIs [80]. It is, however, possible to target functionally defined neuronal compartment expressing light-activated ion pumps and channels [81]. (see chapter 11)

Part II

in vivo light-sheet fluorescence microscope with interchangeable Gaussian and Bessel beam modalities (*in vivo* LSFM)

Chapter 5

Light-sheet fluorescence microscopy

Although light-sheet illumination is not a new concept [82], it has been introduced to the investigation on biological samples, only in 1990's by coining the orthogonal-plane fluorescence optical sectioning to image large fluorescent sample (millimeters in size) with limited spatial resolution [83]. Since then, LSFM has undergone several technical developments such as selective plane illumination microscopy (SPIM) that provides fluorescent images with sub-cellular resolution [84], multidirectional SPIM to reduce illumination artifacts [85] ,multi-views SPIM for improving the spatial resolution in 3D [86] and digital scanned laser light-sheet microscopy that renders structured illumination [87] as well as self-healing beams application. (see Appendix A)

In light-sheet fluorescence microscopy (LSFM), the sample is illuminated with a thin sheet of light and the emitted fluorescence is collected along a detection axis perpendicular to and uncoupled from the illumination one.

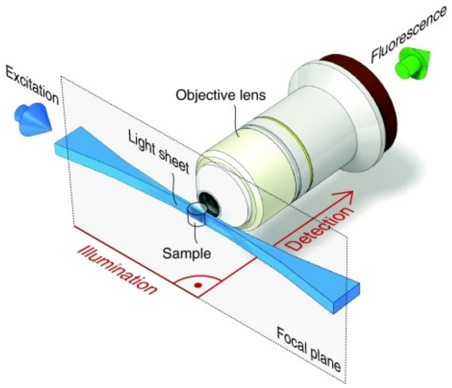

Figure 5.1: Schematic configuration of a light-sheet microscope; The sheet of light is focused along the focal plane of the detection objective. Adopted from [88]

The confinement of the light-sheet illumination with the focal plane of the detection objective allows the optical sectioning (Figure 5.1). This guarantees the fundamental idea of LSFM; applying the optical sectioning via shaping the illumination with simultaneous imaging of the whole detection focal plane (in the field of view of the detector) in a wide-field detection. To obtain a 2D image in LSFM only a thin section is illuminated by the light sheet, therefore phototoxicity and photobleaching are drastically reduced comparing to confocal imaging. In confocal microscopy, the out-of-focus sections of the samples are also exposed to the light whereas, only the in-focus fluorescence is collected (Figure 5.2). This makes the LSFM prominent in long-term 3D imaging, especially *in-vivo*.

The sheet of light is either formed statically by uniaxial focusing a symmetrical laser beam with a cylindrical lens (typically combined with a low-NA objective) or dynamically by rapidly scanning a focused symmetrical Gaussian laser beam across the detection objective focal plane. The latter

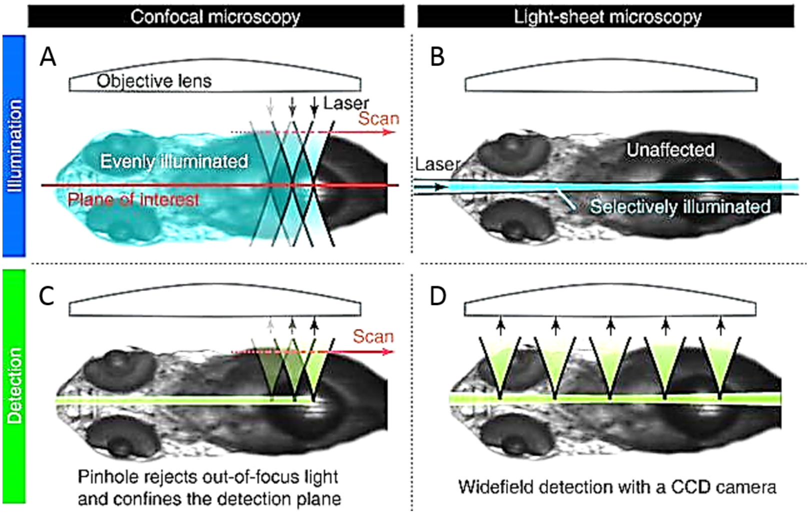

Figure 5.2: Fluorescence generation in confocal microscopy (A and B) compared with LSFM (C and D); A) In confocal microscopy, a focused beam is scanned over a large number of raster positions which illuminate not only the in-focus fluorophores, but also the out-of-focus ones above and below. B) In comparison, in LSFM, a sheet of light illuminates only a thin plane of interest from the side, therefore, it results in a reduction of photobleaching. C) Optical sectioning is obtained by rejection of the out-of-focus photons in confocal microscopy. D) In LSFM, the optical sectioning is achieved by selectively illuminating the plane of interest, hence, the fluorescent photons are collected and imaged simultaneously. Adopted from [88]

approach is called digital scanning laser light-sheet microscopy or DSLM (Figure 5.3). The center of the scanning mirror, the scan lens, the tube lens and the back aperture of the illumination objective are in a $4f$ configuration. This allows the conversion of a tilt movement of the scanning mirror to a step-wise vertical displacement of the Gaussian micrometer-thin focused beam, forming a discontinuous light sheet, perpendicular to the detection direction. The illumination objective focuses the laser beam onto the sample governing the light sheet thickness. [89]
Digitally scanning laser beam offers several advantages in comparison with using a cylindrical lens [87]:

- The light sheet formation in DSLM is flexible. The height of the light sheet can be adjusted respecting the sample size and field of view (FOV) by regulating the tilt angle range of the scanning mirror.

- In DSLM, the laser beam is focused in a single line providing a spatially homogeneous intensity distribution, therefore, even illumination over the light sheet.

- DSLM facilitates the modulation of laser intensity. In other words, the scanning laser beam enables the application of structure illumination, enhancing the image quality. The digital scanned laser light-sheet fluorescence microscopy with incoherent structured-illumination microscopy (DSLM-SI) is introduced by Keller and his colleagues in 2010 [89].

On the other hand, the acquisition rate of a DLSM is limited by the scanning frequency and the height of the light sheet. Moreover, to obtain similar fluorescent yield at the same speed over whole field of view using DSLM,

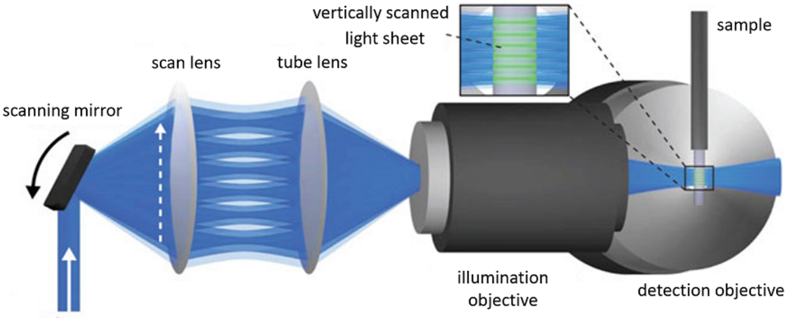

Figure 5.3: Scheme of a digital scanning laser light-sheet microscope; The symmetric Gaussian beam is focused on the detection focal plane. Therefore, the sample is illuminated along a single line scanned vertically along the detection field of view (FOV). A 4f configuration of scanning mirror, scan lens, tube lens and the illumination objective guaranties that the tilt movement of the scanning mirror converts to a vertical displacement of the focused beam at the sample. Adopted from [89]

the sample is exposed to about 300 times higher intensity per location with respect to light sheet illumination using cylindrical lenses. [88]

DSLM has been applied promisingly in long-term (longer than 24 hours) quantitative tracking of large number of cells during embryogenesis development of the entire zebrafish embryo [87] as well as whole brain functional mapping in larval zebrafish [52].

Moreover, scanning a laser beam to produce light sheet illumination facilitates the two-photon LSFM. In this case, the laser intensity is focused along a beam at a moment that fulfils the condition for efficient two-photon excitation eq. 2.23. In LSFM, the radial resolution is the same as in a wide-field microscope given by revising eq. 2.13 using eq. 2.10

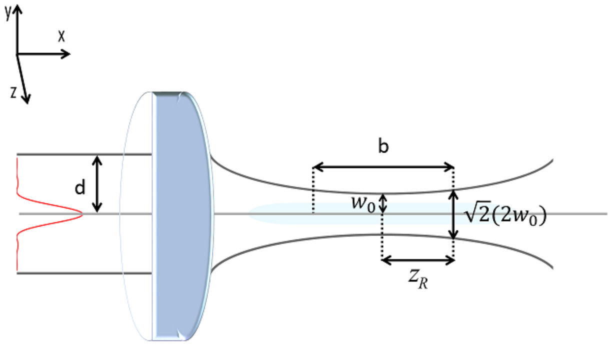

Figure 5.4: A symmetrical Gaussian beam focused by a lens; d denotes the $1/e^2$ half width of the incident beam, w_0 the focused beam waist and b the confocal parameter.

$$FWHM_{lateral} \approx 0.84 \left(\frac{0.61 \lambda_{det}}{NA_{det}} \right) \tag{5.1}$$

λ_{det} for the emission wavelength and NA_{det} is the numerical aperture of the detection objective. The axial resolution is usually related to the thickness of the light sheet. In many cases the light sheet thickness is smaller than the axial extend of the detection PSF, in other words, the light sheet governs the thickness of the optical section not the detection objective. The thickness of a Gaussian beam focused by a single lens or an objective lens (Figure 5.4) with the focal length of f is inverse proportional to the $1/e^2$ incident beam radius (d):

$$w_0^{Gause} = \frac{\lambda f}{\pi d} \tag{5.2}$$

where λ is the incident wavelength and n the refractive index of the medium. In general, for a Gaussian beam, waist and FWHM are correlated

$$FWHM = \sqrt{2\ln 2}w_0^{Gause} \tag{5.3}$$

therefore, the axial resolution of an LSFM can be obtained by equating eq. 5.2 and eq. 5.3:

$$FWHM_{axial} \approx 1.177\frac{f_{ill}\lambda_{ill}}{\pi d} \tag{5.4}$$

where fill denotes the illumination lens (objective) focal length and λ_{ill} the illumination wavelength. In case of LSFM, the useful field-of-view is defined by the height of light sheet times b of the focused Gaussian beam. The confocal parameter is two time the Rayleigh range (z_R) that is defined by beam elongation in x axis where its width is no larger than 2 time of its minimum width ($2w_0^{Gause}$) (Figure 5.4)

$$b = 2z_R = \frac{2\pi n(w_0^{Gause})^2}{\lambda_{ill}} \tag{5.5}$$

The light sheet height (in DSLM) is defined by the scanning mirror angle which varies depending on the size of the specimen and the desired acquisition rate.

As it is shown in eq. 5.5, the FOV and the axial resolution are correlated such that to achieve a larger FOV, the thickness of the light sheet should be increased therefore the axial resolution is subjected to be lower. This causes an anisotropy in spatial resolution while means that to obtain a large

FOV, the axial resolution becomes lower than the radial one. Multi-view imaging techniques have been applied to LSFM [86, 90] in which data is acquired from multiple views by rotating the sample. The data which is poorly resolved in one view is acquired with high resolution in another one, so resulting in isotropic spatial resolution.

Another consideration is occurred while imaging the highly scattering specimen, such as biological samples with light-sheet microscope. Both the light sheet and the fluorescence are scattered when passing through the biological sample. This causes the expansion of the light sheet, therefore, exciting out-of-focus fluorophores and blurriness of the images. Furthermore, the peak intensity of the illumination light sheet decreases deeper in the sample.

To reduce the contribution of out-of-focus fluorescence, the confocal principle has been implemented in the detection path of DSLMs by either placing a slit [91] or by using the rolling shutter of a scientific CMOS camera (sCMOS) as a virtual slit [92]. This enables LSFM to improve the optical sectioning whilst the photobleaching and phototoxicity is decreased [93]. Moreover, two-side illumination has been used to overcome the reduction of peak intensity providing even illumination across the sample. This approach, along with pivoting the light sheet, reduces shadowing artifact drastically [85]. Another approach is to use the unique characteristics of Bessel beam illumination that will be discussed in chapter (6). Application of this approach has shown the reduction in the resolution anisotropy [94], shadowing artifact and improvement in maintaining the peak intensity of the illumination [95].

Chapter 6

Bessel beam illumination

The optical phenomenon of diffraction is an essential property that is caused by the wave nature of light. Diffraction of light results in not only light interference in the presence of an obstacle but also in spreading of the light when it propagates in free space. This results in the alteration of the beam shape in scattering media as well as limited depth-of-focus of a beam. Gaussian beams are exemplar that are subject to light diffraction. In the quest for a light beam resistant to diffraction that its light field is immune to spread when propagating in free space, nondiffracting light beams, e.g. Airy beams [96], some form of Laguerre-Gaussian (LG) beams [27] and Bessel beams [97], have been introduced. Both Airy beams and Bessel beams reconstruct their shape in a short propagation distance after an obstacle (self-reconstructing property) comparing to LG beams (in order of the Rayleigh length) [98]. However, application of Bessel beams with symmetric profile in microscopy is advantageous comparing to the curved profile of Airy beams.

The nondiffracting property of a Bessel beam has been formalized by Durnin

[97] for a wave, $U(\vec{r},t) = U(\vec{r})e^{i((2\pi k_z z)-\omega t)}$ with planar wave front whose complex amplitude, $U(\vec{r}) = A(r,\varphi)e^{-ik_z z}$ is an exact solution of Helmholtz equation[1],

$$\nabla U(\vec{r}) + kU(\vec{r}) = 0 \tag{6.1}$$

where k is the wavenumber. $A(r,\varphi)$ is derived as

$$A(r,\varphi) = A_m J_m(k_r r)e^{\pm im\varphi}, m = 1, 2, ... \tag{6.2}$$

where A_m is constant, J_m denotes the m^{th} order Bessel function of the first kind, r, φ and z are the radial, azimuthal and longitudinal coordinates components, respectively and the wavenumber (k) is given by

$$k = \sqrt{k_z^2 + k_r^2} = \frac{2\pi}{\lambda} \tag{6.3}$$

where λ stand for the wavelength of the Bessel beam. For $m = 0$, we have the J_0 Bessel beam formulated as

$$U(\vec{r}) = A_0 J_0(k_r r)e^{-ik_z z} \tag{6.4}$$

which has a complex amplitude and hence, a planar wavefront. Its intensity distribution $I(r,\phi,z)$ turns out to be variable radially and independent from

---

[1] A mathematical function, U that satisfies wave function,$\nabla^2 U(\vec{r},t) = -\frac{1}{c^2}\frac{\partial U(\vec{r},t)}{\partial t^2}$, is known as a wavefunction. Solving wave equation for given $U(\vec{r},t)$ leads to a differential equation that is known as Helmholtz equation. [23]

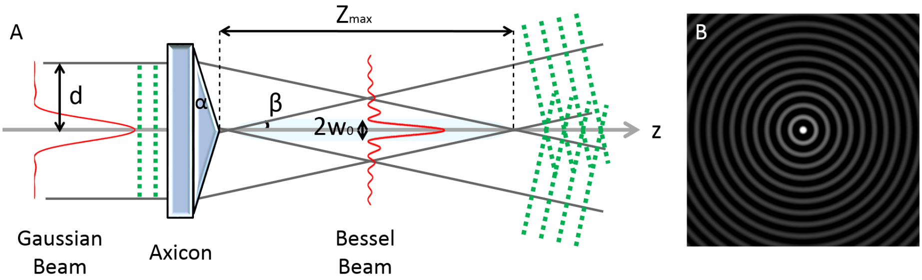

Figure 6.1: Generation of Bessel beam with an axicon; A Gaussian beam with a radial intensity profile shown in A with the beam radius of d passes through an axicon. The interference pattern generated by axicon forms a J_0 Bessel beam approximation. The radial intensity of the J_0 beam is shown B. The red profiles present the beams intensity distribution over x axis, accordingly and the dotted green lines show the wavefronts of the beams. z_{max} and w_0 are the depth of focus and the waist of the Bessel beam respectively. The propagation is from left to right on z axis.

the propagation distance (z). Thereby, the optical power remains confined.

$$I(r, \phi, z) = A_0^2 J_0^2(k_r r) \tag{6.5}$$

Theoretically, in a Bessel beam, the intensity can spread over an infinite number of rings which means they can carry infinite power [99]. Whereas, experimentally, a quasi-Bessel beam can be created that exhibits the aforementioned properties over a finite distance [100].

The approximation of a Bessel beam can be made via different approaches. The 0^{th} order Bessel function of first kind (J_0) is the Fourier transfer of an ultrathin ring, so by placing a circular slit at the back focal plane of a lens, the J_0 Bessel beam can be made [94, 100]. Although, this approach has proven the properties of Bessel beams, it has been evidently inefficient because of blocking the main portion of the incident Gaussian beam power. There are more efficient methods to create the Bessel beams such as holographic techniques. The holograms can be static or variable holograms by using programmable spatial light modulators [99, 101]. Another efficient approach is focusing a Gaussian beam with an axicon [102], a cone-shape lens (Figure 6.1). When the incident light rays pass through an axicon, it generates an interference pattern that takes the form of a J_0 Bessel beam [103]. For each point ($P(x, y, z)$) within the range of the Bessel beam depth-of-focus ($z \leq z_{max}$), the intensity distribution ($I(x, y, z)$) is given by [104]:

$$I(x, y, z) = \frac{4\pi^2 E^2(d)}{\lambda} \frac{d sin\beta}{cos^2\beta} J_0^2 \left(\frac{2\pi sin\beta \sqrt{x^2 + y^2}}{\lambda} \right) \tag{6.6}$$

where $E^2(d)$ is the energy of the incident beam with radius d and λ the wavelength of the propagating light. The angles α (the axicon opening angle), $\beta = (n - 1)\alpha$ (the Bessel beam propagation cone half angle that is corresponding to the numerical aperture of the axicon with a refractive index of n) and the incident Gaussian beam waist (d) define the generated Bessel beam depth-of-focus (z_{max}):

$$z_{max} \approx \frac{d}{\beta}. \tag{6.7}$$

As shown in eq. 6.7, the depth-of-focus of the Bessel beam can be regulated by adjusting the incident beam diameter entering the axicon (d). The radius of the central core of the generated Bessel beam,

$$w_0^{Bassel} = \frac{0.383\lambda}{\beta} \tag{6.8}$$

being 38% narrower than the airy radius of a system, eq. 5.2 with similar numerical aperture [104]. The confocal parameter (depth-of-focus) of a Gaussian beam, eq. 5.5, is proportional to the square of beam waist (w_0^{Gauss}) where a Bessel beam depth-of-focus (z_{max}) is linearly proportional to incident beam waist (d). This results in the fact that a Bessel beam provides narrow central spot over larger propagation ranges comparing to a Gaussian one. Considering the Bessel beam wavefront which propagates on a cone (green dotted lines in Figure 6.1A), the self-healing property of Bessel beams can be discussed. In the case of the presence of an obstacle in the center of the beam, the light rays that propagate in larger angles pass over the obstacle and construct the interference pattern and therefore illuminate the shadowed volume. The distance behind the obstacle in which the Bessel beam reconstruct its shape is given by [99]:

$$z_{min} = \frac{a}{2\sqrt{1-\beta^2}} \tag{6.9}$$

where a is the width of the obstacle (Figure 6.2). This plays an important role when imaging live samples such as larval zebrafish. A drawback of Bessel illumination approaches in fluorescence imaging, e.g. in LSFM, is the excitation of the sample by the side lobes of the Bessel beam. This results in out-of-focus fluorescence, therefore, reduction of contrast. Implementation of a confocal principle (see chapter 5) is necessary. Furthermore, the energy is shared over the number of the rings of the Bessel beam and this causes

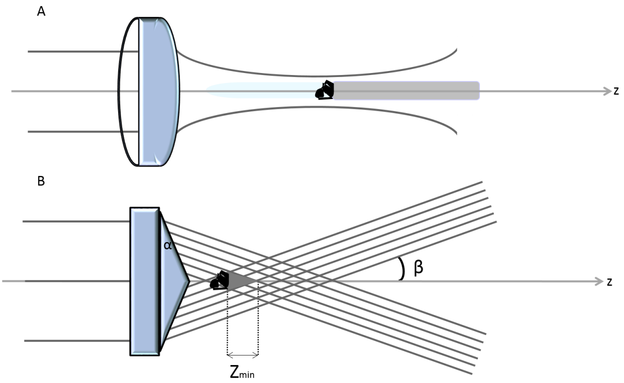

Figure 6.2: Reduction of shadowing with Bessel beam illumination; A) If we place an obstacle in the center of a Gaussian beam, it creates a shadow along the propagation direction. B) In case of a Bessel beam, the inference takes place after the obstacle and reconstructs the shape of the beam.

reduction of the peak intensity and therefore lower image contrast. Thus, Bessel beam illumination requires higher beam power in comparison with Gaussian one. Utilizing the Bessel beam illumination combined with LSFM has led to high-resolution fast imaging of fixed or living specimens that can be cells or more complex organs.[94, 95, 105, 106]
To achieve the benefits of both Gaussian and Bessel beam illumination approaches, we have made a confocal Gaussian/Bessel illumination light-sheet fluorescence microscope aiming high-fidelity neural activity imaging, specifically the brain function of living zebrafish. The setup is explained in details in chapter (7).

Chapter 7

in vivo LSFM; setup

Imaging Ca^{2+} signals *in vivo* is done by our custom-built DSLM with interchangeable Gaussian and Bessel beam illumination that is called *in vivo* Light-sheet Fluorescence microscope (*in vivo* LSFM). In this chapter, the main compartments of *in vivo* LSFM are discussed; the optical setup that includes illumination and detection optics, the specimen compartment including the specimen chamber and heating system, mounting the sample and the positioning platform and finally the electronics and custom-made control software. A list of the main components of *in vivo* LSFM is presented in 7.1.

7.1 Illumination unit

The *in vivo* LSFM is equipped with an externally doubled diode laser (Excelsior $488nm$, $50mW$, vertical polarization, Spectra-Physics, Newport Corporation) that was chosen for Ca^{2+} imaging using GCaMP (Figure 7.1). The laser beam is collimated and expanded by a telescope made of singlet

Table 7.1: A list of the *in vivo* LSFM components

Component	Manufacturer	Model	Specifications
Lasers	Spectra-Physics, Newport Corporation, United States	Excelsior	$488nm$, $50mW$, vertical polarization
AOTF	AA Opto-Electronic, France	AOTFnC-400.650-TN	$> 90\%$ diffraction efficiency, $3 - nm$ resolution, low crosstalk between laser lines, high separation angle
Axicon	Thorlabs, United States	AX251-A	$1.0°, 350 - 700nm$ AR Coated UVFS, $\varnothing$1”
Galvanometer scanner	Cambridge Technology, United States	VM2500+	Small angle step response 200μs
Objectives	Olympus, Japan	UPLFLN 4X	$4x0.13$ NA, $WD17mm$, EFL $45mm$ (illumination)
	Olympus, Japan	XLUMPLFLN 20XW	$20x1$ NA, WD $2mm$, EFL $9mm$, water immersion (detection)
Cartridge heater	RS Pro, RS Component, United Kingdoms	MHI01120	Cartridge heater, $\varnothing 6.5mm$, length $40mm$, $30w$, $220vac$
Temperature controller	Omron, RS Components, United Kingdoms	E5CN-HC2M-500	PID temperature controller, $48x48mm$, 2 output current, $24vac/dc$ supply voltage
Sample stages	Physik Instrumente, Germany	C-863.11	DC servo-motor controller
		M-122	Precision Micro-Translation Stage, Travel range $25mm$, $0.1\mu m$ resolution, max. velocity $20mm/s$
		M-116	Precision Rotation Stage $2.5\mu rad$ resolution, max. velocity $20deg/s$
Objectivesstages	Physik Instrumente, Germany	M-105.10	Precision Cross Roller, $18mm$, $1\mu m$ resolution
Camera	Hamamatsu, Japan	Orca Flash 4.0 v2.0	sCMOS sensor, $2048(H)x2048(V)$, cell dim.: $6.5\mu m$, active area: $13.3, mmx13.3mm$, 16 bit images
DAQ board	National Instruments, United States	NI PCIe-6259	AI: $1MS/s$ multichannel; 16-bit resolution, 10 V; AO: $2.86MS/s$, 16-bit resolution, $10V$; digital I/O: software/hardware timing up to 10 MHz, 100 MHz max source frequency, TTL logic level
Workstation 1	Dell, United States	Precision T5810	32 GB RAM, Intel Xeon CPU E5-1630 V3 at 3.70 GHz, OS Windows 7 64 bit
Workstation 2	Dell, United States	Precision T7810	32 GB RAM, Intel Xeon CPU E5-2630 at 2.40 GHz, OS Windows 7 64 bit

lenses ($f1 = 80mm$ and $f2 = 200mm$). From here on, all lenses are achromatic doublets with anti-reflecting coating for the visible spectrum unless otherwise mentioned. The beam is guided to an acousto-optical tunable filter (AOTF). The AOTF acts as a fast (μs) controllable intensity modulator. In the AOTF there is a transparent birefringent crystal (e.g. tellurium dioxide or Te_2O) that is bound to a transducer. When the transducer is driven with a radio-frequency wave, it vibrates and hence generates high-frequency acoustic wave traversing across the crystal. The ultrasonic wave periodically modulates the refractive index of the crystal. The periodic modulation of the refractive index acts a phase grating; a light beam enters the crystal at the Bragg angle is subjected to Bragg diffraction. Varying the amplitude of the traversing acoustic wave, the intensity of the diffracted output is modulated. The AOTF light transmittance is measured at different radio-frequency amplitudes to determine a lookup table for linearizing the AOTF response. The nondiffracted transmitted beam is filtered out by an iris. From here, the illumination beam can be chosen between Gaussian beam (Figure 7.1A) or Bessel beam (Figure 7.1B) by flipping mirrors (fm1 and fm2):

7.1.1 Gaussian beam

When the flipping mirrors are down, the Gaussian beam originating from the diode laser (Table 7.1) is re-collimated and shrunk by a telescope made of lenses ($f1 = 125mm$ and $f2 = 100mm$). This is due to the beam diameter required for desired Gaussian light sheet thickness (see section 7.1.3). The collimated beam ($1/e^2$ beam radius of $1.4mm$) is reflected onto the center of a galvanometric scanning mirror (galvo).

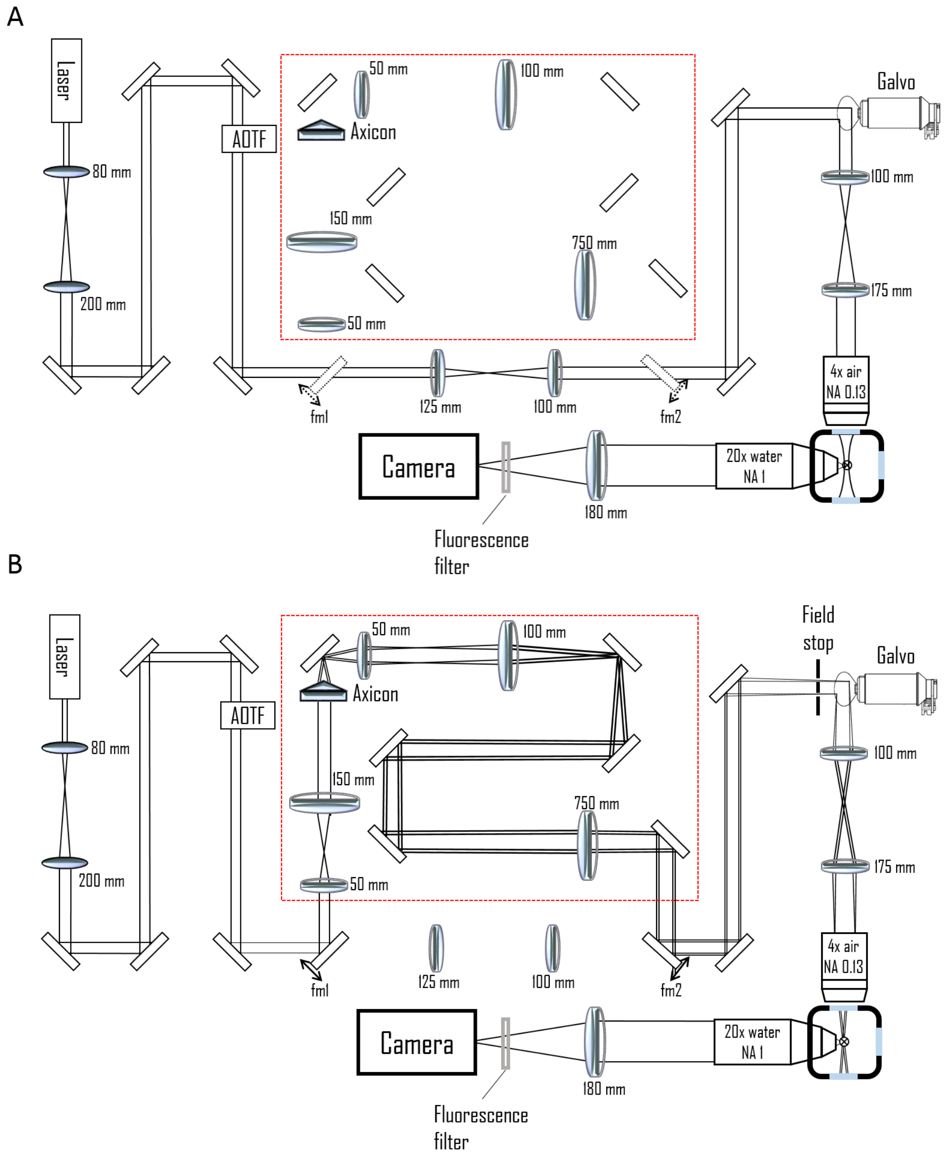

Figure 7.1: Optical setup top view; Schematic representation of the light path of A) Gaussian LSFM and B) Bessel LSFM. The illumination objective focuses the incident beam (Bessel/Gaussian) through a coverslip at the center of the specimen chamber where it coincides with the focal plane of the detection objective. fm: flipping mirror, blue rectangle: coverslip, red-dotted rectangle: Bessel beam shaping unit. The beam diameters and focal distances are partly retouched for better illustration.

7.1.2 Bessel beam

A flipping mirror ($fm1$) reflects the Gaussian beam to a telescope ($f1 = 50mm$ and $f2 = 150mm$ ⌀2") that collimates the beam and expands its radius to $2.6mm$. This beam expansion is required to lower the residual Gaussian beam after the axicon ($\alpha = 1.0°, n = 1.46$ @ $550nm$). The residual is in fact the on-axis Gaussian light that is not refracted by the axicon round tip. The axicon generates a J_0 Bessel beam that is contaminated with residual Gaussian beam. The Bessel beam depth-of-focus and central core waist are quantified by eq. 6.7 and eq. 6.8 to be $327mm$ and $23.3\mu m$, respectively. A lens ($f = 50mm$) takes the Fourier transform of the Bessel beam to a ring with an external radius of $0.4mm$ at its focal plane. The ring is then expanded by a telescope ($f1 = 100mm$ ⌀2" and $f2 = 750mm$ ⌀2") at the galvo surface in a 4f configuration (ring external radius, $3mm$). A second flipping mirror (fm2) is placed on the optical path to reflect the Bessel beam to a common path with Gaussian beam illumination. An annular aperture is placed just before the galvo surface to filter out the residual Gaussian beam.

7.1.3 Light sheet generation

At this end, the illumination beam is aligned at $100mm$ above the optical table (Figure 7.2). An upward 45° mirror deflects the beam to the center of the galvo ($165mm$ above the optical table) such that they form a periscope. A telescope ($f1 = 100mm$ and $f2 = 175mm$) images the center of the galvo onto the back aperture of the illumination objective ($4x$, $0.13NA$, $WD17.5mm$, Olympus) in a $4f$ configuration. Hence, the galvo is in a conjugated plane with respect to the illumination objective. This guarantees that an angular step of the galvo is converted into a vertical displacement

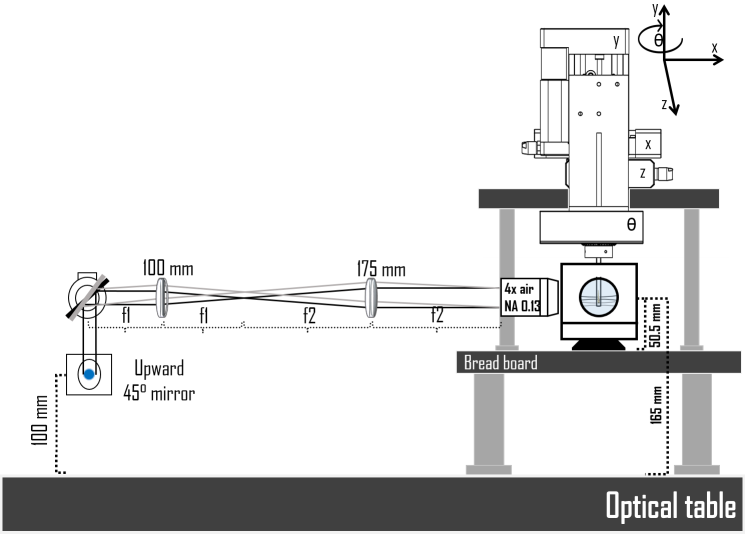

Figure 7.2: Light sheet generation; The laser beam is directed to the center of galvo by an upward 45° mirror. The beam (black) is reflected horizontally to the telescope ($f1 = 100mm$ and $f2 = 175mm$) that adjust the beam diameter entering the illumination objective. While scanning, galvo reflects the beam in different angle to the telescope (gray). Thereof, the center of the galvo mirror and the lenses are in a $4f$ configuration with the back aperture of the illumination objective, the angular movement of the galvo is converted to the vertical sweeping of the focused beam in the specimen chamber.

of the beam across the specimen. The telescopes are designed to achieve a $1/e^2$ beam radius of $1.225mm$ for the Gaussian beam at the back aperture of the illumination objective. In the case of the Bessel illumination, the telescope ($f1 = 100$ and $f2 = 175$) after the galvo, expands the light ring to the back aperture of the illumination objective. The external diameter of the ring at illumination objective back aperture is $10.5mm$. To adjust the beam waist position across the specimen and in center of the camera FOV, the illumination objective is placed on a manual translation stage (Precision Cross Roller, $18mm$, Physik Instrumente). A homogeneous light sheet is generated by scanning the beam with the galvo across the detection focal plane. Each angular step of the galvo is synchronized corresponding to the line exposure time of the camera (see section 7.5). This results, by equating eq. 5.2 and eq. 5.5, in a Gaussian light sheet that is $\sim 5.7\mu m$ thick (corresponding to $FWHM_{axial} \approx 6.7\mu m$) with the confocal parameter of $\sim 557.5\mu m$ that fills 83.7% of the camera FOV. Whereas, in Bessel beam scenario, the illumination objective re-produces the J_0 Bessel beam (corresponding to an inverse Fourier transform of the ring with $10.5mm$ external diameter). This results in a Bessel light sheet with a thickness of $\sim 2.46\mu m$ (corresponding to $FWHM_{axial} \approx 2.9\mu m$) over a $\sim 2044.7\mu m$ depth-of-focus quantified by eq. 6.8 and eq. 6.7, respectively. The height of the light sheet is adjusted to camera FOV being $665.6\mu m$. To align the center of the specimen chamber to the illumination propagation axis, the whole specimen compartment is mounted on a breadboard (UltraLight High-Stiffness Breadboard, $300x300x25mm$, $M6$ Taps, Thorlabs) that is placed $114.5mm$ above the optical table.

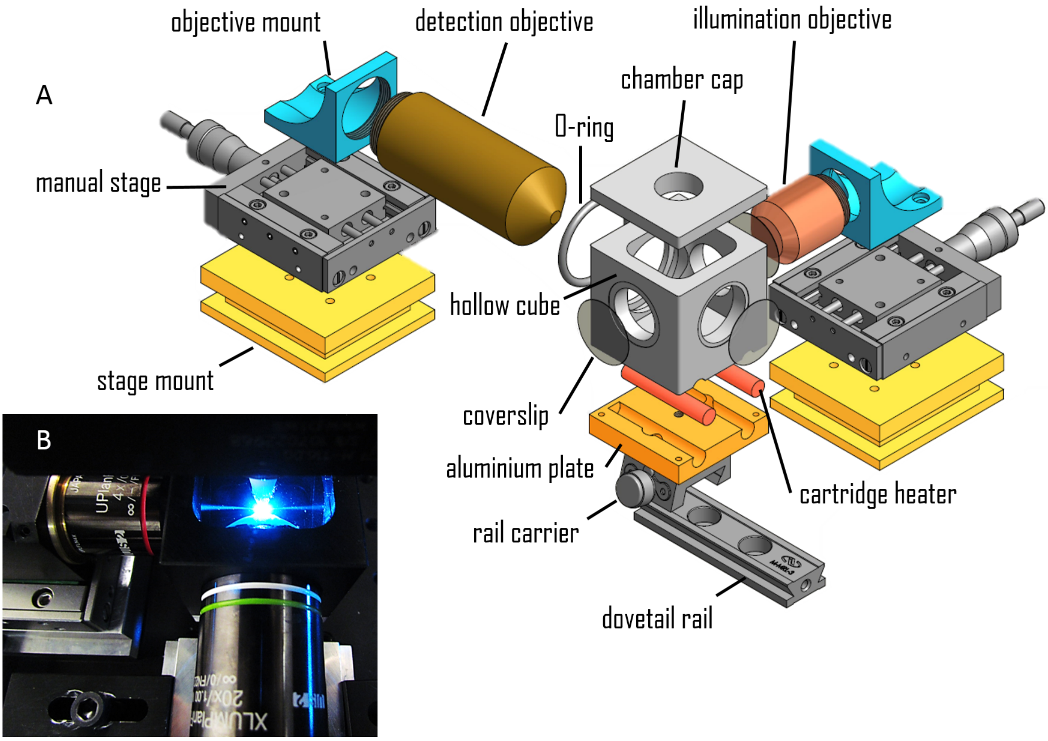

Figure 7.3: Specimen compartment; A) The specimen chamber is a hollow cube with four holes that three of the are water-sealed with coverslips. The 4th hole encounter the detection objective where is water-sealed by using an O-ring. The specimen chamber is equipped with two cartridge heater that mounted on an optical rail with an aluminum plate. The objectives are mounted on manual stages and a mount to adjust the light sheet in the detection FOV. B) A photograph of the specimen chamber with the objectives.

7.2 Specimen compartment

A custom specimen chamber made from aluminum (Figure 7.3) was designed that features four circular holes on the vertical facets. Three of the holes are water-sealed by circular cover slips ($No.1.5$, $\varnothing 25mm$, Menzel Gläser) using silicon sealant, the fourth one encounters the detection objective. The specimen chamber is a hollow cube with $44mm$ edges to match the working distance (WD) of the illumination objective. The specimen is immersed and imaged in fish water ($150mg$ Instant Ocean, $6.9mg$ NaH_2PO_4, $12.5mg$ Na_2HPO 4 per 1L of dH_2O) with refractive index of 1.33. The illumination objective is designed for air immersion that has a working distance of $17mm$ but the specimen chamber is filled with fish water for *in vivo* imaging. The effective working distance can be quantified by applying basic geometry and Snell's law[1]:

$$WD_{effevtive} = WD + d\left(1 - \frac{1}{n_{water}}\right) \tag{7.1}$$

where d is the light path in water. The illumination objective focuses the incident beam (Bessel/Gaussian) through a coverslip at the center of the specimen chamber where it coincides with the focal plane of the detection objective. Hence, given $d = 22mm$ results in $WD_{effective} = 22.46mm$. When the detection objective is mounted, $25ml$ of fish water is required to fill the specimen chamber. An aluminum plate (Figure 7.3) is screwed to the bottom of the chamber for mounting the heating elements. Two heating rods (Cartridge Heater, RS Component) are mounted on the aluminum

---

[1] When a light beam (or other waves) passes the boundary of two media with different refractive indices (n_1 and n_2) with given incidence angle (θ_1), it is subjected to deflect to a refraction angle (θ_2): $n_1 sin\theta_1 = n_2 sin\theta_2$

plate at bottom of the specimen chamber (Figure 7.3) and connected to a temperature controller (Omron PID Temperature Controller, RS Component). The temperature inside the specimen chamber is set to $28.5°C$ monitored via a thermocouple (PRO K Type Thermocouple, RS Component) that is connected to the temperature controller. The specimen chamber with heating plate is then mounted on an optical rail (Dovetail Rail and Rail Carrier, Thorlabs) for ease of removal in the case of the adjustments and repairs.

7.3 Sample mounting and positioning unit

The experiments were performed on $3-6dpf$ larval zebrafish expressing $GCaMP6s$ in almost all neurons' cytoplasm $[elavl3 :: GCaMP6s]$ or nuclei $[elavl3 :: H2B :: GCaMP6s]$. The $1dpf$ larvae are raised in 0.003% 1-phenyl 2-thiourea (PTU or N-Phenylthiourea 97%, Sigma Aldrich) unless otherwise mentioned. PTU inhibits the skin pigmentation and is used to produce transparent larvae. The larval zebrafishes are kept in $1mM$ d-tubocurarine (Tubocurarine chloride pentahydrate, $\geq$ 97.0% (TLC), Sigma Aldrich) for $10minute$ to immobilize them. Then, they are transferred into a reaction tube containing 1.5% low gelling agarose (Agarose, low gelling temperature, Sigma Aldrich) in fish water and kept at $38°C$. The larval zebrafish is then sucked with a syringe inside a glass capillary (Thick/Standard wall Borosilicate with Filament, outer/inner diameters:$1.5/0.86mm$, Shutter Instrument) and kept horizontally in room temperature to let the agarose be polymerized. Afterwards, the low melting agarose gel is extruded out of the capillary such the head of the larval zebrafish is just out of the capillary (Figure 7.4A). Finally, the glass capillary containing the larval zebrafish embedded in agarose gel is inserted into a sample holder (Figure 7.4B), fixed

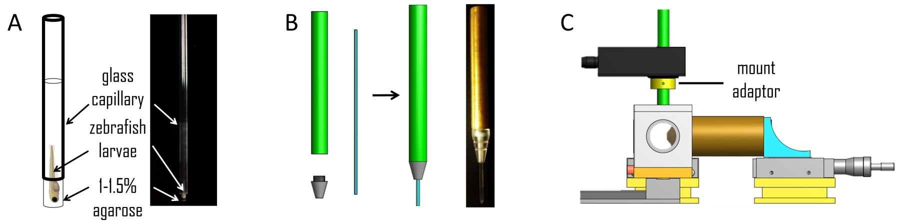

Figure 7.4: Sample mounting; A) a larval zebrafish is immobilized upside-down in $1-1.5\%$ agarose gel inside a glass capillary. B) the glass capillary is then inserted in a custom-made capillary holder and fixed with a grip head. C) the capillary holder is finally fixed inside specimen mount adaptor that is screwed to the rotating element of the position unit.

with a grip head (Grip head 2, Eppendorf) and mounted on the poisoning unit with a custom-made adaptor (Figure 7.4C).

The positioning unit consists of a rotor motor stage (Precision Rotation Stage, $2.5\mu rad$, max. velocity $20 deg/s$, physik Instrumente) through which the capillary holder is mounted. The rotor stage rotates the specimen around the vertical (y) axis (Figure 7.5) and allows data acquisition in different directions.

The light sheet of the *in vivo* LSFM is fixed. Hence, the specimen is moved along the detection optical and the illumination propagation axes to be positioned at the center of the light sheet through the common focal plane. Three translation motor stages (Precision Micro-Translation Stage, travel range $25mm$, max. velocity $20mm/s$, Physik Instrumente) are mounted perpendicular to each other to move the specimen along the three dimensions. The z-axis (detection axis) motor stage is mounted on a custom-made breadboard higher than the specimen chamber to provide just enough space to access the specimen holder. Another translation motor stage is perpendicularly mounted on the z-axis motor stage that allows the sample movement along x axis (illumination propagation axis in the chamber). The third motor stage that moves the sample in y axis (light-sheet height axis) is mounted vertically on the x-axis one by using a custom perpendicular bracket (shown in navy in Figure 7.5A). To mount the rotor stage to the xyz translation platform, an L-shape bracket is designed (Figure 7.5B). One facet of this bracket is mounted on the y-axis motor stage. The other facet of the L-shape bracket has a hole where the rotor stage is mounted. The rotating element of the rotor stage where the specimen mount adaptor is placed, is facing down to the specimen chamber. The specimen holder is mounted on the positioning unit through the L-shape bracket and the rotor stage and finally fixed with three screws to the specimen mount adaptor. Of note, the custom-made brackets are designed to compensate the assembly stability and minimizing the torque on the motor stages, especially the z-axis motor stage. For instance, the perpendicular bracket is a hollow right triangular prism made from aluminum to the minimal extend required with chamfered edges.

7.4 Detection unit

The fluorescence, as discussed in chapter 5, is collected in a wide-field detection configuration. Since the aim is to image living biological specimen, a water-immersing objective ($20x$, $1.0NA$, $WD2mm$, Olympus) is used in the detection unit (Figure 7.1). The detection objective is mounted on a manual stage (Precision Cross Roller, 18 mm, Physik Instrumente) for adjusting its focal plane to the light sheet. The residual illumination light is filtered out by an EGFP band pass filter ($517/20nm$ BrightLine single-band bandpass filter, Semrock) when the collected fluorescence is focused

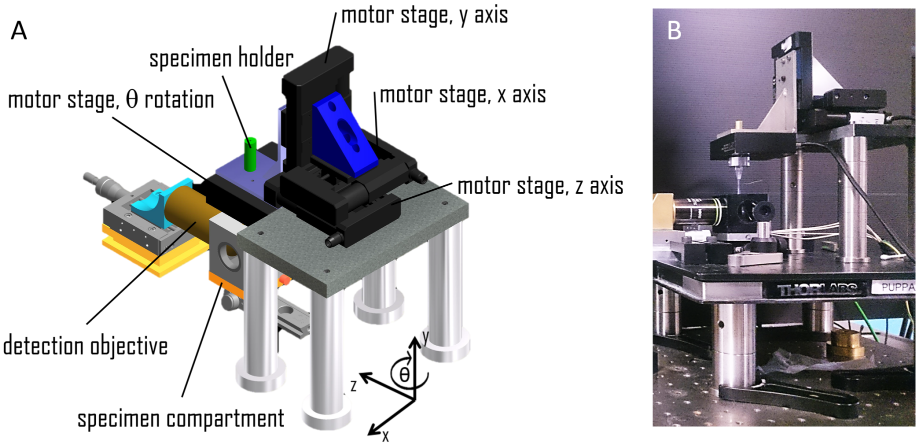

Figure 7.5: Positioning unit; A) Schematic representation of the specimen compartment and the positioning unit. The coordinate system denotes degrees of freedom for moving the sample along all the illumination propagation (x) axis, the elongation of the light sheet height (y axis) and detection direction (z) axis as well as rotating the sample. B) A photograph of the specimen holder mounted on the positioning unit inside the specimen compartment

by an achromatic doublet lens ($f = 180mm$, $\varnothing 2$") on the sCMOS chip of the camera ($OcraFlash4.0v2$, $2048x2048pixels$, Hamamatsu) forming the primary image. The pixel pitch (P) of the camera is $6.5\mu m$. With magnification of the detection objective, $M = 20$, the pixel pitch in object space (Pobject) becomes $0.325\mu m$. Hence, the camera FOV in the object space is $(665.6\mu m)^2$. The camera acquires images in rolling shutter mode, in which only a subset of neighboring horizontal pixel lines is exposed at any time. The active region is then moved over the sCMOS chip from the top to the bottom acting as a virtual confocal slit [92]. A delay between exposing each two neighboring line is applied equivalent to the minimum time required for a single line read-out. This delay acts as a shutter, therefore, the time for the delay is called shutter time ($t_{shutter}$) that is set to $9.7\mu s$. By setting a line exposure time, t_{line}, the active region width in object space (in other words, the width of the virtual confocal slit) can be calculated as $s = (t_{line}/t_{shutter})(P_object)$ and adjusted according to the illumination beam width. The camera is run in external trigger mode using the internal clock of the DAQ board used as the clock. The same clock from the DAQ board used for driving the galvo in a way that a galvo step is corresponding to a line exposure time results in confocal detection.

7.5 Real-time electronics and data acquisition

A schematic representation of the hardware organization is shown in Figure 7.6. A workstation (Precision T5810, Dell, see Table 7.1) is dedicated to control the camera as well as managing the enormous volume of the acquired data via camera link. This workstation is equipped with 4 solid-state derives (SSD) that are configured in a redundant array of independent disks (RAID) of level 0, resulting in a virtual drive of 8 TB volume. It

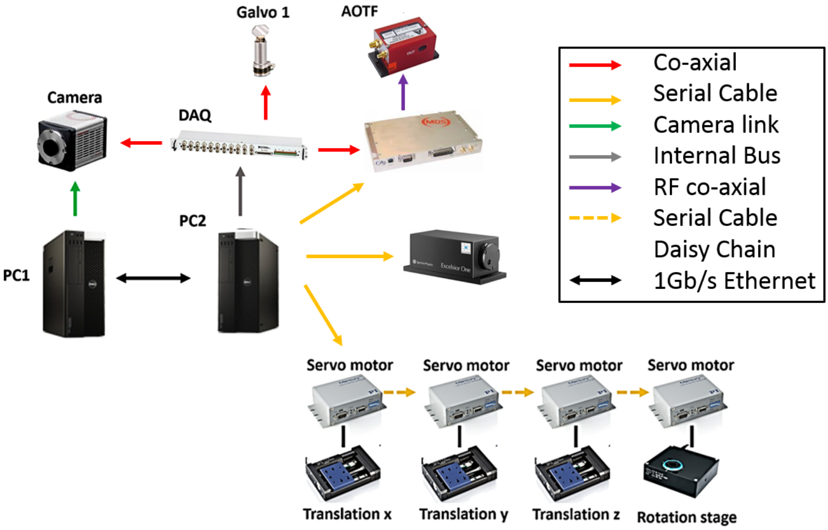

Figure 7.6: Real-time electronics; A workstation (PC1) is dedicated to control the camera and the acquired images via a cameral link. The 2^{nd} workstation (PC2) controls the other electronic component via either serial cables or an installed DAQ board while communicating with PC1 via Ethernet.

is essential to utilize the advantages of RAID0 configuration not only for creating larger drive volume but also achieving higher rate in writing data on disk [107]. This will be necessary in case of long-term whole-brain (3D) Ca^{2+} imaging. OrcaFlash camera acquires 16-bit images with 2048 by 2048 resolution and no compression, hence, each image occupies 8 MB on disk. The camera frame rate being 50 frames per second, the data production rate of our LSFM results in $1.37 TB/h$.

The other hardware components are controlled by a second workstation (Precision T7810, Dell) that is equipped with a DAQ board (NI PCIe-

6259, National Instruments). The hardware components are connected to the workstations either via computer ports such as USB and CameraLink or via analog and/or digital input/output by the DAQ board. The motor stages are architected in a daisy chain assembly and addressed through a RS323 port by the second workstation. The confocal principle is implemented by synchronizing the camera rolling shutter to scanning the laser beam in the specimen chamber. To manage the performance of the microscope, a custom software is developed in the LabVIEW environment (LabVIEW 2012, National Instruments). Since the microscope should acquire data automatically with the least human interference, the rigorous performance of the software is the key priority. The software should deal with several data streams and electronic components while maintaining robustness, avoiding asynchrony and data loss. To this aim, the entire software is partitioned to smaller yet independent and self-contained modules based on an object-oriented programming platform such that each module manages a precisely defined task and handling the data stream required internally and/or externally (Figure 7.7). To process the tasks and manage such a data stream is computationally intensive and may result in system crash, timing delay and/or data loss. Therefore, it is required to distribute the software modules on several computers. To this aim, the Murmex software development kit [108] is used. Murmex creates distributed finite state machines based on an object-oriented programming platform using a messaging system that provides a reliable and asynchronous communication between software modules. Each Murmex-based module performs a state transition following the message it receives either from itself or other modules. Each software module is addressed by an ID and sends its current state to the observers that are specified in its configuration file according to a high-level observer/observe hierarchy. Such hierarchy aims at dividing a large software to smaller yet self-contained modules that are distributed on a messaging network. The software modules can be run synchronously with precise timing on different computers connected through internet or a local Ethernet connection. The hardware-related modules manage the performance of the according hardware components in the *in vivo* LSFM whereas the Waveform and Stack modules operate the entire system.

The Waveform is used as the master module when acquiring 2D time-lapse images. In start state, the Waveform sends a Start message to the Camera and AOTF which modulates the laser intensity and sets the trigger to infinite mode. The Camera module sends the frame rate, resolution and shutter time (rolling shutter pace) values via ”mapping script[2]” method back to the Waveform module. The Waveform generates a TTL pulse at the frame rate of the camera to trigger the acquisition of a frame. This signal serves as start/stop trigger for both camera and galvo to synchronizing the galvo with rolling shutter movement. Then the Waveform module generates a saw-tooth waveform such that its amplitude sets the light sheet height (see section 7.1) and its frequency is equivalent to the system frame rate[3]. Additionally, the camera readout is set to light sheet mode (the rolling shutter moves downward from the top of the sensor) therefore, the phase of the waveform is calculated such that the galvo start scanning the laser beam at its maximum angle corresponding to the top of the light sheet. The saw-tooth waveform is then sent to the galvo through an analog signal produced by the DAQ board. In this configuration the camera and the galvo are triggered to start/stop synchronously and the galvo moves step-by-step

---

[2] Mapping script is a messaging method in Murmex (Parent Class in the hierarchy) configuration file to update a value in module A to corresponding value in module B,

[3] A fraction of the camera frame rate is used to run the galvo and positioning unit to avoid the inertia of the galvo and positioning unit. This guaranties every cycle of the movement of galvo and z-axis motor stage fit within a frame acquisition time.

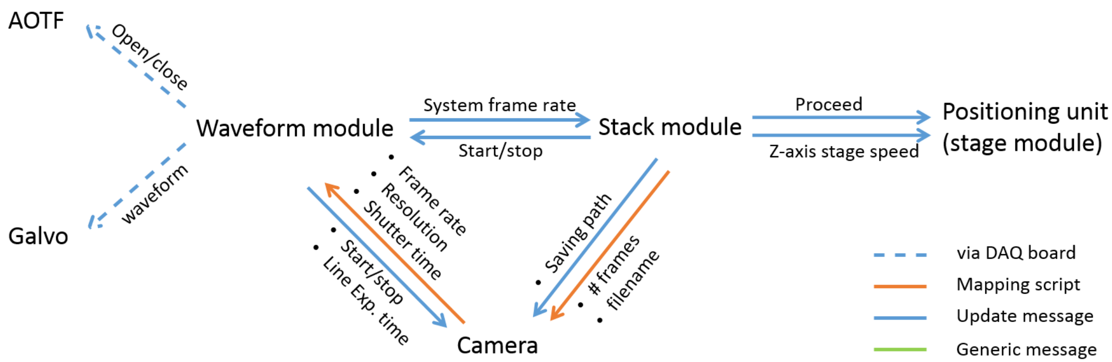

Figure 7.7: Schematic of the control software; The performance of the *in vivo* LSFM, is controlled by a LabVIEW-based custom software. The entire software is partitioned to smaller yet independent and self-contained modules. The modules are distributed over two workstation using the Murmex software developing kit such that each module manages a precisely defined task and handling the data stream required internally and/or externally.

with the rolling shutter.
The Stack module is used to acquire stacks of images along the detection axis (z). It sends the filename, number of the planes in the stack (#frames) and where to save them to the camera. Additionally, the Stack sends a Start message to the waveform to start the camera. The camera informs back the Waveform module about its setting. The Stack module receives the system frame rate via an update message form Waveform. The speed of the z-axis motor stage is then calculated such that the specimen moves continuously while the images are acquired. Each image stacks are written to the disk by the Camera module in a ".dcimg" file from Hamamatsu.

Chapter 8

in vivo LSFM; spatial resolution

The spatial resolution of the *in vivo* LSFM is evaluated by imaging sub-diffraction fluorescent beads embedded in 1.5% agarose for both Gaussian and Bessel illuminations. Stack images along z axis of identical samples are recorded and later analyzed using Fiji (Fiji Package, ImageJ) [109]. To determine the spatial resolution, six PSF from six different parts of the FOV are evaluated. The intensity profile of the PSFs across x and z axes are fitted to a Gaussian function gaining the radial and axial FWHM. The average of the evaluated FWHMs is shown in Figure 8.1. In case of Gaussian illumination, the radial and axial FWHM of the PSF are $0.5 \pm 0.08 \mu m$ (mean ± standard deviation) and $6.7 \pm 0.2 \mu m$, respectively (Figure 8.1A).

Radial FWHM is governed by the characteristic of the detection unit of *in vivo* LSFM, hence, remains the same for both Bessel and Gaussian illumination. Unlike the radial FWHM, the axial FWHM of the PSF depends on the characteristics of the illumination such that using Bessel illumina-

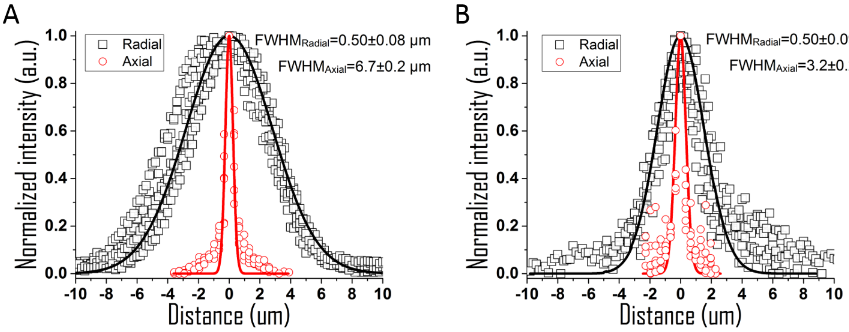

Figure 8.1: Experimental PSF; A) Gaussian illumination B) Bessel illumination The averaged axial FWHMs is shown in black solid line the raw data in black square where the averaged radial FHWMs is presented with red solid line and their according raw data with red circles. Using Bessel beam illumination shows about 2 times improvement in axial FWHM.

tion reduces the axial FWHM to $3.2 \pm 0.2\mu m$ (Figure 8.1B). The virtual slit width is set to $3\mu m$ for Bessel Illumination and $6.7\mu m$ when Gaussian illumination is implemented, unless mentioned otherwise (see section 7.4). Although the radial resolution of *in vivo* LSFM matches to the literature [110], it does exceed the diffraction-limited resolution. Since a water-dipping objective ($20x$, $1.0NA$, $WD2mm$, water immersion, Olympus) is used as the detection objective, the refractive index mismatch between the medium and the one that objective is designed for does not occur. The reason for such matter in radial resolution is because of the Nyquist sampling theorem (see section 2.3); at least four pixels area ($2x2$ pixels) is required to image the diffraction-limited Airy disk. The Nyquist theorem for *in vivo* LSFM, suggest a radial resolution of $0.65\mu m$that is two times the camera pixel pitch in the object space (subjected to undersampling) whereas the averaged experimental radial resolution (Figure 8.1) is by 8%

less. $FWHM_{radial}^{Gauss} = 0.50 \pm 0.08\mu m$ and $FWHM_{radial}^{Bessel} = 0.50 \pm 0.09\mu m$ (mean ± standard deviation), following the eq. 2.13 correspond to an averaged radial resolution of about $0.6 \pm 0.1\mu m$. Notably, the radial resolution does not differ in either Gaussian or Bessel illumination because, as expected from eq. 5.1, the radial resolution is only dependent on the detection objective and wavelength. Although this radial resolution is advantageous when detecting the soma, it may result in the loss of the information about very thin dendrites. Unlike the radial resolution, the axial resolution is governed by the characteristic of the illumination optics. The axial resolution of *in vivo* LSFM is governed by the thickness of the light sheet that is theoretically calculated to $6.7\mu m$ and $2.9\mu m$ (FWHM) for Gaussian and Bessel illumination respectively. Whereas the experimental values are average $FWHM_{axial}^{Bessel} = 6.7 \pm 0.2\mu m$ and $FWHM_{axial}^{Bessel} = 3.2 \pm 0.2\mu m$. Using the Bessel illumination improves the axial resolution and consequently, reduces the anisotropy in the spatial resolution, more than twice as the using Gaussian illumination. However, the experimental value for $FWHM_{axial}^{Bessel}$ depicts about 10% worse axial resolution than the expected theoretical value. One possible reason is that the laser energy is divided to all the concentric rings shaping J_0 Bessel beam and beam intensity is speared over a larger volume. The outer rings of the Bessel beam result in out-of-focus fluorescence and therefore alteration in contrast. The virtual confocal slit, in one hand filters out the out-of-focus fluorescence, on other hand it reduces the number of the photons reaching the detector and therefore, 5 times higher laser intensity is required for apparently similar signal-to-background in comparison with Gaussian light sheet illumination. Fahrbach et.al [111] found that to achieve similar signal-to-background for Bessel modality, the sample is exposed to six fold laser power . Hence, a virtual slit, slightly larger than the theoretical axial resolution of the Bessel *in vivo* LSFM has been used that can result in larger experimental $FWHM_{axial}^{Bessel}$ than expected by the theory.

Chapter 9

in vivo LSFM; high-fidelity Ca^{2+} imaging

The self-healing property of the Bessel beam promises a reduction in the shadowing artifact that is discussed in chapter 6. A time-lapse image series is recorded from a transversal plane deep in the brain on a $3dpf$ larval zebrafish $[elavl3 :: GCaMp6s]$ with Gaussian or Bessel illumination modalities. When using the Gaussian illumination, dark stripes appear parallel to the illumination axis. The dark stripes get thicker and in greater numbers on the right side (the light sheet propagates from left to right) of the brain that results in a reduction in image quality (Figure 9.1B).

In contrast, when illuminating the specimen with Bessel illumination, the dark stripes are almost eliminated and the details of the neurons clusters are revealed. In case of Bessel illumination modality, the specimen is illuminated with 3 times more laser power comparing to Gaussian one. Mapping the brain activity using GCaMPs is based on the fluorescence variation over time (see chapter 4). Therefore, any undesired variation in the intensity

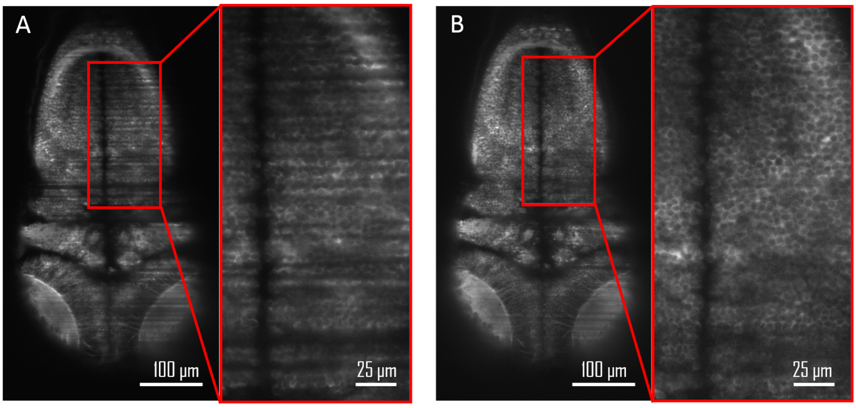

Figure 9.1: Shadowing reduction; An identical section of the brain imaged by *in vivo* LSFM using A) Gaussian light sheet and B) Bessel light sheet. Light sheet propagates from left to right. The red arrows indicate exemplary shadows.

can lead to misinterpretation of the nervous activity. When Gaussian light sheet is applied, the shadow that is caused by obstacles results in dark stripe (Figure 9.1).

In the same manner, a blood cell floating in a vessel in the brain scatters the incident light and induces a dynamic shadow. Figure 9.2A shows three images from a section of the midbrain in right hemisphere of $4dpf$ larval zebrafish $[elavl3 :: GCaMp6s]$ with one second intervals where a blood cell (red arrowhead) floating in a vessel produces a corresponding shadow along the Gaussian light sheet (propagation axis; left to right). The fluorescence intensity along an identical line (yellow line) is measured and normalized for qualitative comparison that is shown in Figure 9.2B. In ”0s”, the blood cell shadow is below of the yellow line. The intensity at ”0s” reaches to a peak at the center whereas after ”1s” the blood cell shadow sweeps the yellow

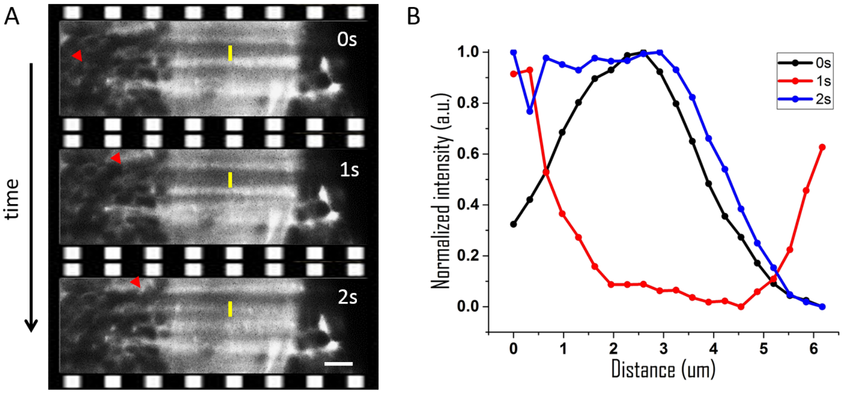

Figure 9.2: Intensity variation in fluorescence signal caused by a blood cell; A) three frames with 1 second interval of a time-lapse showing the right midbrain of a larval zebrafish [$elavl3 :: GCaMp6s$] in which a blood cell floating in a vessel is pointed with red arrowhead. Light sheet propagates from left to right. Scale bar is $5\mu m$. B) the intensity profile over an identical line is shown with in yellow on the frames in A.

line and results in a sharp decrease in the intensity profile. At ”2s” the blood cell shadow is sweeping above the yellow line where an intensity peak appears again in the middle of the line intensity profile. Living zebrafish continuously pumps the blood through whole body including the brain. The blood stream causes dynamic shadowing artifacts which can be thought as a protracted flickering in the acquired time-lapse images.

To quantitatively compare the performance of Bessel and Gaussian illumination modalities, larval fishes expressing nuclei-restricted $GCaMP6s$ in almost all neurons $[elavl3 :: H2B :: GCaMp6s]$ are studied. Each experiment consists of time-lapses acquired from an identical single transversal plane that are successively imaged in both Gaussian and Bessel light sheet modalities. In following, identical individual cells in both Bessel and Gauss time-lapses are manually inspected and categorized to active and inactive cell. The fluorescent image of an identical lateral plane deep in the brain of a $4dpf$ larval zebrafish is shown in Figure 9.3A (Gaussian modality) and Figure 9.3B (Bessel modality).

Identical cells ($n = 171$) that are manually inspected to be inactive over the acquisition time paired in both Gaussian and Bessel illumination modalities are studied. Their corresponding fluorescence trace (intensity profiles over time) is calculated over a circular ROI around the cell nucleus using ImageJ. After subtracting the background, the baseline of each trace is calculated and corrected with the MATLAB ”mjbackadj” function. The fluorescence traces are presented as normalized deviation of the raw data (F) from the calculated baseline ($F0$), $dF/F = (F - F_0)/F_0$. The traces of three inactive cells shown in Figure 9.3C using red (cyan) for Gaussian (Bessel) illumination. These exemplary traces indicate the drastic reductions of the flickering when imaging with Bessel illumination. The standard deviation of each trace over time is evaluated as a quantitative measure for the level

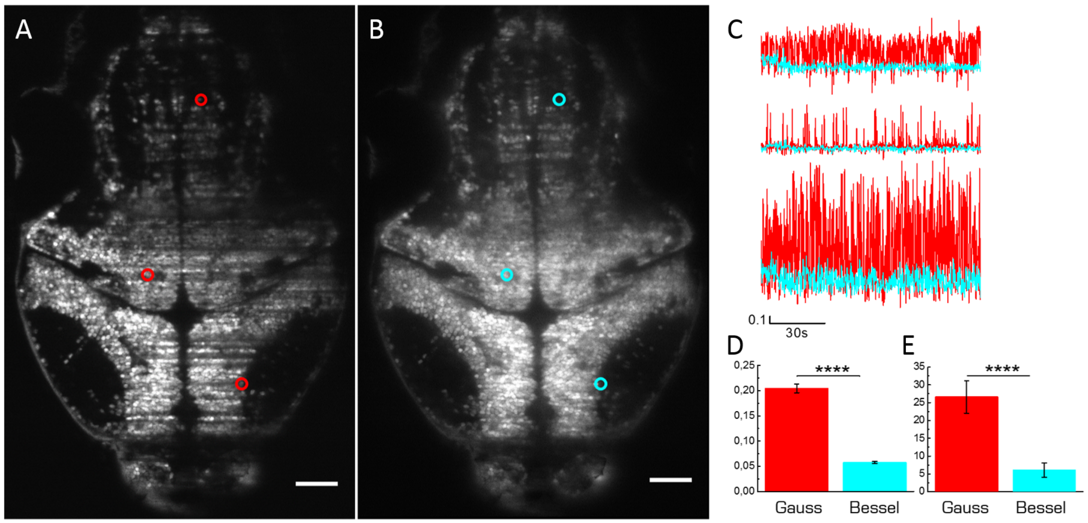

Figure 9.3: Comparison of using Gaussian and Bessel illumination modality in inactive cells; An identical single plane in the brain of a $4dpf$ larval zebrafish $[elavl3 :: H2B :: GCaMP6s]$ is imaged with A) Gaussian illumination and B) Bessel illumination. Light sheet propagates from left to right. Scale bar is $50\mu m$. C) Fluorescence traces of three exemplary cells identified in both excitation modalities using red (cyan) for Gaussian (Bessel) illumination (Scale bars are 10% of dF/F in x and $30s$ in y). D) Mean of the standard deviation of the traces for the Gaussian and Bessel beam illumination of pairwise identical cells (paired t-test, $n = 171$), error bars indicate the standard error of the mean or SEM. E) Mean of area affected by blood cells inducing flickering as a percentage of the total brain area for Gaussian and Bessel illumination.

of the flickering. The mean of the standard deviation of the paired inactive cell traces show a reduction in the case of Bessel by the factor of 4 (Figure 9.3D).

Furthermore, the area of the brain affected by blood cells causing flickering is shown as a percentage of the whole brain area in the FOV in Figure 9.3E that reports less area is affected by a factor of four while using Bessel illumination modality. The area affected due to flickering is calculated by using a custom-written macro in Fiji such that the standard deviation of 5 sequential images of a time-lapse is calculated in 5-frame steps. The calculated standard deviation images result in a temporally downsampled standard deviation time-lapse.

The bright regions in the standard deviation time-lapses correspond to the more intense variation in the pixels' gray value, hence they are estimated as the regions affected by flickering. In case of an active cell, time-lapses are acquired from a lateral plane of $4dpf$ larval zebrafishes $[elavl3 :: H2B :: GCaMP6s]$ using Bessel illumination modality (Figure 9.4A). The traces are measured over circular ROIs around the cell nuclei in optic tectum, hindbrain and hindbrain oscillator. A custom-written MATLAB code slightly smoothens the traces and then counts the peaks above a predefined threshold and furthermore, rejects the peaks have prominence smaller than 0.08. The threshold is calculated as the mean value plus one deviation of the traces acquired with Gaussian (Bessel) modality to be 0.4366(0.1248) according to the fluorescence traces of the inactive cells presented in Figure 9.3. The exemplary processed traces are shown in the boxes that are color-coded to the ROIs in the brain sections. The peaks that are detected above the Gaussian (Bessel) threshold are denoted with red (cyan) arrowheads. More exemplary traces containing the peaks above Gaussian threshold are assorted in the red box regardless that the traces

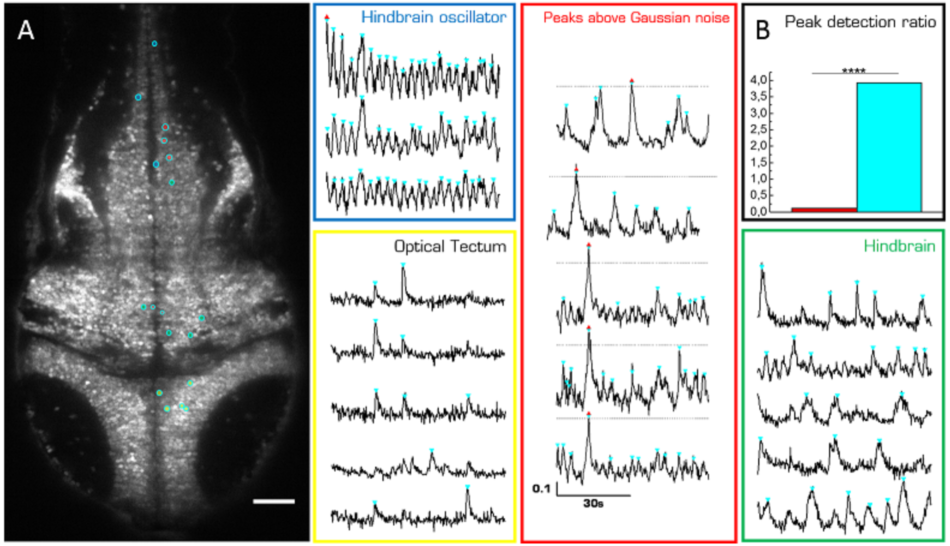

Figure 9.4: Comparison of using Gaussian and Bessel illumination modality in active cells; A) Fluorescent image from a single plane in the brain of a $4dpf$ larval zebrafish [$elavl3$ :: $H2B$ :: $GCaMP6s$]. Scale bar is $50\mu m$. The ROIs are color-coded to the boxes when the exemplary neuronal activity traces are presented. (Scale bars are 10% of dF/F in x and $30s$ in y). The peaks that are detected above the Gaussian and Bessel thresholds (equal to 0.4366 and 0.12479) are denoted with red and cyan arrowheads, respectively. B) The mean number of the peaks detected above the Gaussian and Bessel thresholds per trace are shown in red and cyan successively. The comparison demonstrates above 35-fold improvement in the detecting the neural activities that are manually inspected when using the Bessel illumination modality. The SEM bar are too small to be displayed.

are acquired from which section of the brain. Figure 9.4B presents the mean number of the peaks detected above the Gaussian (Bessel) thresholds ($n = 53$) to be 0.11 (3.92) peaks per trace which show a 35-fold improvement in the number of the activity peaks that are correctly detected when using the Bessel illumination modality.

Chapter 10

Summary

in vivo LSFM is a one-sided illumination DSLM system with interchangeable Gaussian and Bessel illumination modalities to obtain high-fidelity Ca^{2+} imaging.

Ahrens et.al.[110] applied both time-dependent and time-independent thresholds to extract the activity peaks from florescence traces with respect to the manual inspection. The fluorescent images were acquired by a two-sided DSLM using Gaussian illumination. They reported that using thresholds to subtract unwanted fluorescence variation results in detecting false activities in the fluorescence traces when no actual activity inspected manually. As shown in Figure 9.3C, when using Gaussian illumination, several spikes are appeared whereas the cell is manually inspected to be inactive. These spikes are mainly caused by the floating blood cells producing dynamic shadows that appear as moving dark stripes. Such dynamic shadow causes a time-dependent variation on a pixel value and therefore appears as a flickering artifact that can be misinterpreted to Ca^{2+} signal(s). Thanks to the non-diffractive and self-reconstructive properties of Bessel beams, the flickering artifacts drastically reduced by a factor of 4 (Figure 9.3D). The advantage of using Bessel light sheet in case of detecting the neural activities from the fluorescence trance with respected to the manual inspection is shown in Figure 9.4. The brain functional activities that are observed manually, can be detected with 35 times higher fidelity in the fluorescence traces acquired with Bessel illumination modality. Whereas, most of the activity peaks are superimposed (covered) with high level of flickering when using Gaussian illumination modality and therefore are not resolved.

Part III

Generation of transgenic zebrafish with broadly neuronal channelrhodopsin expression

Chapter 11

Introduction

The method to optically manipulate a cell or a population of genetically engineered cells expressing light-activated channels or pumps is known as optogenetics. A popular class of these channels are channelrhodopsins (ChRs). In 2002, Nagel determined ion-flux properties of Channelrhodopsin-1 or ChR1 [112]. Once the ChRs are illuminated at their activation wavelength, they open and therefore elicit influx to the intracellular fluid. If enough numbers of ChRs open, the depolarization overcomes the membrane threshold potential and, hence, the action potential occurs (Figure 11.1).

A list of published ChRs with their activation peaks and references is shown in table 11.1. Through genetic targeting, it is possible to express optogenetic tools in specific populations of cells and to extract information about them deep in the brain, their functional activities and interconnections. Part III describes the generation of a transgenic zebrafish expressing C1V1 (Chlamydomonas ChR1 fused to volvox ChR1). This engineered rhodopsin is excited at red-shifted wavelengths (if using single-photon excitation) with high efficiency and in a short response time [113]. The aim is to investigate

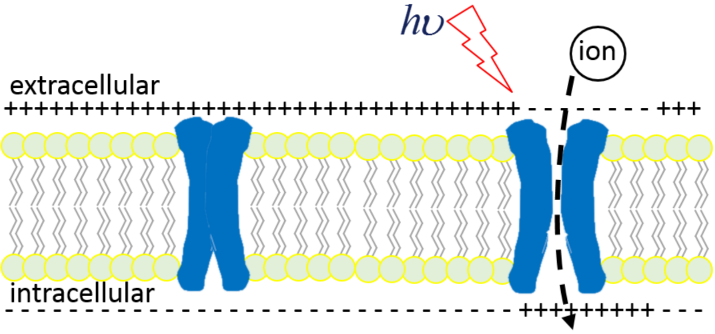

Figure 11.1: Schematic configuration of light-activated channels; The light-activated channels are closed. Once the light-activated channels are illuminated at their activation wavelength, they open and therefore elicit the ion influx to the intracellular fluid.

the neuronal activity in larval zebrafish by the mean of studying the Ca^{2+} propagation across the brain in response to an optical stimulation. Therefore, a zebrafish transgenic line that expresses both ChRs and GCaMPs is required. The process of generating such transgenic line is initiated by generating a stable transgenic zebrafish line expressing ChRs. It will be followed, then, by crossing this zebrafish with currently available zebrafish expressing pan-neuronal $GCaMP6s$ $[elavl3 :: GCaMp6s]$.

One of the common light-activated channels is ChR2 that already has been used in activity and behavioral studies in animal models [115]. ChR2 is activated at $480nm$ that makes it inappropriate in combination with Ca^{2+} imaging using a GCaMP because of the excitation spectral overlap. Therefore, C1V1, a red-shifted ChR, is more suited to generate transgenic zebrafish for truly independent excitation of GCaMP6s and C1V1. This allows simultaneous optical manipulation and neural activity recording.

Table 11.1: Channelrhodopsins with peak activation wavelength and references. Adopted from [114]

Opsin	**Mechanism**	**Peak Activation λ**	**References**
ChR2	Cation channel	470 nm	Boyden et al.,2005 and Nagel et al.,2003
ChR2(H134R)	Cation channel	470 nm	Nagel et al.,2005 and Gradinaru et al.,2007
ChR2 (T159C)	Cation channel	470 nm	Berndt et al.,2011
ChR2 (L132C)	Cation channel	474 nm	Kleinlogel et al.,2011
VChR1	Cation channel	545 nm	Zhang et al.,2008
C1V1	Cation channel	540 nm	Yizhar et al.,2011a
C1V1 ChETA (E162T)	Cation channel	530 nm	Yizhar et al.,2011a
C1V1 ChETA(E122T/E162T)	Cation channel	535 nm	Yizhar et al.,2011a

Chapter 12

Plasmid cloning

The aim of this step is to insert the C1V1 gene behind the elavl3 promoter into a plasmid containing Tol2 sites. The Tol2 system is a transposition system facilitates gene integration into the zebrafish genome with high efficiency [116]. The elavl3 promoter includes a RNA-binding protein specific to neurons that starts the transcription of C1V1 in almost all neurons across the zebrafish body [52, 117]. The $[Tol2 :: elavl3 :: H2B :: GCaMP6s]$ plasmid was gifted by Ahrens's lab [118] and is ordered from a repository (Addgene plasmid #59530). Furthermore, to obtain C1V1 gene,$pAAV :: CaMKIIa :: C1V1(t/t) :: TS :: mCherry$ (Addgene plasmid #35500) which was gifted by Deisseroth's lab, is ordered from the same repository [119]. Two pairs of primers for PCR amplification are designed to produce $Tol2 :: elavl3$ (Figure 12.1A) and C1V1 $(t/t) :: TS :: mCherry$ (Figure 12.1B) sequences from their according plasmids (Phusion Hot Start II High-Fidelity DNA Polymerase, Thermo Scientific). The primers are designed such that $Tol2 :: elavl3$ and C1V1 $(t/t) :: TS :: mCherry$ have at least 15 nucleotides base pair (bp) overlap on each side to be compatible

with an high-efficiency and directional cloning approach (In-Fusion®HD Cloning Kit, Clontech Laboratories).
5’-ggatcctggccgtcGTT-3’
(forward primer)
and
5’-taattatctgcaggtggAAAATATAACAGG-3’
(reverse primer).
The primers for PCR amplification of C1V1(t/t) :: TS :: $mCherry$ are in particular long sequences because the overlapped nucleotides regions are artificially added to the sequences of the actual amplification primers:
5’-ccacctgcagataattaTTGTCGCGGAGGCCATGG-3’
(forward primer)
and
5’-gacggccaggatccTTTACTTGTACAGCTCGTCCATGC-3’
(reverse primer)
that the overlapped coding sequences are in lower case and colored accordingly. The PCR amplicons quality is tested with gel electrophoresis (O’GeneRuler 1 kb Plus DNA Ladder, ready-to-use, Thermo Scientific). This step is followed by cloning C1V1 (t/t)::TS::mCherry to Tol2::elavl3 using one-reaction HD Cloning reaction (Figure 12.1C). It is notable that the PCR amplicon Tol2::elavl3 from Tol2::elavl3::H2B::GCaMP6s contains *Ampicillin* resistance gene (Amp R). The produced plasmid is then transferred into bacteria cells and cultured on agar plates containing *Ampicillin*. Therefore, only the bacteria that are transformed by the plasmid containing Amp R grow. The cultured plasmid, then, is extracted from the bacteria and purified (QIAprepÂ® Spin Miniprep, QIAGEN).
The production of the plasmid is followed by testing the DNA construct sequence with both enzymatic digestion and sequencing. $Tol2$ :: $elavl3$ and

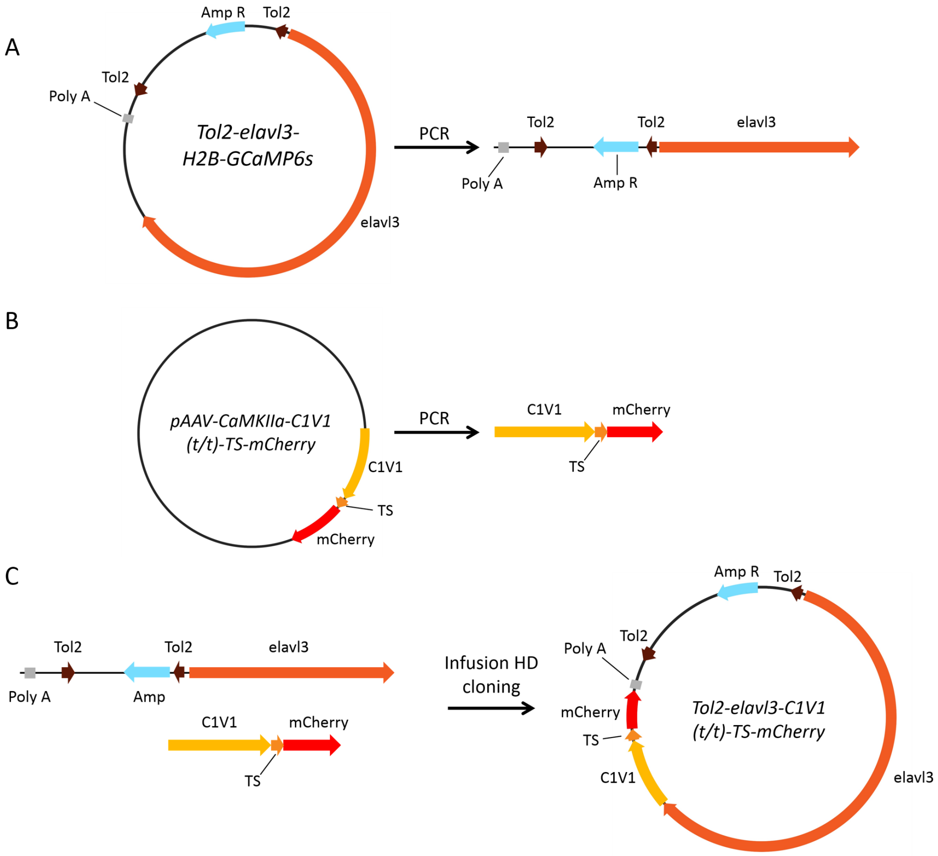

Figure 12.1: Molecular cloning; A and B denote PCR amplification of $Tol2 :: elavl3$ and $C1V1(t/t) :: TS :: mCherry$ fragments with primers containing at least 15 bp overlap compatible with infusion HD cloning (In-Fusion®HD Cloning Kit, Clontech Laboratories) that is presented in C.

C1V1 $(t/t) :: TS :: mCherry$ DNA fragments are expected together to have two NotI and one XhoI restriction sites (Figure 12.2A). If the cloning product is $Tol2 :: elavl3 :: C1V1(t/t) :: TS :: mCherry$, it can be enzymatically

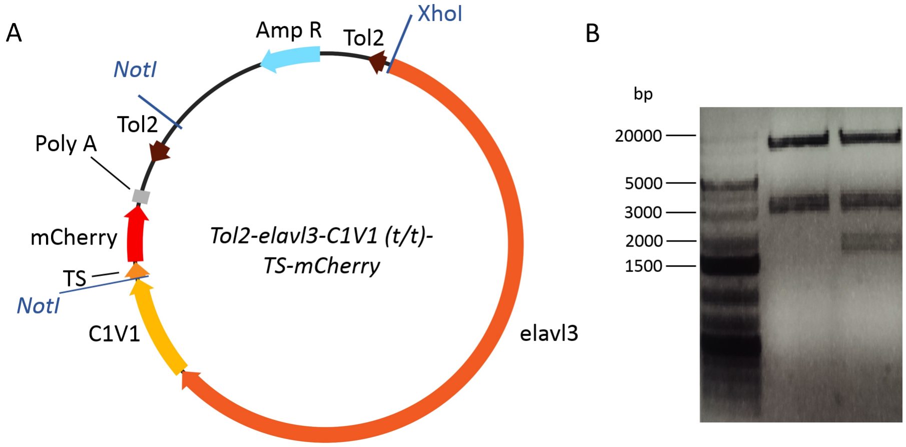

Figure 12.2: Double digestion with NotI and XhoI enzymes; A) The position of two NotI and one XhoI restriction sites in the $Tol2 :: elavl3 :: C1V1(t/t) :: TS :: mCherry$. B) Gel electrophoresis of a digested plasmid containing NotI-NotI, XhoI- NotI and NotI-XhoI ending fragment (right) comparing with one that does not contain NotI-NotI ending fragment (middle) with respect to a DNA ladder (GeneRuler 1 kb DNA Ladder, ready-to-use, Thermo Scientific)

digested (DoubleDigest Calculator, Thermo Scientific) to three fragments with 9747 bp (ends: XhoI- NotI), 2954 bp (ends: NotI-XhoI) and 1637 bp (ends: NotI-NotI) length. The XhoI restriction site is just behind the elavl3 promoter gene while one NotI site is placed between C1V1 and mCherry genes and the other one is after a Tol2 site (Figure 12.2A).

The product of the double digestion is then tested with gel electrophoresis on 1% agarose (Agarose High resolution, Carl Roth) gel in 1X Triethylamine (Triethylamine (TEA), $\geq$ 99.5% for synthesis, Carl Roth) and resulted in three DNA fragments with expected lengths (Figure 12.2B) with respect to a DNA ladder (GeneRuler 1 kb DNA Ladder, ready-to-use, Thermo

Scientific). The double digestion by NotI and XhoI enzymes resulted in a good indication that $C1V1(t/t) :: TS :: mCherry$ is cloned to $Tol2 :: elavl3$.

Furthermore, forward and reverse sequencing primers (Figure 12.3A) are designed to adequately prove that the produced DNA plasmid is the expected Tol2::elavl3::C1V1 (t/t)::TS::mCherry:
5'-ATCACTCGGACCAGTTCTCG-3'
(forward sequencing primer)
is used for sequencing inside C1V1 gene upstream to elavl3 sequence and
5'-AAGGGCGAGGAGGATAACAT-3'
(reverse sequencing primer)
for sequencing mCherry gene downstream to Tol2 site. The result of sequencing shows 100% matching in C1V1, mCherry, elavl3 and Tol2 sequences but one thymine (T) on each side that are highlighted in yellow (Figure 12.3B). The proven DNA vector is then ready for injection in the fertilized zebrafish embryos to generate a transgenic line with nearly pan-neuronal $C1V1(t/t) :: mCherry$ expression.

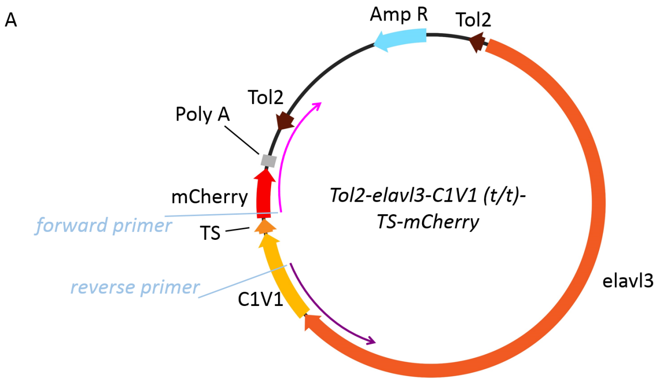

B

>C1V1 sequence downstream to elavl3

```
CGCTCGTGGGCACGGTGGAAAACGTAGTCGGGGCCATCCTGAGTCGCGACCGGCACCGTCGCG
TCACTGCCAGTCGAGGCTCCTGCGCTGCCGGCCGCCAGCGCCACTGCCAGCGCTAGGGCAAGA
AGCCATGGCCTCCGCGACATTAATTATCTGCAGGTGGAAAATATAACAGGTTGGGTGAGGAAC
CATAATTTGAGGGGTGTAATGCTTGGCATTCTCGCTGAGAGGTTAAAAATCAATGCGTCTGAG
AGGGATAGGGCCTGAGGAGGACAATATCCCACCCTTCCTCCTCCTCTGACCTCCCTCACTTCA
```

>mCherry upstream to Tol2

```
CGTGCAGCTGCCCGGCGCCTACAACGTCAACATCAAGTTGGACATCACCTCCCACAACGAGGA
CTACACCATCGTGGAACAGTACGAACGCGCCGAGGGCCGCCACTCCACCGGCGGCATGGACGA
GCTGTACAAGTAATGGATCCTGGCCGTCGTTTTACTGTACCATCGATGATGATCCAGACATGA
TAAGATACATTGATGAGTTTGGACAAACCACAACTAGAATGCAGTGAAAAAAATGCTTTATTT
GTGAAATTTGTGATGCTATTGCTTTATTTGTAACCATTATAAGCTGCAATAAACAAGTTAACA
```

Figure 12.3: Sequencing; A) A pair of primers are designed to sequence the cloned gene upstream to Tol2 site (forward primer) and downstream to elavl3 (reverse primer). B) The sequencing result confirms that elavl3, C1V1 and mCherry genetic codes are correctly cloned into Tol2-donor plasmid. Two thymines (T) are the only mismatches that are outside the genetic codes, therefore, they do not cause mistranscription of the genes. The sequences in (B) are colored according to (A)

Chapter 13

Microinjection and screening

The next step in generating a transgenic zebrafish line is to integrate the cloned DNA (elavl3::C1V1(t/t)::TS::mCherry) to the zebrafish genome and then transfer it to the F1 offspring (first generation) through germ lineage. That can be done by injecting the DNA plasmid into a fertilized egg at one-cell stage (zygote). The efficiency of the germline transmission efficiency in this method is about 5% [120]. Another method is injecting a pseudotyped retrovirus into the embryos at blastula stage. The retrovirus back transcripts its own RNA and the cloned one inside the host cells to produce its complementary DNA (cDNA). The cDNA is then integrated into the host cell genome where it is termed provirus. The germline transmission efficiency with this method is about 100% [116]. However, applying this approach is difficult because of the delicacy and adversity in handling and modifying the retrovirus. To overcome these restrictions, a Tol2-based method has been introduced. A DNA plasmid containing two Tol2 transposons and a synthetic RNA are co-injected into the zygote. In the embryos, the RNA is translated to Tol2 transposase protein. The transposase protein catalyzes the excision of the Tol2-donor construct and the integration of elavl3::C1V1(t/t)::TS::mCherry into the genome. This method leads to about 50% efficiency in producing F1 transgenic offspring [116].

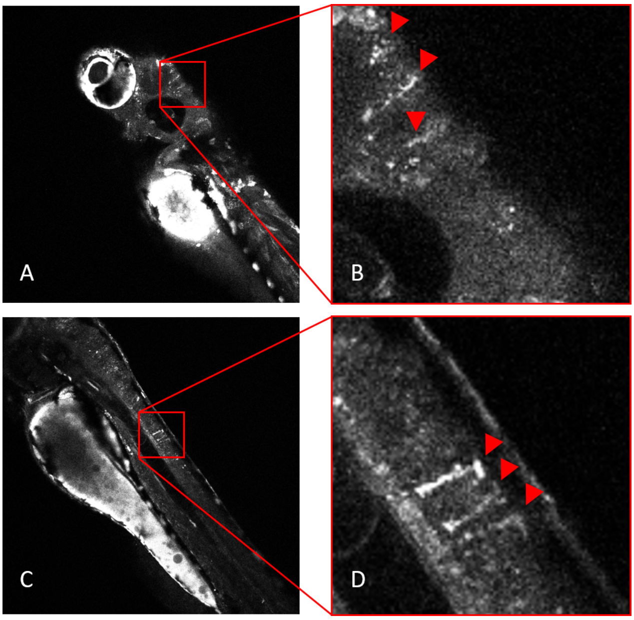

Figure 13.1: Screening the marker (mCherry) expression inside brain and spinal cord in an injected fish; A) Confocal image from midbrain. B) Zoom-in image from A; the read arrowheads point the mCherry fluorescence signals. C) Confocal image from spinal cord. D) Zoom-in image from C; the red arrowheads point the motor neurons expressing mCherry.

For this purpose, $12.5ng/\mu L$ of $Tol2 :: elavl3 :: C1V1(t/t) :: TS :: mCherry$ have co-injected with $12.5ng/\mu L$ of synthetized transposase RNA in a zygote following the protocol by Clarck and his colleagues [121]. The resulting embryos have screened with a confocal microscope (Figure 13.1). Since mCherry gene is fused downward C1V1 gene as a marker in the cloned

DNA, the mCherry fluorescence is a good indication to the C1V1 expression. Fluorescent images recorded from mCherry fluorescence shows mosaic mCherry expression in the midbrain (Figure 13.1A and red arrow heads in Figure 13.1B) and over the spinal cord where motor neurons axons project, e.g. to the muscles (Figure 13.1C and red arrow heads in Figure 13.1D). A reliable confirmation on $elavl3 :: C1V1(t/t) :: TS :: mCherry$ integration in the zebrafish genome requires genotyping. The genotyping is done by anesthetizing the larval fish on ice and then putting the larvae in 50 µL of $50mMNaOH$ (Sodium hydroxide solution, 1 mol/l, Carl Roth). This step is followed by incubating the sample at $95 \circ C$ for 20 minutes. After the sample is cooled down to $4 \circ C$ (5 minutes incubating on ice), $5\mu L$ of $1M$ Tris-Cl, $pH8$ (TRIS hydrochloride, Carl Roth) is added to the sample and mixed gently. At last, the sample is centrifuged at $1300rpm$ for 5 minutes to pellet the debris.

The supernatant containing genomic DNA is used as the template for PCR test (the genomic DNA is stored at $4\circ$ before freezing at $-20 \circ C$). To this end, one reverse primer;

5’-TTGACCTCAGCGTCGTAGTG-3’

(reverse primer)

is designed which is placed by the end of mCherry gene. The reverse primer with two forward primers;

5’-CATGGCTTCTTGCCCTAGC-3’

(forward primer 1)

and

5’-TTCGTCCTCCCTTTGTCATC-3’

(forward primer 2)

are designed (Figure 13.2A) to amplify a 1633 bp PCR fragment within C1V1(t/t)::TS::mCherry (light green interval in Figure 13.2A) and a 1941

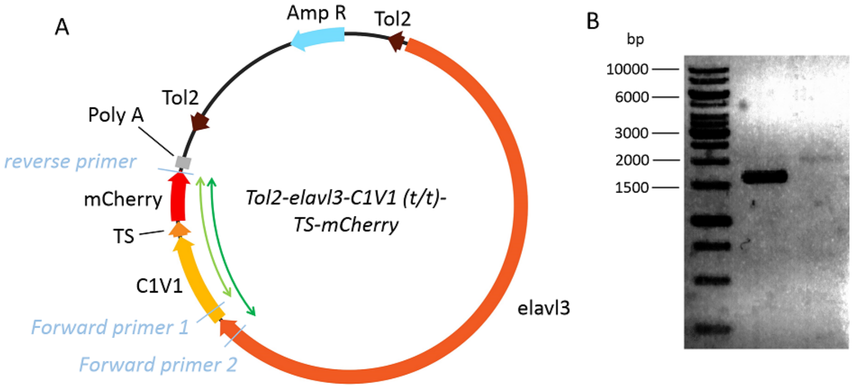

Figure 13.2: Genotyping; A) A reverse PCR primer is designed along with two forward PCR primers to amplify a 1633 bp fragment within C1V1::TS::mCherry cassette (light green interval) and a 1941 bp fragment inside elavl3 promoter downstream to mCherry gene (dark green interval). B) Gel electrophoresis of 1941 bp (right) and 1633 bp PCR amplicons with respect to a DNA ladder (GeneRuler 1 kb DNA Ladder, ready-to-use, Thermo Scientific). The contrast of the image in B is enhanced for better visualization.

bp PCR fragment within elavl3::C1V1(t/t)::TS::mCherry (dark green interval in Figure 13.2A), respectively. The PCR products are then verified by gel electrophoresis. This records the correct PCR fragments are produced (Figure 13.2B).

Chapter 14

Summary

In Summary, we construct a new Tol2-based DNA vector to generate a transgenic zebrafish line expressing a red-shifted ChR, C1V1 fused with a fluorescent marker, mCherry in almost all neurons under the elavl3 promoter that makes almost whole nervous system of a larval zebrafish accessible for optical manipulation.

The successful molecular cloning was tested with double digestion method. The approved produced plasmid was then sequenced (Figure 12.3A) within the amino acid gene (C1V1(t/t)::mCherry) reverse to the elavl3 promoter and forward the Tol2 site. Figure 12.3B denotes the sequencing results that confirm the C1V1 sequence which is fused to mCherry gene is cloned downstream elavl3 promoter sequence. The confirmed DNA plasmid was then injected into zebrafish zygotes and screened for mCherry fluorescence (Figure 13.1). Since mCherry gene is fused to C1V1 gene, the detection of red fluorescence from mCherry was inspected as the indication for C1V1 expression on the neurons membrane. The C1V1 expression confirmation was then followed by genotyping approach in which the genomic DNA of the larval zebrafish was extracted and then used as a template for a PCR amplification (Figure 13.2A). The gel electrophoresis images confirm the correct length of DNA fragments that are amplified using the designed PCR primer pairs as presented in Figure 13.2B. The positive fishes will be outcrossed with the wild -types to generate a stable transgenic zebrafish line, $[elavl3 :: C1V1(t/t) :: TS :: mCherry]$.

Part IV

Conclusion and outlook

Chapter 15

Conclusion

We have successfully built the *in vivo* LSFM that is a one-sided illumination DSLM system with interchangeable Gaussian and Bessel illumination modalities. The Bessel illumination modality reveals a 2-fold improvement in the spatial resolution in detection direction (Figure 8.1)that is an essential requirement if aiming to investigate the correlation between the structure and function of the nervous system. DSLM systems with interchangeable Gaussian and Bessel illumination modalities have been presented by Olarte et. al. [106] and Fahrbach et. al. [122] to acquire high-quality images respectively using living ”Caenorhabditis elegans” and highly scattering samples. Nevertheless, they have not investigated the performance of the Bessel light sheet in neuronal activity imaging. Moreover, they have discussed that the out-of-focus fluorescence arisen from the outer rings of the Bessel beams degrades the image quality and a filtering method is required, therefore, the *in vivo* LSFM is equipped with virtual confocal slit (section 7.4) thanks to a robust and precise synchronization of the camera rolling shutter and the galvo scanning steps by our custom control software (section 7.5). When using Bessel light sheet, the artifacts in the images caused by scattering are drastically reduced (Figure 9.1) such that Rohrbach [123] theoretically predicted for using scanned Bessel beam in imaging a cluster of scattering spheres. This reduction is the result of the Bessel beams both self-healing characteristics and the higher effective NA (larger focusing angle) of the illumination objective in comparison with the Gaussian illumination. As discussed in section 7.1, the $1/e^2$ beam diameter of the Gaussian beam entering the back aperture of the illumination objective is $2.45mm$ whereas the external diameter of the ring (Fourier transform of a J_0 Bessel beam) entering the illumination objective is $10.5mm$ that results in $NA_{Bessel} \approx 4.3NA_{Gauss}$ [1]. Furthermore, we studied the effect of the shadowing artifacts on neural activity imaging. Figure 9.2 shows the variation of the fluorescent intensity caused by a blood cell floating in a vessel in the right midbrain of a zebrafish when using Gaussian illumination modality. Since recording the brain activity using changes of Ca^{2+} concentration is based on the fluorescence variation arisen from the $GCaMP6s$ genetically encoded in the zebrafish neurons, any artifact causing fluorescence intensity variation or flickering artifact results in the false detection of the activity signals or a superimposition of the flickering and the actual activity signals (Figure9.3). Ahrens et. al. [110] demonstrated the fastest DSLM-based method to map whole brain activity (1.3 second per entire brain volume) with cellular resolution using $5dpf$ larval albino zebrafish expressing $GCaMP5G$ in almost all neurons $[elavl3 :: GCaMP5G]$. They implemented two-side illumination DLSM to improve the spatial resolution. Furthermore, they set thresholds to extract the activity signals but

---

[1] The effective numerical aperture of an objective is governed by $NA = nD/2f$, where n, f and D denote the medium refractive index, the objective focal distance and the beam diameter entering the objective, respectively

they have not investigated the Bessel light sheet performance. In particular, we demonstrated that using Bessel light sheet drastically reduces false activity detection caused by scattering obstacle (e.g. blood cells) via reducing the flickering artifact that allows to extract the correct neural activity signals with high fidelity (Figure 9.4). Investigating the function of the brain requires not only a high fidelity activity recording method but also a well-defined and non-invasive method to interact simultaneously with the living specimen that leads toward closing the feedback loop between the environmental cues, locomotion sensory information transmission and processing.

The studies presented experimental approaches to cross-register the larval zebrafish sensory-motion activity with brain functional activity patterns either in specific subset of neurons or whole brain. Of note, odor tracking [124], visual [125]and sound stimuli [126] have been investigated on different animal models that provide invaluable information about correlation between the behavioral activity and the brain functional activity in specific neuronal circuits. Recently, the whole-brain activity mapping on either fictively-behaving [52, 127] or freely swimming [128] larval zebrafish provide promising results toward closing the aforementioned feedback loop. However, the latter approaches use electrophysiological methods that are mainly invasive that induce undesired stimuli (e.g. pain) yet are difficult to perform. Alternatively, optical targeting of neuronal circuits with genetically encoded ChRs enables optical manipulation of a specific neuron and/or subset of neurons revealing their functionality, for instance, evoking motor responses by optically stimulated spinal neurons [129]. To this aim, Shipley et.al. [130] reported an interesting approach to optically manipulate targeted subset of neurons expressing ChR2 and simultaneously record the activity of neurons that only express GCAMP3 in freely moving ”Caenorhabditis elegans”. However, their system is not able to simultaneously manipulate and record the neurons that express both ChR2 and GCAMP3 because their fluorescence excitation overlap. Therefore, we have generated a transgenic zebrafish expressing a red-shifted ChR. Part III demonstrates the successful establishment of a transgenic zebrafish expressing a red-shifted ChR, C1V1 under elavl3 promoter that could make almost entire nervous system of a larval zebrafish accessible for optical manipulation. To the best of our knowledge, this is the first demonstration of a transgenic zebrafish for optogenetics manipulation using C1V1 under elavl3 promoter.

Chapter 16

Outlook

Chapter 7 describes the *in vivo* LSFM in details that it is followed by the characterization of the system. Bessel illumination *in vivo* LSFM provides a high-fidelity activity imaging thanks to the self-healing property of the Bessel beams as well as a reduction of factor of two in spatial resolution anisotropy. It has been outlined that by even one-side illumination LSFM, we detected high-throughput neuronal activity signals deep inside the brain of the larval zebrafish. However, the aim has been to interact with the specimen while recording its neural activity. To achieve simultaneous neuronal optogenetic manipulation and activity recording, a specimen is required that co-expresses ChR and GECI with well separated excitation spectra. Rickgauer et.al. [131] generated transgenic mice co-expressing C1V1 and GCaMP3 in a subset of the neurons. They demonstrated simultaneous optogenetic manipulation and Ca^{2+} imaging deep in the brain of a living mouse with cellular resolution. However, the entire nervous system of a mouse is not accessible even when utilizing infrared lasers for the excitation. We can overcome this limitation by using larval zebrafish. To this aim we generated a novel transgenic zebrafish with almost pan-neuronal C1V1 expression. (see part III)

The zebrafish expressing C1V1, [elavl3::C1V1(t/t)::TS::mCherry] can be crossed with transgenic zebrafish expressing GCaMP6s, [elavl3::H2B::GCaMP6s] to generate a transgenic zebrafish co-expressing C1V1 and GCaMP6s in almost all neurons. C1V1 is a ChR that opens when exposed to red-shifted wavelengths yet it is highly sensitive and it may be activated in lower wavelengths in a certain level.

This can cause a spectral overlap between Ca^{2+} imaging using GCaMPs and optical manipulation via C1V1 activation. Hence, obtaining a truly independent yet simultaneous manipulation and recording of neuronal activity, two-photon excitation is required. Rickgauer et.al. [131] also reported a laser scanning two-photon system for simultaneous optical manipulation and activity imaging using an infrared laser with $920nm$ ($1064nm$) wavelength for Ca^{2+} imaging (C1V1 activation). Since, the application of two-photon excitation in optogenetics, several scanning methods such as spiral trajectory and line scanning approaches has been performed that suffer from low both temporal resolution and spatial flexibility (see chapter 2.5).

Parallel illumination [132] approaches such as intensity modulation utilizing the LED arrays (patterned illumination) or digital micrometer devices overcome the temporal resolution issue but for highly flexible and reconfigurable two-photon excitation at high speeds, phase modulation with a spatial light modulator (SLM) is required [133] (see appendix A).

To this aim, a spatial light modulator two-photon (SLM 2P) system is assembled on a 2^{nd} optical table above the *in vivo* LSFM (Figure 16.1). An infrared pulsed laser beam (FemtoPower, 1064 nm, $> 5W$, Fianium, NKT Photonics) is expanded with a telescope ($f1 = 75mmandf2 = 250mm$) onto

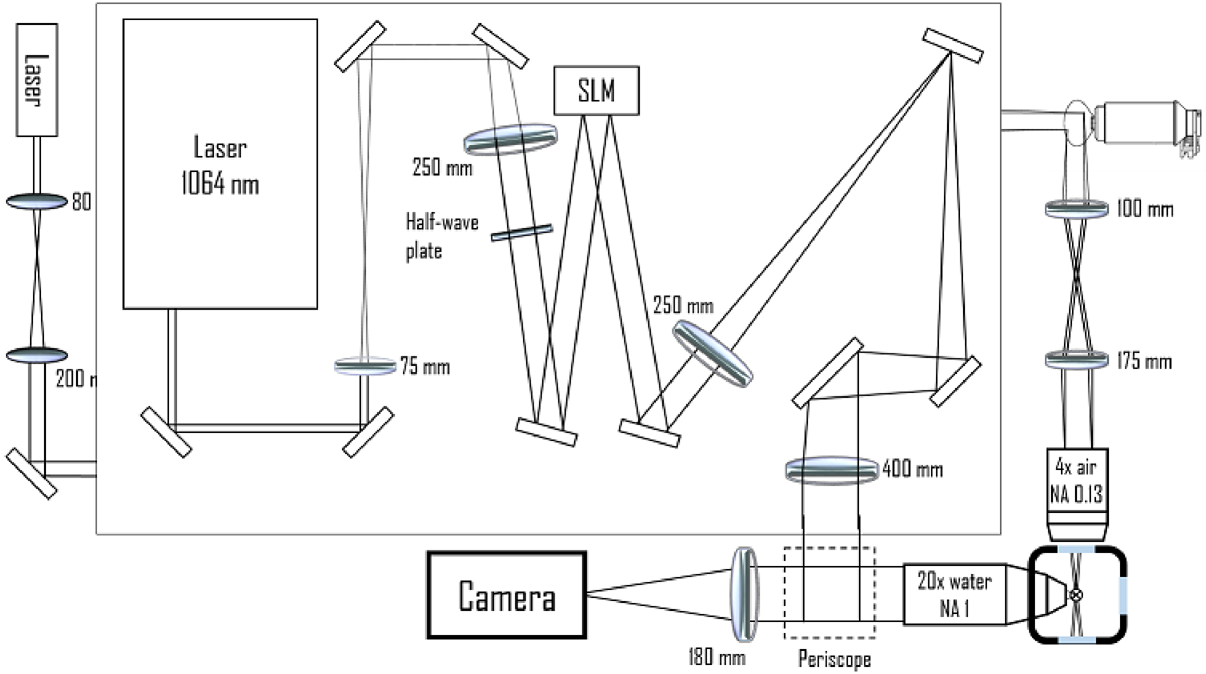

Figure 16.1: Spatial light modulator two photon (SLM 2P) system top view; Schematic representation of the light path. An infrared laser beam (FemtoPower, 1064nm, $> 5W$, Fianium, NKT Photonics) is expanded with a telescope ($f1 = 75mmandf2 = 250mm$) on a SLM active window. The half-wave plate adjusted the polarization direction of the laser beam to maximize the reflection from the SLM. The $1/e^2$ diameter of the entrance beam is adjusted by a telescope to just under-fill the detection objective back aperture

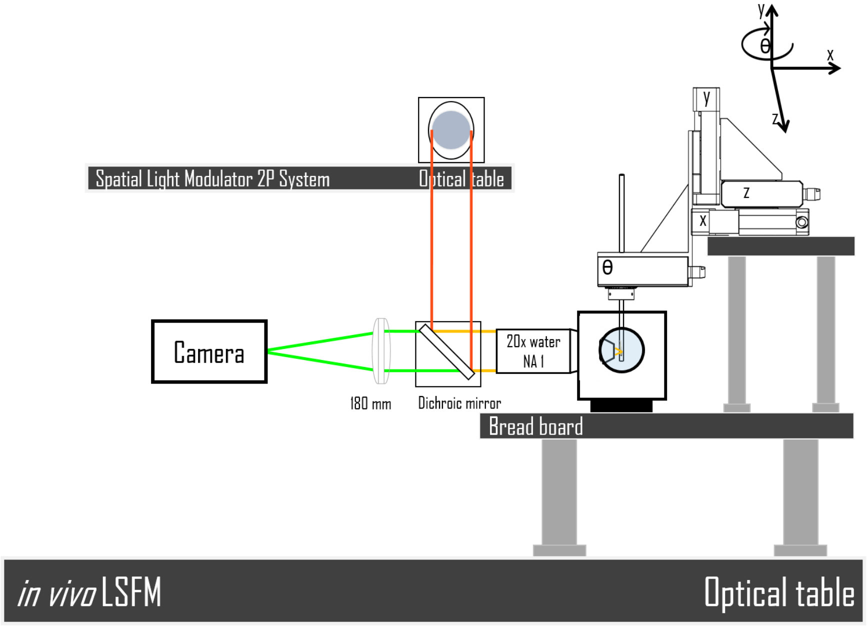

Figure 16.2: Schematic of the superposed SLM 2P system excitation and *in vivo* LSFM detection path; The laser beam from the SLM 2P system is reflected to the back aperture of the objective by a dichroic mirror. The objective simultaneously collects the green fluorescence from the specimen. The dichroic mirror is transparent to the visible wavelengths; hence the collected fluorescence produces the image on the camera by a lens ($f = 180mm$)

the chip of a liquid crystal SLM ($X10468-3$, LCOS-SLM, Hamamatsu) active window. The half-wave plate adjusted the polarization direction of the laser beam to maximize the reflection from the SLM. The $1/e^2$ diameter of the entrance beam is adjusted by the 2^{nd} telescope ($f1 = 250mm$ and $f2 = 400mm$) to just under-fill the objective back aperture. The laser beam is then reflected onto the back aperture of the *in vivo* LSFM detection objective by a periscope (Figure 16.2). The periscope is assembled in a cage system ($30mm$ cage system with a dichroic cage cube, Thorlabs) such that the laser beam is reflected downward onto a dichroic mirror (Shortpass Dichroic Mirror, $805nm$ Cutoff, Thorlabs). Likewise, the *in vivo* LSFM will be further improved by using an infrared pulsed laser for Ca^{2+} imaging to obtain well separation in the excitation wavelengths of C1V1 and GCaMP6s.

Considering the high temporal resolution and flexibility achieved from SLM 2P system superposed to a two photon Bessel illumination *in vivo* LSFM as well as the promising benefits in using zebrafish expressing GCaMP6s and C1V1 in almost all neurons as the animal model, simultaneous yet independent optical manipulation and activity recording of whole nervous system could be obtained.

Part V

Appendix

Appendix A

Fluorescence light-sheet microscopy techniques

Table A.1: Light-sheet microscopy techniques. Adopted from [88]

Technique	**Unique features**	**Pros**	**Cons**	**Ideal application**	**Reference**
Orthogonal-plane fluorescence optical sectioning (OPFOS)	Single-sided light-sheet illumination	Optical sectioning	Shadows, stripes	Fluorescently-stained samples	Voie et al., 1993
Selective plane illumination microscopy (SPIM)	Single-sided light-sheet illumination, sample rotation about vertical axis	Fast acquisition, low photbleaching, good penetration, MVR	Shadows, stripes	Extended time-lapse imaging of millimetre-sized embryos, high speed movies	Huisken et al., 2004
Objective coupled planar illumination (OCPI) microscopy	Single-sided light-sheet illumination, attached to detection lens	Fast stack acquisition, no sample movement, conventional sample	Shadows, stripes	Conventionally prepared samples, fast 3D imaging	Holekamp et al., 2008
Ultra-microscopy	Dual-sided light-sheet illumination, upright detection path	Sealed chamber with clearing solution	No index-matched optics, stripes	Large fixed and cleared specimens	Dodt et al., 2007
Digital scanned laser lightsheet fluorescence microscopy (DSLM)	Like SPIM, light-sheet generated by beam scanning	Like SPIM, uniform, adjustable light-sheet	Like SPIM	Like SPIM	Keller et al., 2008
Multidirectional SPIM (mSPIM)	Like SPIM, pivoting light-sheet, two alternating illumination arms	Like SPIM, reduced stripes, reduced shading	Space constraints	Like SPIM, especially scattering and absorbing tissue	Huisken and Stainier, 2007
Highly inclined and laminated optical sheet (HILO) microscopy	Single lens for oblique light-sheet illumination and detection	Single lens	Very narrow FOV	Single cell microscopy close to the coverslip	Tokunaga et al., 2008
Oblique plane microscopy (OPM)}	Like HILO, matching, tilted image plane	Like HILO, extended FOV	Extensive optics	Like HILO	Dunsby, 2008

Appendix B

Liquid crystal spatial light modulator

Spatial light modulator (SLM) refers to a device that modulates the spatial properties of light such as amplitude and phase. As discussed in chapter 16, to achieve a simultaneous optical manipulation with activity recording, parallel two-photon excitation method that is re-configurable with a high temporal resolution is required. LCOS-SLM by Hamamatsu (Figure B.1) is a SLM that modulates only the phase of the incident light in the reflective mode using a nematic liquid crystal (LC)[1] that are oriented in a parallel manner. The information of the modulation is addressed to a CMOS-based chip via a Digital Visual Interface (DVI) controlled by a PC. The pixe-

---

[1] Liquid crystals are elongated ellipsoid-shape molecules with anisotropic dielectric properties such that their electric permittivity (ϵ) is directional. For a liquid crystal with positive uniaxial symmetry,ϵ is larger when the electric field is parallel to molecule direction (long axis). According to the position and orientation order of the molecules, the LCs are categorized in three types. Nematic liquid crystals are one of three types of liquid crystals such that the molecules are oriented in a same direction while their position is random. [27]

lated CMOS chip induces an according electric field to the liquid crystal molecules and hence changes their orientation order pixel-by-pixel such that each pixel locally alters the optical path and modulates the phase of the reflected light. Hereby, the wavefront of the reflected light is encoded to the modulation information addressed by the PC. Oron et.al. [134] reviewed that there are two main techniques to address a modulation intensity to a SLM; digital holography (DH) and generalized phase contrast (GFC). Although, with GPC method, low-speckle excitation is achievable and a simplified control software is required, the DH require a simpler optical setup and most importantly it is the only available method providing 3D pattern parallel excitation.

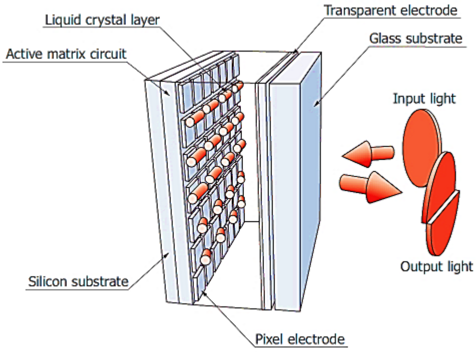

Figure B.1: Schematic of a LCOS-SLM X10468 from Hamamatsu; This model is an only phase modulator that works in the reflective mode using a parallel-aligned nematic LC on a pixelated electrode (CMOS-based chip). The modulation pattern is addressed to the electrode via DVI interface by a PC. The pixelated electrode induces an according electric field that changes the orientation liquid crystal molecules locally. Thereby, the wavefront of the reflected light is encoded pixel-by-pixel to the modulation pattern addressed by the PC. Adopted from [135]

Appendix C

Acknowledgement

I would like to thank Erasmus Mundus Doctorate Program, Europhotonics (Grant No. 159224-1-2009-1-FR-ERA MUNDUS-EMJD) for providing such an intercultural PhD program.

I also would like to thank my supervisors Prof. Francesco S. Pavone (LENS, University of Florence) to give me this opportunity to develop the *in vivo* LSFM in his group and Prof. Martin Bastmeyer (ZNBIO, Karlsruhe Institute of Technology) to provide all the requirements for me to learn and practice molecular biology for establishment of the transgenic zebrafish.

I learned a lot from Marcel van 't Hoff in Optics and LabVIEW. I am thankful for all the time we have been spending together.

To Caroline Müllenbroich who took over the *in vivo* LSFM project and provided according information for this dissertation when I was busy pursuing the establishment of the stable transgenic zebrafish line at ZNBIO.

To Francesco Vanzi and Lapo Torini for providing zebrafish larvae used in calcium imaging.

Special thanks to Joachim Bentrop, Michaela Schober and Ramona Dries

for their dedication in teaching and helping me through all steps. You have been always patient and supportive, although there was a physicist in the biology lab. What on earth!!!
It was not possible to finish this work without your friendship and help in the office, the lab, the coffee breaks, the moments in ”Mensa” and/or the amazing evenings: Marco, Martino, Lucia, Alessia, Antonino, Niccolò, Matteo, Marios, Claudia, Felix, Mona and the others that surely I have forgotten.
To my old friends Amin, Babak and Behnam who have been always available and supportive although there are thousands of kilometers distance between us.
Showing me the kindness, welcoming and the contradictions in the Italian culture and providing her special relaxing explanations for the confusing situations, thank you Ivana.
Last but not least, a deep sense of gratitude to my family who has been supporting me to follow my dreams by sacrificing theirs. I owe them what I have achieved.

Bibliography

[1] George Gabriel Stokes. On the change of refrangibility of light. *Philosophical Transactions of the Royal Society of London*, 142:463–562, 1852. 3

[2] Markus Sauer, Johan Hofkens, and Jörg Enderlein. Basic principles of fluorescence spectroscopy. *Handbook of Fluorescence Spectroscopy and Imaging: From Single Molecules to Ensembles*, pages 1–30, 2011. 3

[3] S Gasiorowicz. *Quantum Physics*. Jonh Wiley and Sons, 2003. 4

[4] Thomas G. Chasteen. Jablonski diagram. 5

[5] C Cohen-Tannoudji, B Diu, and F Laloë. *Quantum Mechanics*. Wiley-Interscience, 2006. 4

[6] GA Ketsle, LV Levshin, and VV Bryukhanov. Mechanism of the external heavy atom effect on intersystem crossing in rhodamine dye solutions. *Journal of Applied Spectroscopy*, 24(5):573–577, 1976. 5

[7] GJ Hoijtink. The influence of paramagnetic molecules on singlet-triplet transitions. *Molecular Physics*, 3(1):67–70, 1960. 5

[8] Michael J Davies. Reactive species formed on proteins exposed to singlet oxygen. *Photochemical & Photobiological Sciences*, 3(1):17–25, 2004. 5

[9] Daniel C Harris and Michael D Bertolucci. *Symmetry and spectroscopy: an introduction to vibrational and electronic spectroscopy*. Courier Corporation, 1978. 6

[10] J.R. Lakowicz. *Principles of fluorescence spectroscopy*. Principles of Fluorescence Spectroscopy. Springer, 2006. 6

[11] Dmitriy M Chudakov, Mikhail V Matz, Sergey Lukyanov, and Konstantin A Lukyanov. Fluorescent proteins and their applications in imaging living cells and tissues. *Physiological reviews*, 90(3):1103–1163, 2010. 7

[12] Hiroshi Morise, Osamu Shimomura, Frank H Johnson, and John Winant. Intermolecular energy transfer in the bioluminescent system of aequorea. *Biochemistry*, 13(12):2656–2662, 1974. 7

[13] Douglas C Prasher, Virginia K Eckenrode, William W Ward, Frank G Prendergast, and Milton J Cormier. Primary structure of the aequorea victoria green-fluorescent protein. *Gene*, 111(2):229–233, 1992. 7

[14] M Chalfie, Y Tu, G Euskirchen, WW Ward, and DC Prasher. Green fluorescent protein as a marker for gene expression. *Science*, 263 (5148):802–805, 1994. 7

[15] Richard N Day and Michael W Davidson. The fluorescent protein palette: tools for cellular imaging. *Chemical Society Reviews*, 38(10): 2887–2921, 2009. 7

[16] Nathan C Shaner, George H Patterson, and Michael W Davidson. Advances in fluorescent protein technology. *Journal of cell science*, 120(24):4247–4260, 2007. 8

[17] Isadore Berlman. *Handbook of florescence spectra of aromatic molecules*. Elsevier, 2012. 8, 9

[18] GG Guilbault. Practical fluorescence (modern monographs in analytical chemistry). *Marcel Dekker Inc, New York*, 1990. 9

[19] Robert E Campbell, Oded Tour, Amy E Palmer, Paul A Steinbach, Geoffrey S Baird, David A Zacharias, and Roger Y Tsien. A monomeric red fluorescent protein. *Proceedings of the National Academy of Sciences*, 99(12):7877–7882, 2002. 9

[20] Nathan C Shaner, Robert E Campbell, Paul A Steinbach, Ben NG Giepmans, Amy E Palmer, and Roger Y Tsien. Improved monomeric red, orange and yellow fluorescent proteins derived from discosoma sp. red fluorescent protein. *Nature biotechnology*, 22(12):1567–1572, 2004. 9

[21] FS Pavone, PTC So, and PMW French. *Microscopy Applied to Biophotonics*, volume 181. IOS Press, 2014. 11

[22] J. W. Lichtman and J. A. Conchello. Fluorescence microscopy. *Nat Methods*, 2(12):910–9, 2005. 11

[23] Joseph W Goodman. *Introduction to Fourier optics*. Roberts and Company Publishers, 2005. 13, 56

[24] Max Born and Emil Wolf. *Principles of optics: electromagnetic theory of propagation, interference and diffraction of light.* CUP Archive, 2000. 15

[25] Douglas B Murphy and Michael W Davidson. Fundamentals of light microscopy. *Fundamentals of Light Microscopy and Electronic Imaging, Second Edition*, pages 1–19, 2013. 18

[26] George B Arfken and Hans J Weber. *Mathematical methods for physicists international student edition.* Academic press, 2005. 19

[27] Bahaa EA Saleh and Teich. Fundamentals of photonics. *Wiley Series in Pure and Applied Optics, Wiley*, 10, 2007. 19, 55, 129

[28] José-Angel Conchello and Jeff W Lichtman. Optical sectioning microscopy. *Nature methods*, 2(12):920–931, 2005. 20

[29] J.B. Pawley. *Handbook of biological confocal microscopy. Language of science.* Number v. 1 in Handbook of biological confocal microscopy. Language of science. Springer, 2006. 21, 23

[30] Rainer Heintzmann. Band-limit and appropriate sampling in microscopy. *Cell Biology: A Laboratory Handbook*, 3:29–36, 2006. 22, 24

[31] Rafael C Gonzalez and Richard E Woods. *Digital image processing.* Pearson, 3rd edition, 2007. 23

[32] Steven W Smith. *The scientist and engineer's guide to digital signal processing.* California Technical Pub. San Diego, 3rd edition, 1999. 25

[33] Albert Rose. Television pickup tubes and the problem of vision. *Advances in Electronics and electron Physics*, 1:131–166, 1948. 25

[34] James R Janesick. *Scientific charge-coupled devices*, volume 117. SPIE press Bellingham, Washington, 2001. 26

[35] Winfried Denk, James H Strickler, Watt W Webb, et al. Two-photon laser scanning fluorescence microscopy. *Science*, 248(4951):73–76, 1990. 29

[36] Alberto Diaspro, editor. *Confocal and Two-Photon Microscopy: Foundations, Applications and Advances.* Wiley, 3rd edition, 2001. 29

[37] Alessandro Esposito, Federico Federici, Cesare Usai, Fabio Cannone, Giuseppe Chirico, Maddalena Collini, and Alberto Diaspro. Notes on theory and experimental conditions behind two-photon excitation microscopy. *Microscopy research and technique*, 63(1):12–17, 2004. 30

[38] Gaddum Duemani Reddy, Keith Kelleher, Rudy Fink, and Peter Saggau. Three-dimensional random access multiphoton microscopy for functional imaging of neuronal activity. *Nature neuroscience*, 11(6): 713–720, 2008. 30

[39] QT Nguyen, N Callamaras, C Hsieh, and I Parker. Construction of a two-photon microscope for video-rate ca^{2+} imaging. *Cell calcium*, 30(6):383–393, 2001. 31

[40] Fritjof Helmchen and Winfried Denk. Deep tissue two-photon microscopy. *Nature methods*, 2(12):932–940, 2005. 32

[41] Warren R Zipfel, Rebecca M Williams, and Watt W Webb. Nonlinear magic: multiphoton microscopy in the biosciences. *Nature biotechnology*, 21(11):1369–1377, 2003. 32

[42] George Streisinger, Charline Walker, Nancy Dower, Donna Knauber, and Fred Singer. Production of clones of homozygous diploid zebra fish (brachydanio rerio). *Nature*, 291(5813):293, 1981. 33

[43] Rémy Beaudouin, Benoit Goussen, Benjamin Piccini, Starrlight Augustine, James Devillers, François Brion, and Alexandre RR Péry. An individual-based model of zebrafish population dynamics accounting for energy dynamics. *PloS one*, 10(5):e0125841, 2015. 33

[44] Joseph R Fetcho, Shin-ichi Higashijima, and David L McLean. Zebrafish and motor control over the last decade. *Brain research reviews*, 57(1):86–93, 2008. 33

[45] Shin-ichi Higashijima, Mark A Masino, Gail Mandel, and Joseph R Fetcho. Imaging neuronal activity during zebrafish behavior with a genetically encoded calcium indicator. *Journal of neurophysiology*, 90 (6):3986–3997, 2003. 33

[46] Ruben Portugues, Kristen E Severi, Claire Wyart, and Misha B Ahrens. Optogenetics in a transparent animal: circuit function in the larval zebrafish. *Current opinion in neurobiology*, 23(1):119–126, 2013. 33

[47] Owen Randlett, Caroline L Wee, Eva A Naumann, Onyeka Nnaemeka, David Schoppik, James E Fitzgerald, Ruben Portugues, Alix MB Lacoste, Clemens Riegler, Florian Engert, et al. Whole-

brain activity mapping onto a zebrafish brain atlas. *Nature methods*, 12(11):1039–1046, 2015. 33

[48] Mario F Wulliman, Barbara Rupp, and Heinrich Reichert. *Neuroanatomy of the zebrafish brain: a topological atlas*. Birkhäuser, 2012. 33

[49] Christiane Nusslein-Volhard and Ralf Dahm. *Zebrafish*. Oxford University Press, 2002. 34, 35

[50] Jeroen Bakkers. Zebrafish as a model to study cardiac development and human cardiac disease. *Cardiovascular research*, 91(2):279–288, 2011. 34

[51] Jiandong Liu and Didier YR Stainier. Zebrafish in the study of early cardiac development. *Circulation research*, 110(6):870–874, 2012. 34

[52] Nikita Vladimirov, Yu Mu, Takashi Kawashima, Davis V Bennett, Chao-Tsung Yang, Loren L Looger, Philipp J Keller, Jeremy Freeman, and Misha B Ahrens. Light-sheet functional imaging in fictively behaving zebrafish. *Nature methods*, 2014. 34, 51, 101, 117

[53] Jun Li, Julia A Mack, Marcel Souren, Emre Yaksi, Shin-ichi Higashijima, Marina Mione, Joseph R Fetcho, and Rainer W Friedrich. Early development of functional spatial maps in the zebrafish olfactory bulb. *The Journal of neuroscience*, 25(24):5784–5795, 2005. 34

[54] Jessell T.M. Kandel E.R., Schwartz J.H. *Principles of neural science*. Number 4th ed in Principles of neural science 4th ed. McGraw-Hill, 2000. 41

[55] Loren L Looger and Oliver Griesbeck. Genetically encoded neural activity indicators. *Current opinion in neurobiology*, 22(1):18–23, 2012. 41, 43

[56] Massimo Scanziani and Michael Häusser. Electrophysiology in the age of light. *Nature*, 461(7266):930–939, 2009. 42

[57] Christine Grienberger and Arthur Konnerth. Imaging calcium in neurons. *Neuron*, 73(5):862–885, 2012. 42, 43

[58] Robert S Zucker. Calcium- and activity-dependent synaptic plasticity. *Current Opinion in Neurobiology*, 9(3):305 – 313, 1999. 42

[59] Paul L Greer and Michael E Greenberg. From synapse to nucleus: calcium-dependent gene transcription in the control of synapse development and function. *Neuron*, 59(6):846–860, 2008. 42

[60] Michael J Berridge, Peter Lipp, and Martin D Bootman. The versatility and universality of calcium signalling. *Nature reviews Molecular cell biology*, 1(1):11–21, 2000. 42

[61] Diana Smetters, Ania Majewska, and Rafael Yuste. Detecting action potentials in neuronal populations with calcium imaging. *Methods*, 18(2):215–221, 1999. 42

[62] Bu-Qing Mao, Farid Hamzei-Sichani, Dmitriy Aronov, Robert C Froemke, and Rafael Yuste. Dynamics of spontaneous activity in neocortical slices. *Neuron*, 32(5):883–898, 2001. 42

[63] Christoph Stosiek, Olga Garaschuk, Knut Holthoff, and Arthur Konnerth. In vivo two-photon calcium imaging of neuronal networks.

Proceedings of the National Academy of Sciences, 100(12):7319–7324, 2003. 42

[64] Benjamin F Grewe, Dominik Langer, Hansjörg Kasper, Björn M Kampa, and Fritjof Helmchen. High-speed in vivo calcium imaging reveals neuronal network activity with near-millisecond precision. *Nature methods*, 7(5):399–405, 2010. 42

[65] JE Brown, LB Cohen, P De Weer, LH Pinto, WN Ross, and BM Salzberg. Rapid changes in intracellular free calcium concentration. detection by metallochromic indicator dyes in squid giant axon. *Biophysical journal*, 15(11):1155, 1975. 42

[66] RY Tsien, T Pozzan, and TJ Rink. Calcium homeostasis in intact lymphocytes: cytoplasmic free calcium monitored with a new, intracellularly trapped fluorescent indicator. *The Journal of Cell Biology*, 94(2):325–334, 1982. 42

[67] Roger Y Tsien. New calcium indicators and buffers with high selectivity against magnesium and protons: design, synthesis, and properties of prototype structures. *Biochemistry*, 19(11):2396–2404, 1980. 42

[68] Roger Y Tsien. A non-disruptive technique for loading calcium buffers and indicators into cells. 1981. 42

[69] Roger Y Tsien, Tullio Pozzan, and Timothy J Rink. T-cell mitogens cause early changes in cytoplasmic free ca2+ and membrane potential in lymphocytes. *Nature*, 295(5844):68–71, 1982. 42

[70] Grzegorz Grynkiewicz, Martin Poenie, and Roger Y Tsien. A new generation of ca2+ indicators with greatly improved fluorescence

properties. *Journal of Biological Chemistry*, 260(6):3440–3450, 1985. 42

[71] R Madelaine Paredes, Julie C Etzler, Lora Talley Watts, Wei Zheng, and James D Lechleiter. Chemical calcium indicators. *Methods*, 46 (3):143–151, 2008. 42

[72] Atsushi Miyawaki, Juan Llopis, Roger Heim, J Michael McCaffery, Joseph A Adams, Mitsuhiko Ikura, and Roger Y Tsien. Fluorescent indicators for ca2+ based on green fluorescent proteins and calmodulin. *Nature*, 388(6645):882–887, 1997. 42

[73] Jasper Akerboom, Jonathan D Vélez Rivera, María M Rodríguez Guilbe, Elisa C Alfaro Malavé, Hector H Hernandez, Lin Tian, S Andrew Hires, Jonathan S Marvin, Loren L Looger, and Eric R Schreiter. Crystal structures of the gcamp calcium sensor reveal the mechanism of fluorescence signal change and aid rational design. *Journal of biological chemistry*, 284(10):6455–6464, 2009. 43, 44

[74] Junichi Nakai, Masamichi Ohkura, and Keiji Imoto. A high signal-to-noise ca2+ probe composed of a single green fluorescent protein. *Nature biotechnology*, 19(2):137–141, 2001. 44

[75] Qi Wang, Bo Shui, Michael I Kotlikoff, and Holger Sondermann. Structural basis for calcium sensing by gcamp2. *Structure*, 16(12): 1817–1827, 2008. 44

[76] Joseph R Fetcho and Donald M O'Malley. Imaging neuronal networks in behaving animals. *Current opinion in neurobiology*, 7(6):832–838, 1997. 44

[77] Shin-ichi Higashijima, Hitoshi Okamoto, Naoto Ueno, Yoshiki Hotta, and Goro Eguchi. High-frequency generation of transgenic zebrafish which reliably express gfp in whole muscles or the whole body by using promoters of zebrafish origin. *Developmental biology*, 192(2): 289–299, 1997. 44

[78] Koichi Kawakami, Hisashi Takeda, Noriko Kawakami, Makoto Kobayashi, Naoto Matsuda, and Masayoshi Mishina. A transposon-mediated gene trap approach identifies developmentally regulated genes in zebrafish. *Developmental cell*, 7(1):133–144, 2004. 44

[79] Misha B Ahrens, Jennifer M Li, Michael B Orger, Drew N Robson, Alexander F Schier, Florian Engert, and Ruben Portugues. Brain-wide neuronal dynamics during motor adaptation in zebrafish. *Nature*, 485(7399):471–477, 2012. 44

[80] Adam M Packer, Lloyd E Russell, Henry WP Dalgleish, and Michael Häusser. Simultaneous all-optical manipulation and recording of neural circuit activity with cellular resolution in vivo. *Nature Methods*, 12(2):140–146, 2015. 44

[81] Adam M Packer, Botond Roska, and Michael Häusser. Targeting neurons and photons for optogenetics. *Nature neuroscience*, 16(7): 805–815, 2013. 44

[82] Henry Siedentopf and Richard Zsigmondy. Uber sichtbarmachung und größenbestimmung ultramikoskopischer teilchen, mit besonderer anwendung auf goldrubingläser. *Annalen der Physik*, 315(1):1–39, 1902. 47

[83] AH Voie, DH Burns, and FA Spelman. Orthogonal-plane fluorescence optical sectioning: Three-dimensional imaging of macroscopic biological specimens. *Journal of microscopy*, 170(3):229–236, 1993. 47

[84] Jan Huisken, Jim Swoger, Filippo Del Bene, Joachim Wittbrodt, and Ernst HK Stelzer. Optical sectioning deep inside live embryos by selective plane illumination microscopy. *Science*, 305(5686):1007–1009, 2004. 47

[85] Jan Huisken and Didier YR Stainier. Even fluorescence excitation by multidirectional selective plane illumination microscopy (mspim). *Optics letters*, 32(17):2608–2610, 2007. 47, 54

[86] Peter J Verveer, Jim Swoger, Francesco Pampaloni, Klaus Greger, Marco Marcello, and Ernst HK Stelzer. High-resolution three-dimensional imaging of large specimens with light sheet–based microscopy. *Nature methods*, 4(4):311–313, 2007. 47, 54

[87] Philipp J Keller, Annette D Schmidt, Joachim Wittbrodt, and Ernst HK Stelzer. Reconstruction of zebrafish early embryonic development by scanned light sheet microscopy. *science*, 322(5904):1065–1069, 2008. 47, 50, 51

[88] Jan Huisken and Didier YR Stainier. Selective plane illumination microscopy techniques in developmental biology. *Development*, 136(12):1963–1975, 2009. 48, 49, 51, 128

[89] Philipp J Keller, Annette D Schmidt, Anthony Santella, Khaled Khairy, Zhirong Bao, Joachim Wittbrodt, and Ernst HK Stelzer. Fast, high-contrast imaging of animal development with scanned light

sheet-based structured-illumination microscopy. *Nature methods*, 7 (8):637–642, 2010. 50, 51

[90] Jim Swoger, Peter Verveer, Klaus Greger, Jan Huisken, and Ernst HK Stelzer. Multi-view image fusion improves resolution in three-dimensional microscopy. *Optics express*, 15(13):8029–8042, 2007. 54

[91] L Silvestri, A Bria, L Sacconi, G Iannello, and FS Pavone. Confocal light sheet microscopy: micron-scale neuroanatomy of the entire mouse brain. *Optics express*, 20(18):20582–20598, 2012. 54

[92] Eugen Baumgart and Ulrich Kubitscheck. Scanned light sheet microscopy with confocal slit detection. *Optics express*, 20(19):21805–21814, 2012. 54, 74

[93] Jonathan Palero, Susana ICO Santos, David Artigas, and Pablo Loza-Alvarez. A simple scanless two-photon fluorescence microscope using selective plane illumination. *Optics express*, 18(8):8491–8498, 2010. 54

[94] Thomas A Planchon, Liang Gao, Daniel E Milkie, Michael W Davidson, James A Galbraith, Catherine G Galbraith, and Eric Betzig. Rapid three-dimensional isotropic imaging of living cells using bessel beam plane illumination. *Nature methods*, 8(5):417–423, 2011. 54, 57, 60

[95] Florian O Fahrbach, Philipp Simon, and Alexander Rohrbach. Microscopy with self-reconstructing beams. *Nature Photonics*, 4(11): 780–785, 2010. 54, 60

[96] GA Siviloglou, J Broky, Aristide Dogariu, and DN Christodoulides. Observation of accelerating airy beams. *Physical Review Letters*, 99 (21):213901, 2007. 55

[97] J Durnin. Exact solutions for nondiffracting beams. i. the scalar theory. *JOSA A*, 4(4):651–654, 1987. 55, 56

[98] John Broky, Georgios A Siviloglou, Aristide Dogariu, and Demetrios N Christodoulides. Self-healing properties of optical airy beams. *Optics express*, 16(17):12880–12891, 2008. 55

[99] D McGloin and K Dholakia. Bessel beams: diffraction in a new light. *Contemporary Physics*, 46(1):15–28, 2005. 57, 58, 59

[100] J1 Durnin, JJ Miceli Jr, and JH Eberly. Diffraction-free beams. *Physical Review Letters*, 58(15):1499, 1987. 57

[101] Jeffrey A Davis, E Carcole, and Don M Cottrell. Nondiffracting interference patterns generated with programmable spatial light modulators. *Applied optics*, 35(4):599–602, 1996. 58

[102] John H McLeod. The axicon: a new type of optical element. *JOSA*, 44(8):592–597, 1954. 58

[103] Shiro Fujiwara. Optical properties of conic surfaces. i. reflecting cone. *JOSA*, 52(3):287–291, 1962. 58

[104] Rieko Arimoto, Caesar Saloma, Takuo Tanaka, and Satoshi Kawata. Imaging properties of axicon in a scanning optical system. *Applied optics*, 31(31):6653–6657, 1992. 58, 59

[105] Florian O Fahrbach and Alexander Rohrbach. A line scanned light-sheet microscope with phase shaped self-reconstructing beams. *Optics express*, 18(23):24229–24244, 2010. 60

[106] Omar E Olarte, Jacob Licea-Rodriguez, Jonathan A Palero, Emilio J Gualda, David Artigas, Jürgen Mayer, Jim Swoger, James Sharpe, Israel Rocha-Mendoza, Raul Rangel-Rojo, et al. Image formation by linear and nonlinear digital scanned light-sheet fluorescence microscopy with gaussian and bessel beam profiles. *Biomedical optics express*, 3(7):1492–1505, 2012. 60, 115

[107] Peter M Chen, Edward K Lee, Garth A Gibson, Randy H Katz, and David A Patterson. Raid: High-performance, reliable secondary storage. *ACM Computing Surveys (CSUR)*, 26(2):145–185, 1994. 75

[108] Murmex by distrio. software framework for distributed input/output applications, 2016. 76

[109] Johannes Schindelin, Ignacio Arganda-Carreras, Erwin Frise, Verena Kaynig, Mark Longair, Tobias Pietzsch, Stephan Preibisch, Curtis Rueden, Stephan Saalfeld, Benjamin Schmid, et al. Fiji: an open-source platform for biological-image analysis. *Nature methods*, 9(7):676–682, 2012. 81

[110] Misha B Ahrens, Michael B Orger, Drew N Robson, Jennifer M Li, and Philipp J Keller. Whole-brain functional imaging at cellular resolution using light-sheet microscopy. *Nature methods*, 10(5):413–420, 2013. 82, 93, 116

[111] Florian O Fahrbach and Alexander Rohrbach. Propagation stability of self-reconstructing bessel beams enables contrast-enhanced imaging in thick media. *Nature communications*, 3:632, 2012. 83

[112] Georg Nagel, Doris Ollig, Markus Fuhrmann, Suneel Kateriya, Anna Maria Musti, Ernst Bamberg, and Peter Hegemann. Channelrhodopsin-1: a light-gated proton channel in green algae. *Science*, 296(5577):2395–2398, 2002. 97

[113] Rohit Prakash, Ofer Yizhar, Benjamin Grewe, Charu Ramakrishnan, Nancy Wang, Inbal Goshen, Adam M Packer, Darcy S Peterka, Rafael Yuste, Mark J Schnitzer, et al. Two-photon optogenetic toolbox for fast inhibition, excitation and bistable modulation. *Nature methods*, 9(12):1171–1179, 2012. 97

[114] Ofer Yizhar, Lief E Fenno, Thomas J Davidson, Murtaza Mogri, and Karl Deisseroth. Optogenetics in neural systems. *Neuron*, 71(1):9–34, 2011. 99

[115] John Y Lin. A user's guide to channelrhodopsin variants: features, limitations and future developments. *Experimental physiology*, 96(1): 19–25, 2011. 98

[116] Koichi Kawakami. Tol2: a versatile gene transfer vector in vertebrates. *Genome biology*, 8(1):1, 2007. 101, 107, 108

[117] Cheol-Hee Kim, Emiko Ueshima, Osamu Muraoka, Hidekazu Tanaka, Sang-Yeob Yeo, Tae-Lin Huh, and Naomasa Miki. Zebrafish elav/huc homologue as a very early neuronal marker. *Neuroscience letters*, 216 (2):109–112, 1996. 101

[118] Jeremy Freeman, Nikita Vladimirov, Takashi Kawashima, Yu Mu, Nicholas J Sofroniew, Davis V Bennett, Joshua Rosen, Chao-Tsung Yang, Loren L Looger, and Misha B Ahrens. Mapping brain activity at scale with cluster computing. *Nature methods*, 11(9):941–950, 2014. 101

[119] Ofer Yizhar, Lief E Fenno, Matthias Prigge, Franziska Schneider, Thomas J Davidson, Daniel J O'Shea, Vikaas S Sohal, Inbal Goshen, Joel Finkelstein, Jeanne T Paz, et al. Neocortical excitation/inhibition balance in information processing and social dysfunction. *Nature*, 477(7363):171–178, 2011. 101

[120] GARY W Stuart, JAMES V McMURRAY, and MONTE Westerfield. Replication, integration and stable germ-line transmission of foreign sequences injected into early zebrafish embryos. *Development*, 103(2):403–412, 1988. 107

[121] Karl J Clark, Mark D Urban, Kimberly J Skuster, and Stephen C Ekker. Transgenic zebrafish using transposable elements. *Methods in cell biology*, 104:137, 2011. 108

[122] Florian O Fahrbach, Vasily Gurchenkov, Kevin Alessandri, Pierre Nassoy, and Alexander Rohrbach. Light-sheet microscopy in thick media using scanned bessel beams and two-photon fluorescence excitation. *Optics express*, 21(11):13824–13839, 2013. 115

[123] Alexander Rohrbach. Artifacts resulting from imaging in scattering media: a theoretical prediction. *Optics letters*, 34(19):3041–3043, 2009. 116

[124] Alex Gomez-Marin, Brian Duistermars, Mark A Frye, and Matthieu Louis. Mechanisms of odor-tracking: multiple sensors for enhanced perception and behavior. *Frontiers in cellular neuroscience*, 4:6, 2010. 117

[125] Alexander Borst, Juergen Haag, and Dierk F Reiff. Fly motion vision. *Annual review of neuroscience*, 33:49–70, 2010. 117

[126] CE Carr and M Konishi. A circuit for detection of interaural time differences in the brain stem of the barn owl. *The Journal of Neuroscience*, 10(10):3227–3246, 1990. 117

[127] Misha Benjamin Ahrens, Kuo-Hua Huang, Sujatha Narayan, Brett D Mensh, and Florian Engert. Two-photon calcium imaging during fictive navigation in virtual environments. *Frontiers in neural circuits*, 7:104, 2013. 117

[128] Timothy W Dunn, Yu Mu, Sujatha Narayan, Owen Randlett, Eva A Naumann, Chao-Tsung Yang, Alexander F Schier, Jeremy Freeman, Florian Engert, and Misha B Ahrens. Brain-wide mapping of neural activity controlling zebrafish exploratory locomotion. *eLife*, 5:e12741, 2016. 117

[129] Herwig Baier and Ethan K Scott. Genetic and optical targeting of neural circuits and behavior-zebrafish in the spotlight. *Current opinion in neurobiology*, 19(5):553–560, 2009. 117

[130] Frederick B Shipley, Christopher M Clark, Mark J Alkema, and Andrew M Leifer. Simultaneous optogenetic manipulation and calcium imaging in freely moving c. elegans. *arXiv preprint arXiv:1311.6406*, 2013. 117

[131] John Peter Rickgauer, Karl Deisseroth, and David W Tank. Simultaneous cellular-resolution optical perturbation and imaging of place cell firing fields. *Nature neuroscience*, 17(12):1816–1824, 2014. 119, 120

[132] Eirini Papagiakoumou. Optical developments for optogenetics. *Biology of the Cell*, 105(10):443–464, 2013. 120

[133] Alipasha Vaziri and Valentina Emiliani. Reshaping the optical dimension in optogenetics. *Current opinion in neurobiology*, 22(1):128–137, 2012. 120

[134] Dan Oron, Eirini Papagiakoumou, F Anselmi, and Valentina Emiliani. Two-photon optogenetics. *Prog. Brain Res*, 196:119–143, 2012. 130

[135] Phase spatial light modulator lcos-slm, 2015. 130

Corrections

Page 6

$$\phi = \frac{k_F}{k_F + k_{nF}} \tag{1.1}$$

$$\tau = \frac{1}{k_F + k_{nF}} \tag{1.2}$$

In next line: $F_k \rightarrow k_F$

$$k_F = 2.88 \times 10^9 n^2 \frac{\int F \;\bar{\nu}\; d\bar{\nu}}{\int \;\bar{\nu}^{\;3}\; F \;\bar{\nu}\; d\bar{\nu}} \int \frac{\varepsilon \;\bar{\nu}}{\bar{\nu}} d\bar{\nu} \tag{1.3}$$

$$\tau_n = \frac{1}{k_F} \tag{1.5}$$

Page 7

$$g(x,y) = \int\int_{-\infty}^{\infty} f\left(x^{'},y^{'}\right) h\left(x - x^{'}, y - y^{'}\right) dx^{'} dy^{'} \tag{2.4}$$

Page 53

After eq. 5.4: $fill \rightarrow f_{ill}$

“larger than 2 time of its minimum width ...” → “larger than $\sqrt{2}$ time of its minimum width ...”

Page 56

First line: $U\left(\vec{r},t\right) = U\left(\vec{r}\right) e^{i((2\pi k_z z)-\omega t)} \rightarrow U\left(\vec{r},t\right) = U\left(\vec{r}\right) e^{-i\omega t}$